Nano Research

ISSN 1998-0124 CN 11-5974/O4
https://doi.org/10.26599/NR.2026.94908456

Review Article

Recent progress on artificial spiking neurons based emerging electronic devices for neuromorphic perception and computation

Zheng Fang[2,†,§], Kaiyao Wang[1,§], Shujing Zhao[1,3], Shiquan Fan[1,3], Weihua Liu[1,3], Xin Li[1,3], Li Geng[1,3], Chuanyu Han[1,3](✉)

[1] School of Microelectronics, Xi'an Jiaotong University, Xi'an 710049, China

[2] School of Physics, Xi'an Jiaotong University, Xi'an 710049, China

[3] The Key Lab of Micro-nano Electronics and System Integration of Xi'an City, Xi'an 710049, China

[†] Present address: School of Electronics, Peking University, Beijing 100871, China

[§] Zheng Fang and Kaiyao Wang contributed equally to this work.

Nano Res., **Just Accepted Manuscript** • https://doi.org/10.26599/NR.2026.94908456

https://www.sciopen.com/journal/1998-0124 on Jan. 16, 2026

Just Accepted

TABLE OF CONTENTS (TOC)

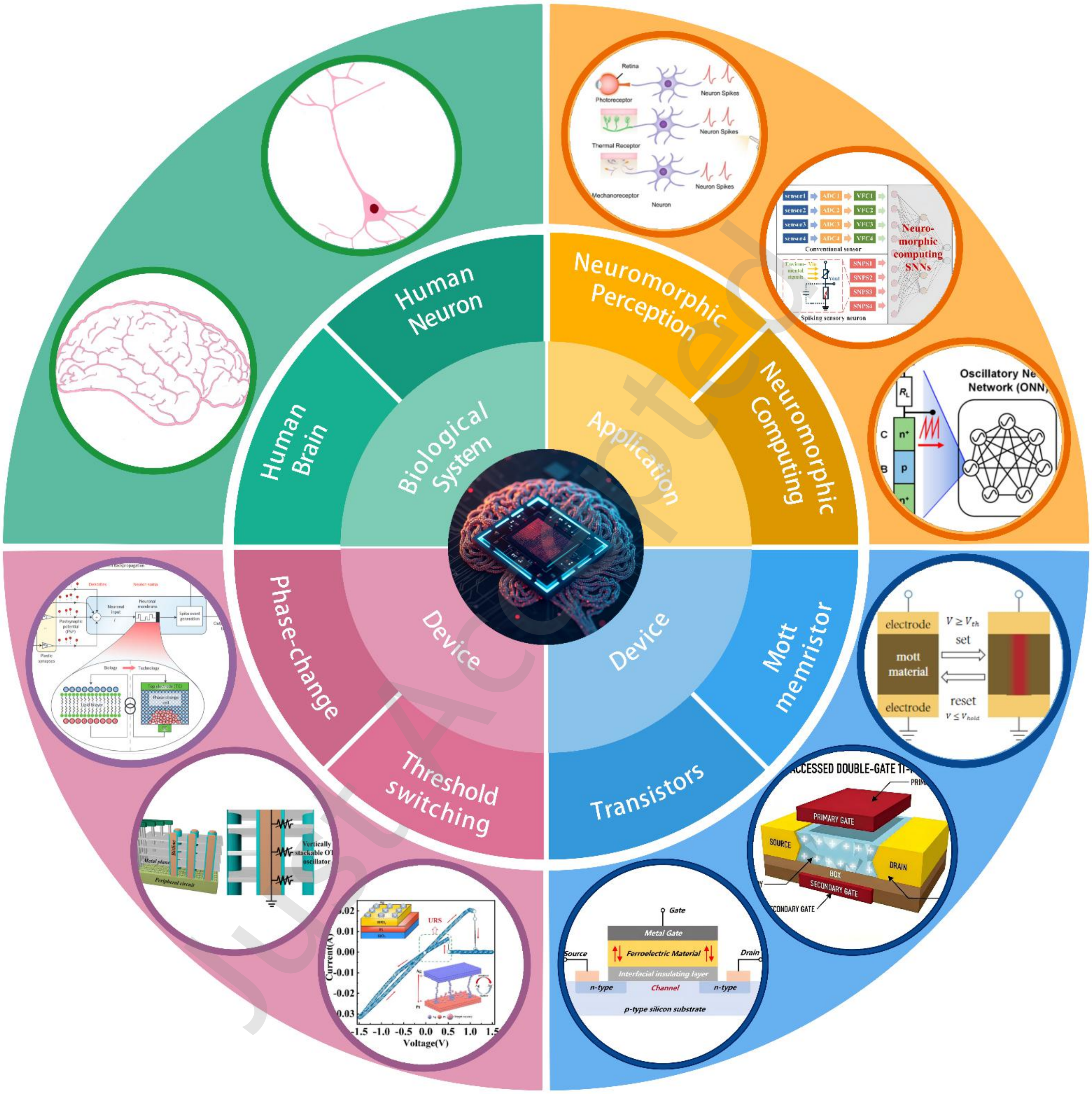

This review systematically investigates artificial spiking neurons through a "material-device-circuit-system" hierarchy, exploring their implementations in neuromorphic perception and computing, and providing insights for future development.

Recent progress on artificial spiking neurons based emerging electronic devices for neuromorphic perception and computation

Zheng Fang[2, †, §], Kaiyao Wang[1, §], Shujing Zhao[1,3], Shiquan Fan[1,3], Weihua Liu[1,3], Xin Li[1,3], Li Geng[1,3], and Chuanyu Han[1,3, ✉]

[1] School of Microelectronics, Xi'an Jiaotong University, Xi'an 710049, China
[2] School of Physics, Xi'an Jiaotong University, Xi'an 710049, China
[3] The Key Lab of Micro-nano Electronics and System Integration of Xi'an City, Xi'an 710049, China
[†] Present address: School of Electronics, Peking University, Beijing 100871, China
[§] Zheng Fang and Kaiyao Wang contributed equally to this work.

✉ Address correspondence to hanchuanyu@mail.xjtu.edu.cn

Cite this article: *Nano Research*, **2026**, *19*, 94908456. https://doi.org/10.26599/NR.2026.94908456

ABSTRACT: The recent surge in enthusiasm for cutting-edge artificial intelligence and neuromorphic computing paradigms, such as spiking neural networks (SNNs) and oscillatory neural networks (ONNs), has sparked significant interest. This has motivated researchers worldwide to delve into the study and realization of artificial spiking neurons. Conventional electronic devices, such as MOSFETs and diodes, lack the subtle nonlinear behaviors inherent in neuromorphic systems, thus requiring complex circuits and many devices to replicate the simplest functions of biological neurons at the expense of substantial energy and hardware costs. Consequently, to emulate biological neurons, researchers are turning to novel artificial neuron devices, aiming to simplify structure, reduce power consumption, and lower hardware cost. This study provides a comprehensive review and benchmark of recent progress in artificial spiking neurons based on emerging electronic devices for neuromorphic perception and computation. It summarizes various artificial neurons using different spiking mechanisms, including Mott, Ion diffusion, phase-change, ovonic threshold switching (OTS) memristor neurons and transistor neurons. Furthermore, the work reviews practical applications in neuromorphic perception and computing. Finally, it discusses future directions and trends. By offering valuable insights, this work aims to serve as a reference guide, inspiring further research and practical use of artificial spiking neurons.

KEYWORDS: artificial spiking neuron, threshold-switching device, Mott memristor, transistor, neuromorphic perception and computation

1. Introduction

The rapid advancements in technologies like the Internet of Things (IoT), 5G, and cloud computing, coupled with the rise of artificial intelligence (AI), have significantly enhanced the capabilities of modern computers, particularly in task of decision-making, speech recognition, image classification, intelligent driving and natural language processing [1-4]. The growing integration of AI with IoT has enabled smart devices not only to exchange information but also to process data and make decisions at the edge [5]. However, the massive amount of data generated by these interconnected devices presents significant challenges in data acquisition, storage, processing, and communication for traditional computing systems [6, 7].

In conventional system, sensors capture analog signals from the environment, which are then converted into digital signals by analogue-to-digital converters (ADCs) and subsequently fed into the computing system for storage and processing. This process often results in a high volume of redundant raw data, increasing the processing system's workload and reducing efficiency due to frequent data exchanges. Furthermore, traditional computing architectures, including smartphones, rely on the Von Neumann architecture, where the processing unit and memory are physically separated. This separation leads to significant energy consumption and latency, known as the "memory wall," caused by the constant movement of large amounts of data between the processing unit and memory [8-10]. For example, a single integer multiply-accumulate (MAC) operation may only require a few picojoules (pJ) of energy, but fetching the convolution kernel values from off-chip DRAM can consume several hundred pJ [11]. The energy and time required for updating the millions of weight values during deep learning algorithm training severely hamper the efficiency of information processing.

In contrast, the human brain, with over 10^{15} synapses and 10^{11} neurons, operates at a level nearly five orders of magnitude more efficient than existing computing systems, functioning effectively with just 20 watts of power [12-14] [10, 15]. This efficiency largely comes from the brain's integrated processing architecture of sensing, storing and computing, and the co-localization of memory and computing functionalities [9, 16, 17]. Consequently, constructing neuromorphic machines that mimic the working patterns of the human nervous system has become a significant research focus [18-23].

The human nervous system relies on various receptors, synapses and neurons [15, 24]. To emulate this system, neuromorphic electronic devices that replicate the functions of biological receptors, synapses, and neurons are essential for developing computing in memory (CIM) and computing in sensor (CIS) paradigms [25, 26]. However, traditional electronic components, such as conventional MOSFETs, lack the nonlinear behavior necessary for neuromorphic devices, requiring complex circuitry and numerous components to perform even simple biological functions[27, 28]. In contrast, memristors and novel transistors, in particular, are favored for simulating biological neurons and synapses due to their faster switching speeds and lack of need for additional mechanisms to update information, making them ideal for applications in perceptrons, memory arrays, and neuromorphic computing [2, 5, 28-30]. Additionally, neuromorphic perception systems, which address the limitations of ADCs and integrate external stimulus preprocessing and spike-coded generation, are gaining increasing attention from researchers [31-33].

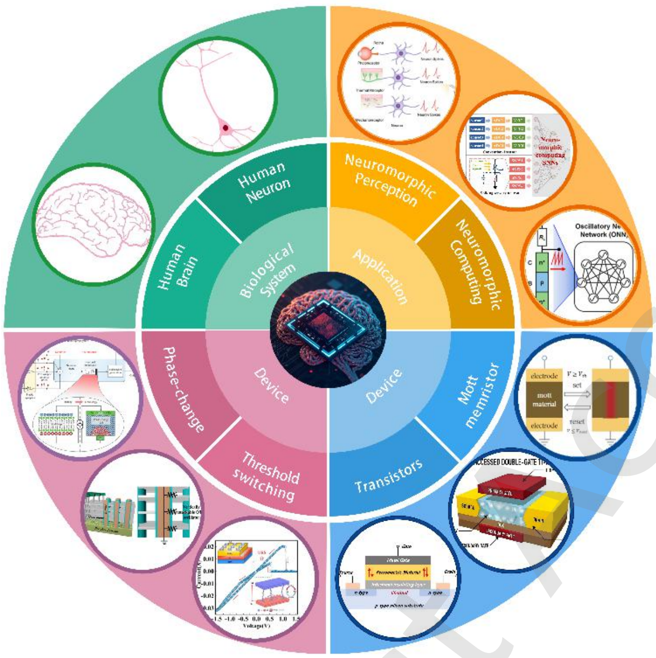

Figure 1 Schematic diagram of the human brain system with artificial spiking neurons and systems.

Therefore, unlike previous reviews that concentrate on a single class of artificial neuron devices and a relatively limited set of targeted application scenarios, this review adopts the material-device-circuit-system perspective to provide a comprehensive overview of artificial spiking neurons, as shown in **Fig. 1**. We summarize their design principles, operating mechanisms and performance characteristics, and benchmark them within a unified comparative framework. Building on this foundation, we critically survey recent advances in spiking neuron devices and circuits, and discuss their integration into multimodal neuromorphic perception systems, including vision, touch, audition and olfaction, as well as brain-inspired computing architectures such as spiking neural networks (SNNs) and oscillatory neural networks (ONNs). By articulating the key opportunities and bottlenecks across materials, devices and systems, this review provides a coherent technology roadmap for energy-efficient, low-power and highly integrated neuromorphic platforms. Ultimately, we aim to offer systematic insights that will inform and inspire future research and application of artificial spiking neurons.

2. Artificial spiking neuron

Most neurons consist of a cell body (soma), an axon, and dendrites. Information is transmitted to the soma via biological spiking signals through the dendrites and then sent out through the axon as exhibited in **Fig.2(a)** [34]. The soma receives and integrates this information through changes in the voltage potential across the neuron's cell membrane. When the voltage potential reaches a specific threshold, the soma generates an action potential that propagates along the axon. This process allows for the transmission and processing of information between neurons [35-37].

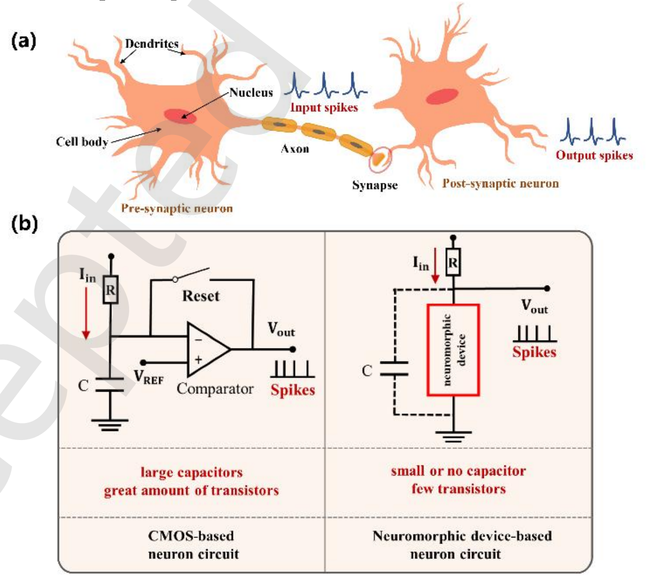

Figure 2 Schematic diagram of biological neurons and artificial neurons, (a) Signal transmission from the pre-synaptic neuron to the post-synaptic neuron, (b) Comparison between CMOS-based neuron circuit and neuromorphic device-based spiking neuron circuit.

However, conventional electronic devices like MOSFETs require complex circuitry and numerous components to mimic even simple biological neuron functions, such as integrate-and-fire (IF) and leaky integrate-and-fire (LIF) mechanisms [38, 39]. The CMOS-based spiking neuron not only employs capacitors and voltage comparators to complete the integration of charges, but also requires a complex peripheral reset circuit to realize the charge leakage process. Consequently, achieving low power consumption, large-scale integration, and high efficiency in spiking neural networks (SNNs) built on CMOS circuits is challenging. Recently, advancements in novel neuromorphic devices have made it possible to create artificial spiking neurons using just a single device or with minimal peripheral circuitry. The comparison chart of these two types of neurons is vividly demonstrated in **Fig. 2(b)**. These emerging neuromorphic devices can generally be divided into two categories: memristor-based devices (including Mott memristors (IMT), ion-diffusion memristors, Ovonic threshold switching (OTS) memristors, and phase change memristors (PCM)) and new types of transistors (including single transistors, ferroelectric field-effect transistors (FeFETs), antiferroelectric field-effect transistors (Anti-

FeFETs), and mulitple-gate FETs), as shown in **Fig. 3**. Besides, two-dimensional (2D) materials represent a versatile active platform for artificial neuron devices, as they allow nonlinear responses, tunable temporal dynamics, and controllable state evolution to be integrated within compact structures [40-42]. 2D materials serve not only as conduction channels but also as multifunctional media for signal transduction and state modulation across electrical, optical, ionic, and polarization degrees of freedom [43, 44]. Therefore, 2D materials constitute highly effective enabling materials for both memristor-based and transistor-based artificial spiking neurons. Beyond 2D materials, organic semiconductors and conducting polymers have also increasingly emerged in recent years as important material platforms. Leveraging their mechanical flexibility, biocompatibility, and pronounced ion–electron coupling, these materials have enabled systematic advances in both synapse-like and neuron-like devices [45-47].

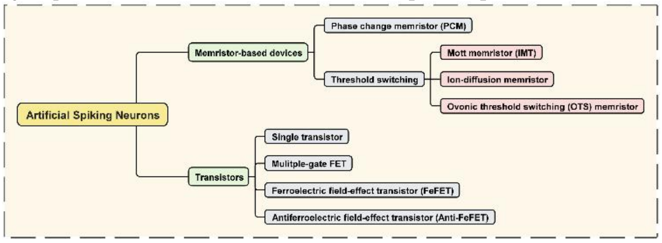

Figure 3 Artificial spiking neuron classification map.

2.1 Key Performance Indicators for Benchmarking Artificial Spiking Neurons

To systematically evaluate and compare the diverse range of emerging artificial neuron devices, we introduce nine critical performance metrics. These indicators not only quantify the device characteristics but also determine their suitability for specific neuromorphic sensing and computing applications.

(1) Electrical Characteristics

Threshold Voltage (V_{th}): This metric defines the minimum voltage required to trigger a resistive switching event or a neuronal spike. A lower V_{th} is desirable for reducing the operating voltage and power consumption of the system. However, it must be balanced against signal stability to prevent false firing induced by noise.

Energy per Spike: This indicator represents the energy consumption associated with a single firing event, typically measured in picojoules (pJ) or femtojoules (fJ). Since high energy efficiency is a primary advantage of neuromorphic computing over conventional Von Neumann architectures, minimizing energy per spike is crucial for edge computing and battery-powered sensory systems.

Frequency: This refers to the maximum firing rate of the neuron. While biological neurons typically operate at low frequencies (<100 Hz), artificial neurons can achieve frequencies ranging from kHz to GHz. High-frequency operation is essential for rapid data processing in computing tasks, whereas lower frequencies may be preferred for bio-hybrid interfaces to match biological timescales.

(2) Reliability and Integration

Endurance: Defined as the maximum number of switching cycles a device can sustain before failure. Given the event-driven nature of Spiking Neural Networks (SNNs), where neurons fire frequently, high endurance is a prerequisite for reliable long-term operation.

Thermal Budget: This parameter specifies the maximum temperature required during the device fabrication process. Devices with a low thermal budget (<400℃) are compatible with CMOS Back-End-Of-Line (BEOL) processes, enabling high-density 3D stacking directly on top of standard CMOS logic circuits. Conversely, devices requiring high-temperature annealing are typically restricted to Front-End-Of-Line (FEOL) integration.

CMOS-back-end Compatibility: This metric assesses whether the device materials and fabrication steps are compatible with standard silicon CMOS foundries. High compatibility facilitates large-scale integration and reduces manufacturing costs, which is vital for commercial adoption. We specifically use the term "back-end compatibility" rather than general "CMOS compatibility" to highlight the potential for 3D Integration. FEOL-compatible devices (e.g., FeFETs) typically require high-temperature processing (>900°C) and must occupy silicon substrate area, thereby limiting circuit integration density. In contrast, BEOL-compatible devices (e.g., Mott and OTS memristors) usually possess a low thermal budget (<400°C), allowing them to be integrated directly over the metal interconnect layers of CMOS logic circuits. This characteristic is essential for realizing high-density "In-Memory Computing" architectures.

Test Conditions: Reported performance metrics, particularly energy and frequency, are heavily dependent on external test conditions such as series resistance (R_s) and parallel capacitance (C_p). Specifying these conditions is essential for fair benchmarking across different studies.

(3) Functional Characteristics

Volatility: This describes whether the device retains its state after the removal of an external stimulus. Volatile devices spontaneously recover their state, allowing for compact implementation of neuronal behavior without the need for reset circuits, offering advantages in mimicking biological neuron dynamics. Non-volatile devices require additional reset operations but offer advantages in synaptic weight tunability; therefore, they are predominantly used as artificial synaptic devices.

Neuron Type: This categorizes the specific biological neuron model simulated by the device. Models range from simple types, such as Integrate-and-Fire (IF), Leaky Integrate-and-Fire (LIF), and oscillatory neurons, to complex types like the FitzHugh-Nagumo (FHN) and Hodgkin-Huxley (HH) models. The choice of neuron type dictates the coding scheme (e.g., rate coding vs. temporal coding) and the complexity of the required peripheral circuitry. Simple neuron structures are advantageous for constructing large-scale circuits, with the LIF neuron currently being the primary model for artificial neuron research.

2.2 Memristor-based artificial spiking neurons

Memristors offer several advantages, including low power consumption, compatibility with complementary metal-oxide-semiconductor (CMOS) technology, strong potential for 3D integration, and a simple structure [48-50]. Memristors can be classified as either volatile or nonvolatile based on the retention time of their stored state.

Volatile memristors, also known as threshold switching (TS) devices, automatically revert to a high resistance state (HRS), which simplifies the design and fabrication of neuron circuits. TS devices can be categorized into three main types based on different mechanisms: insulator-metal transition (IMT) memristors, ion diffusion memristors, and amorphous chalcogenide-based ovonic threshold switching (OTS) memristors [5, 17, 29, 51, 52].

TS memristors undergo a transition from high resistance state (HRS) to low resistance state (LRS) at the threshold voltage V_{th} during the forward scanning of DC voltage. Then, during the reverse voltage sweep, they jump back from LRS to HRS at the holding voltage V_{hold}. This "LRS → HRS → LRS" switching process of TS devices perfectly corresponds to the biological membrane potential's process of first rising sharply and then dropping suddenly. The TS memristors do not require an additional reset circuit when switching back from HRS to LRS, but only need the applied voltage to be lower than V_{hold}. This means that neuron circuits based on TS devices can be very simple by using charging and discharging circuits.

The specific circuit layout and basic principle are well illustrated in **Fig. 4**. When the TS device is in HRS (R_{OFF}), the time constant of the charging loop is much smaller than that of the discharging loop. Therefore, the voltage change on the capacitor is predominantly caused by charging. When the voltage across the TS device reaches V_{th}, the device switches to LRS (R_{ON}). At this point, the time constant of the discharging circuit is much smaller than that of the charging circuit. Therefore, the voltage across the capacitor drops rapidly. The alternating charging and discharging process generates a spike sequence.

Nonvolatile memristors, including phase-change memristors (PCMs), resistive random-access memory (RRAM), magnetoresistive random-access memory (MRAM), and ferroelectric random-access memory (FRAM), maintain their states even when the voltage bias are removed, thus making them ideal for emulating the synaptic plasticity of biological synapses [51]. Additionally, exploring the intrinsic cycle-to-cycle variations in the resistive switching process, phase-change memristors (PCMs) can also be used to construct artificial neurons, often requiring an additional reset circuit.

The typical characteristics, switching mechanism, advantages and disadvantages of four types of memristors (i.e. IMTs, ion diffusion memristors, OTS memristors, PCMs) that can be used to construct artificial neurons are listed in **Fig. 5**.

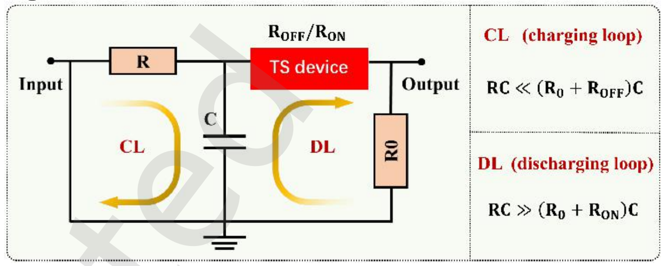

Figure 4 Basic design template and construction method of a spiking neuron circuit based on a TS memristor.

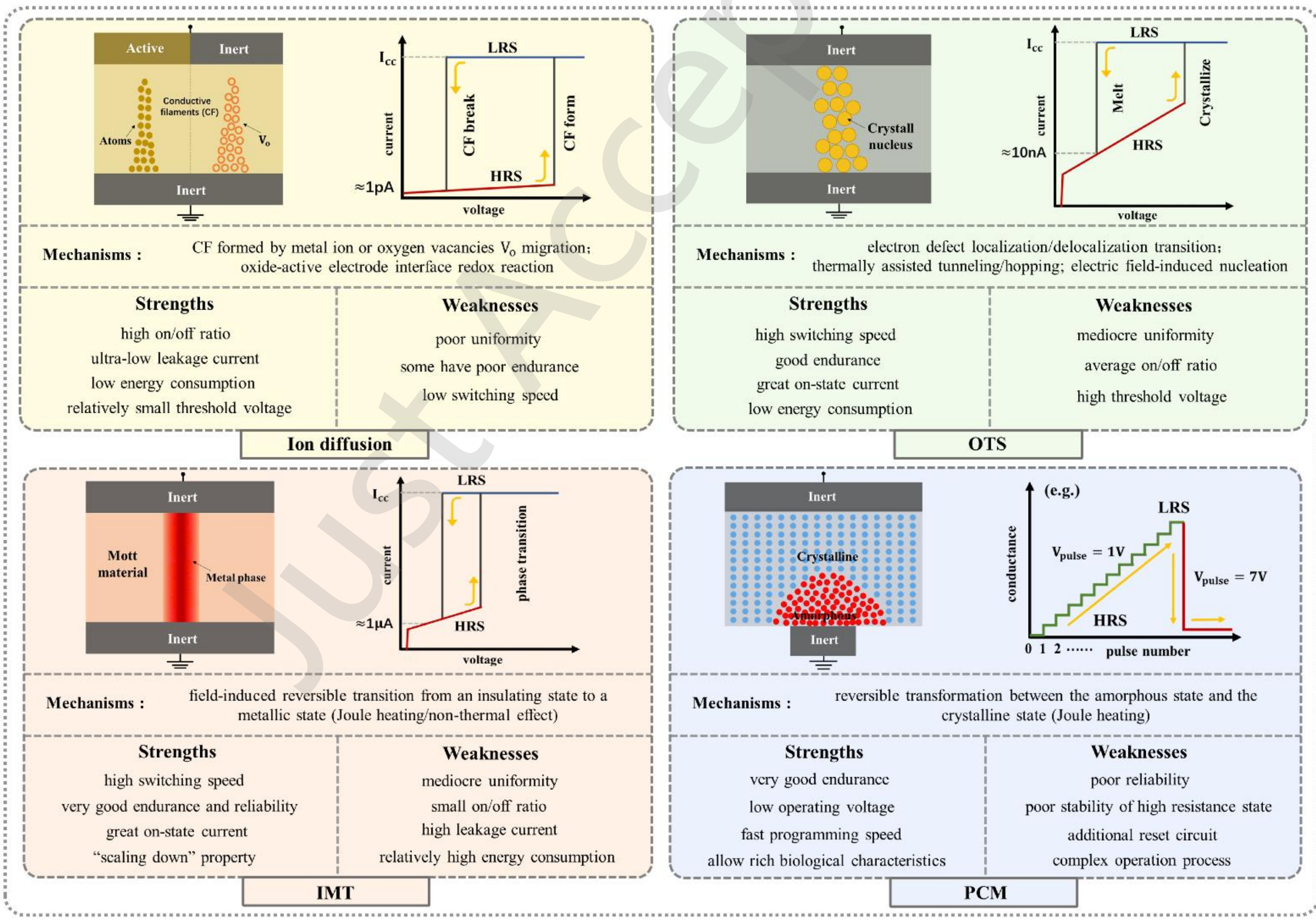

Figure 5 Comprehensive comparisons of four main kinds of memristor for establishing artificial neurons.

2.2.1 Mott Memristor neuron

(1) Operating mechanism

Mott insulators are characterized by their unique insulator-metal transition (IMT) phenomenon [53-57]. The most common structure for a Mott memristor is a metal-Mott insulator-metal "sandwich" configuration, where the Mott insulator is typically NbO_2 or VO_2 [58-66]. The operating mode of a Mott memristor is illustrated in **Fig. 6(a)**. When electrical excitation is applied to the device, the conductivity of the Mott material decreases as Joule heating increases, initiating the setting process. Once the temperature of the Mott material exceeds its phase transition temperature, it transitions from an insulating state to a metallic state, and the Mott memristor switches from a high resistance state (HRS) to a low resistance state (LRS) [67-69].

When the electrical excitation is removed, the conductivity of the Mott material increases as Joule heating diminishes, leading to the resetting process. As the temperature drops below the phase transition threshold, the Mott material reverts from the metallic state back to its initial insulating state, causing the Mott memristor to switch from LRS to HRS. **Fig. 6(b)** shows the I-V characteristic curve of the Mott memristor during the setting and resetting processes. When a voltage scan is applied, the device switches from HRS to LRS once the voltage across the memristor reaches its threshold voltage (V_{th}) and reverts from LRS to HRS when the voltage falls below the holding voltage (V_{hold}).

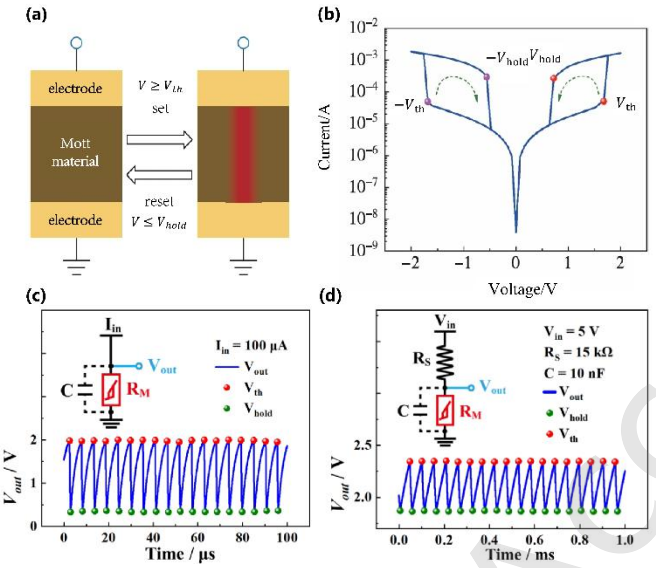

Figure 6 (a) Schematic diagram of Mott Memristor setting and resetting process. (b) I-V curve of Mott Memristor under voltage scanning. Reproduced with permission from Ref. [70] © Microelectronics 2024 (c) Schematic diagram of Mott memristor neurons based on current-driven; (d) Schematic diagram of Mott memristor neurons based on current-driven.

Based on the TS property of Mott memristors, artificial spiking neurons capable of generating spikes can be constructed. Typically, there are two types of circuit structures for the Mott memristor neurons: one is current-driven and the other is voltage-driven, as shown in **Fig. 6**.

1) Current driven circuit

The inset in **Fig. 6(c)** illustrates the circuit structure of a current-driven Mott memristor neuron. In this setup, RM represents the Mott memristor, while C represents either the capacitor in parallel with the Mott memristor or the parasitic capacitance inherent to the Mott memristor itself. I_{in} denotes the input current, and V_{out} is the output voltage. Notably, a pulse neuron can be constructed using just a single Mott memristor, without the need for an external capacitor. Compared to oscillators implemented with CMOS technology, the electronic spiking neuron circuit based on Mott memristors is remarkably simple. To better understand the relationship between the frequency of output spikes and the input current or parallel capacitance, the following mathematical expressions are derived from Kirchhoff's current law,

$$I_{in} = \frac{V_{out}}{R_M} + C\frac{dV_{out}}{dt} \quad (1)$$

To solve for V_{out}, equation (1) is rearranged as follows:

$$\tau_m \frac{dV_{out}}{dt} = -V_{out} + I_{in}R_M \quad (2)$$

Where $\tau_m = I_{in} \times R_M$， when R_M is in the HRS, $R_M = R_H$; when RM in the LRS, $R_M = R_L$.

Assume $R_H >> R_s >> R_L$， solve Equation (2), we can obtain the rise time t_r and fall time t_f, which are expressed by

$$t_r = R_H C \ln\left(\frac{I_{in}R_H - V_{hold}}{I_{in}R_H - V_{th}}\right) \quad (3)$$

$$t_f = R_L C \ln\left(\frac{V_{th} - I_{in}R_L}{V_{hold} - I_{in}R_L}\right) \quad (4)$$

,respectively.

Therefore， the spiking frequency (f) output by the current-driven neuron can be represented as follows:

$$f = \frac{1}{t_r + t_f} \quad (5)$$

Due to $R_H >> R_L$, the pulse frequency of the current-driven artificial neuron is mainly determined by the rise time. Therefore, the pulse frequency output by the device can be represented as follows,

$$f \approx \frac{1}{t_r} \approx \frac{I_{in} - \frac{V_{th}}{R_H}}{C\left(V_{th} - V_{hold}\right)} \quad (6)$$

From equations (3)-(5), with the value of the parallel capacitance remaining constant, the pulse frequency output by the current-driven Mott memristive neuron increases as the input current increases. With the input current value remaining constant, the pulse frequency output by the current-driven Mott memristive neuron decreases as the value of the parallel capacitance increases. This conclusion is consistent with the experimental results.

From equations (3)-(5), with the value of the parallel capacitance remaining constant, the pulse frequency output by the current-driven Mott memristive neuron increases as the input current increases. With the input current value remaining constant, the pulse frequency output by the current-driven Mott memristive neuron decreases as the value of the parallel capacitance increases. This conclusion is consistent with the experimental results.

2) Voltage driven circuit

The inset in **Fig. 6(d)** illustrates the circuit structure of a voltage-driven Mott memristor-based oscillator. Here, R_M represents the Mott memristor, C represents the capacitor in parallel with the Mott memristor or the parasitic capacitance of the Mott memristor itself, and R_S represents the series resistor (which serves to divide voltage and limit current). V_{in} is the input voltage, and V_{out} is the output voltage. It can be seen that, without an external capacitor, an oscillator can be constructed using just one Mott memristor and a resistor. The frequency of the voltage pulses output by the voltage-driven Mott memristor artificial neuron is closely related to the V_{in}, C, and R_s. Based on the circuit structure of the artificial neuron, the following mathematical expressions are established according to Kirchhoff's current law,

$$\frac{V_{in} - V_{out}}{R_S} = \frac{V_{out}}{R_M} + C\frac{dV_{out}}{dt} \quad (7)$$

To solve for V_{out}, Equation (6) is rearranged as follows:

$$\frac{dV_{out}}{dt}=\frac{V_{in}}{CR_S}-\frac{R_S+R_M}{CR_SR_M}V_{out} \quad (8)$$

Assume R_H>>R_s>>R_L, solving Equation (7) yields the rise time (t_r) and fall time (t_f) of the voltage pulses output by the voltage-driven artificial neuron as follows:

$$t_r=-R_HC\ln\left(\frac{V_{th}-V_{in}\frac{R_H}{R_S}}{V_{hold}-V_{in}\frac{R_H}{R_S}}\right) \quad (9)$$

$$t_f=-R_LC\ln\left(\frac{V_{hold}-V_{in}\frac{R_L}{R_S}}{V_{th}-V_{in}\frac{R_L}{R_S}}\right) \quad (10)$$

Since R_H>>R_L, the rise time of the output pulse of the voltage-driven artificial neuron is much greater than the fall time. The pulse frequency output by the voltage-driven artificial neuron can be represented as follows:

$$f=\frac{1}{CR_H\ln\left(\frac{V_{hold}R_S-V_{in}R_H}{V_{th}R_S-V_{in}R_H}\right)} \quad (11)$$

From Equation (11), we can conclude that, the spiking frequency, f of the voltage-driven artificial neuron decreases as the R_s and C increases, and increased as the V_{in} increases.

(2) Oscillating neuron

Based on the TS property of the Mott Memristor, artificial spiking neurons with simple structure can be constructed [71]. For example, Yuan et al [33] built an artificial spiking neuron by connecting a VO_2 Mott Memristor in series with a resistor and in parallel with a capacitor as shown in **Fig. 7(a)**. When driven by voltage, the VO_2 Mott Memristor works in conjunction with the capacitor, enabling the generation of an oscillating voltage pulse signal at the output through the charging and discharging of the capacitor. As shown in **Fig. 7(b)**, the frequency of the output voltage pulse of the VO_2 Mott Memristor-based artificial spiking neuron decreases with the increase of the series resistance. This is consistent with the theoretical analysis. The combination of a resistor and capacitor with the VO_2 Memristor structure offers a concise method for constructing the artificial spiking neuron. However, the lower phase transition temperature of the VO_2 Mott Memristor (68°C) is significantly influenced by environmental conditions [72], rendering this structure unsuitable for high-temperature applications.

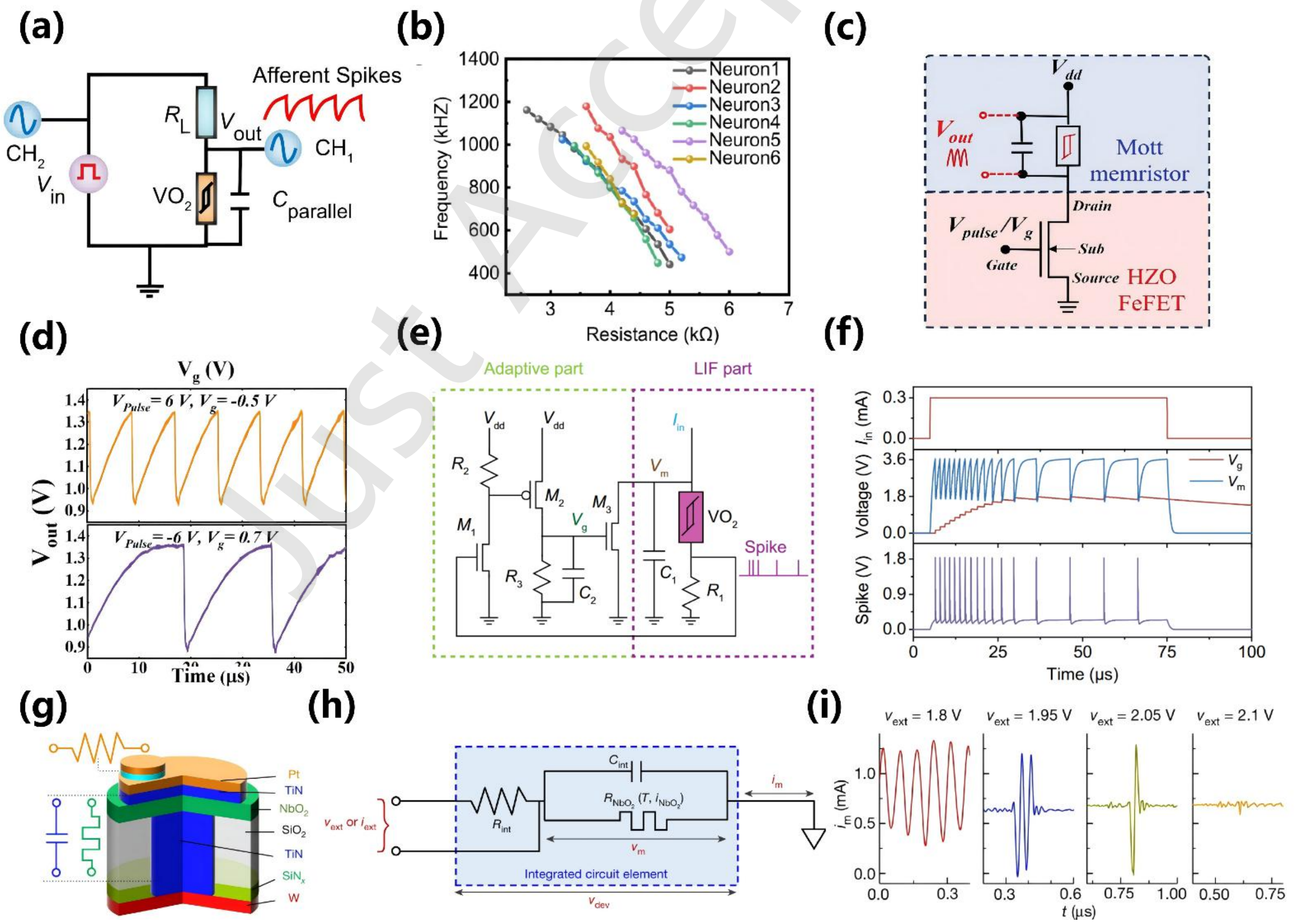

Figure 7 Mott Memristor-based artificial spiking neuron and its electrical characteristics. (a) Circuit structure of the VO2 Mott Memristor-based artificial spiking neuron. (b) Relationship between the output voltage spiking frequency of the VO_2 Mott Memristor-based artificial spiking neuron and the series resistor. Reproduced with permission from Ref. [33] © Springer Nature 2022. (c) Schematic diagram of the 1T1M programmable artificial spiking neuron. (d) Spiking rate with V_{pulse} fixed and V_g varied. Reproduced with permission from Ref. [73] © IEEE 2024. (e) Circuit diagram of the VO_2

memristor-based ALIF neuron. The adaptive part serves as a negative feedback control loop about M_3. Each firing of spikes from the LIF section results in the charging of C_2 and an increase in V_g, which activates M_3 to a greater extent. This contributes to an elevated leakage current and thus adaptation, which leads to decelerated charging of C_1 during the integration phase and a reduction in spiking frequency. The firing frequency of the ALIF neuron decreases as the V_g increases. (f) Variations of V_g, V_m, and V_{spike} over time. When the adapted frequency saturates, V_m shows a steady plateau during the charging period. Reproduced with permission from Ref. [74]. © Springer Nature 2023. (g) Circuit diagram of the device. (h) Structural diagram of the device. (i) Different neuromorphic electrical signals output from the device when applying different different neuromorphic electrical signals output from the device when different bias voltages (v_{ext}) are applied. Reproduced with permission from Ref. [75]. © Springer Nature 2020.

Consequently, NbO_x Memristors with higher phase transition temperature (about 800 ℃) have attracted more and more researchers' attention in recent years [76]. For instance, Zhao et al [73] built a programmable 1T1M artificial spiking neuron circuit by integrating a NbO_x Mott Memristor with an HZO ($Hf_{0.5}Zr_{0.5}O_2$) FeFET, shown in **Fig. 7(c)**. As shown in **Fig. 7(d)**, the neuron spiking rate increases with the increase of gate voltage (V_g) when the gate write pulse (V_{pulse}) is a constant value. The stable spiking rate of this neuron circuit at a fixed value of V_g indicates that the threshold voltage state of the FeFET is not disturbed during the oscillation process, which ensures the coding accuracy of the artificial spiking neuron. Meanwhile, the output spike rate and coding range of the applied V_g can be programmed by V_{pulse} when V_g is fixed, thus realizing the function of programmable spiking neuron.

(3) IF&LIF Neuron

The integrate-and-fire (IF) neuron model is one of the most prevalent computational neuroscience models. It integrates the input signals to a neuron to generate membrane potentials, and when these potentials exceed a threshold, spikes are generated [77]. Lee et al. [78] constructed an IF neuron simulation circuit by using an NbO_2-based threshold switching device. At the outset, the TS device is turned off, and the capacitance C_m of the analog membrane capacitor integrates the synaptic input current. Since the turn-off resistance R_{off} of the TS is much greater than the circuit output resistance R_{out}, the circuit is in the integration process and the output voltage V_{out} is close to 0. When V_{TS} approaches V_{TH}, the magnitude of R_{off} is equal to that of Rout, and V_{out} gradually increases to produce a spike output. Simultaneously, C_m is gradually discharged. When V_{TS} is less than V_{TH}, the device returns to the off state for the next integration process. Adding the leak process to the IF neuron forms the Leaky integrate-and-fire (LIF) neuron model [79]. In this model, when the membrane potential is lower than the threshold voltage, it gradually returns to the resting state. Valle et al. [80]constructed a heat-based LIF artificial neuron using a VO_2-based Mott memristor. The neuron uses heat flow instead of current and employs a resistor as a heater. The previous neuron electrical signal flowing through this resistor generates Joule heat. As a result, the VO_2-based Mott memristor thermally coupled to the resistor warms up, and ignition is generated when the temperature is higher than the threshold temperature. The role of R_{Load} is to reset the device and thereby output a spike current.

(4) ALIF Neuron

In biology, when a neuron is exposed to repetitive and prolonged stimulation like sustained sensory or artificial electrical current stimulation, it initially shows a strong onset response and then the time interval between spikes will subsequently increase [81]. This biological phenomenon is called spike frequency adaptation (SFA). To reinforce the history dependence of neurons, especially the SFA, several studies have introduced the Adaptive-Leaky Integrate and Fire (ALIF) neuron. These neurons are enhanced with an adaptive threshold that will increment after each firing spike and then depreciate exponentially with the time constant τ_{adp} [36, 74, 82]. Both LIF and ALIF neurons can be recognized as neural units with self-recurrency characteristics [83], yet hardware implementations of ALIF neurons are able to share complex behaviors of biological neurons and improve the computational capabilities of neuromorphic systems [36, 82].

Yuan et al. designed a highly efficient ALIF neuron based on a VO_2 memristor [74]. The advantageous features of VO_2 memristors such as the highly uniform symmetric threshold switching and fast volatile responds bring about great simplification to the neuron circuit. The VO_2 memristor is devised as planar device and its I–V characteristics demonstrates its stable volatile resistive switching property, when 100 cycles were executed. The built ALIF neuron modal is shown in **Fig. 7(e)**, which is combination of the compact adaptive control circuit and the fundamental LIF neuron. Biologically, the adaptive feature stems from the augmented membrane leakage current that occurs after the neuron discharges. When the neuron is at rest, the adaptive effect will weaken and the spiking frequency will return to its initial value. In the ALIF neuron, C_2 gains a discharging path through R_3 and further gradually shuts down M_3, which realizes adaptation effectively. **Fig. 7(f)** reveals that adaptive response of V_g, V_m, and V_{spike} when a 0.3 mA input current is applied. The frequency remains high at first, then decreases, and finally settles at a low level.

(5) High-order neuron

For an artificial neuron, the order indicates the level of complexity in the neuronal dynamics model. A typical low-order (less than 2) neuromorphic device can only display periodic oscillations and spikes. However, for the simulation of the complete neuromorphic function, at least an order of complexity of 3 is needed to be achieved, and such neurons are called high-order neurons.

Among numerous memristor-based neuronal circuits, the Hodgkin-Huxley (HH) model serves as the foundation for all simplified neuronal models. By mathematically describing the current flow of Na ions, K ions, and leakage currents within the cell membrane, the HH model can accurately depict most biological neuronal electrical signals after parameter adjustment [84]. Wei et al. [85] constructed an artificial spiking neuron using a scalable VO_x Mott memristor circuit to simulate HH neurons. By modeling four processes of the cell membrane—resting state, hyperpolarization, depolarization, and refractoriness—three neuron circuits (i.e., tonic neuron, phasic neuron, and mixed-mode neuron were proposed to generate spiking signals and successfully simulate 23 types of known biological neuron spiking behaviors. However, the use of constant bias voltages, E_{Na} and E_K, limits the integration of the neuron circuit.

Consequently, a high-order neuron implemented with integrated devices was developed. Kumar et al. [75] constructed the first third-order artificial spiking neuron by a nanocircuit which integrates a NbO_x Mott memristor, an internal shunt capacitor, and an internal series resistor, as shown in **Fig. 7(g)** and **7(h)**. This nanocircuit can be modeled by three state variables: the temperature variable T, the voltage v_m across NbO_2, and the switchable ohmic conductor R_{met}. As shown in **Fig. 7(i)**, different neuromorphic electrical signals are observed when varying bias voltages (v_{ext}) are applied to the device. For example, a self-sustained sinusoidal oscillatory signal is generated when v_{ext}=1.8V (bias just below the hysteresis), while periodic two-spike bursting occurs when the bias is within the hysteresis range (v_{ext}= 1.95V). By adjusting the bias voltages, a total of 15 distinct neuron spiking behaviors were observed.

2.2.2 Ion diffusion memristor neuron

(1) Operating mechanism

The ion diffusion memristors rely on the mobile particles responsible for resistance switching [86, 87]. After an electroforming process, a conductive bridge based on the migration of active metal cations is formed, utilizing the on-off state of conductive filaments formed by metal ion migration to achieve memory resistance change [14]. The working mechanism of the ion diffusion memristor is illustrated in **Fig. 8(a)**. The two electrodes at both ends are metals with active (electrochemically active) and inert (inert) chemical properties. The former is usually Ag or Cu, and the latter generally selects W, Pt, Au, Pd, TiN or ITO, etc. Between the electrodes is an insulating material layer as the dielectric layer. Commonly used materials include SiO_2, Al_2O_3, HfO_2, TaO_x, etc. During the electrical forming process, by applying a positive voltage, the active electrode is first ionized into metal ions and migrates along the electric field direction in the insulating layer. When they reach the vicinity of the inert electrode serving as the cathode, these cations obtain electrons and become electrically neutralized, stop migrating and form nanoclusters near the cathode. When the cumulative amount of migration of the above cations is sufficient, a conductive path is formed in the insulating layer, which is also vividly called a conductive bridge. Correspondingly, the device changes from the HRS to the LRS. In the subsequent set and reset processes, the applied voltage controls the on-off state of the conductive filament by controlling the migration of cations, further realizing the modulation of the resistance value of the memristor

A prototypical $Ag/HfO_2/Pt$ ion diffusion TS memristor has been prepared by Lee et al. [88]. Its measured I–V characteristics is shown in **Fig. 8(b)**. When the applied voltage exceeds the threshold voltage V_{th}, the device switches to LRS. If the voltage drops below the holding value V_{hold}, it will shift back to the original HRS. The TS characteristic of ion diffusion memristor makes it a preferable choice to help build neuron circuits with low energy consumption per spike.

(2) Oscillating neuron

Due to the TS property of ion diffusion memristors, they can be used to construct artificial oscillating neurons like the Mott memristors. However, due to the poor endurance of ion diffusion memristors, only few oscillation neurons are recently reported. Recently, Hong et al. proved TS oscillation neurons could be achieved by pure $Nb/SiO_x/Nb$ assembly [89]. Through investigation of the Nb/SiO_x interface and comparative study of the Ar/O gas ratio during SiO_x deposition, the TS property in SiO_x is proved to be attributed the transiently aggregated oxygen vacancies rather than the IMT of Mott memristor. The oscillation neuron is constructed by connecting an ion diffusion memristor in series with a resistor R_L as shown in **Fig.8(c)**.

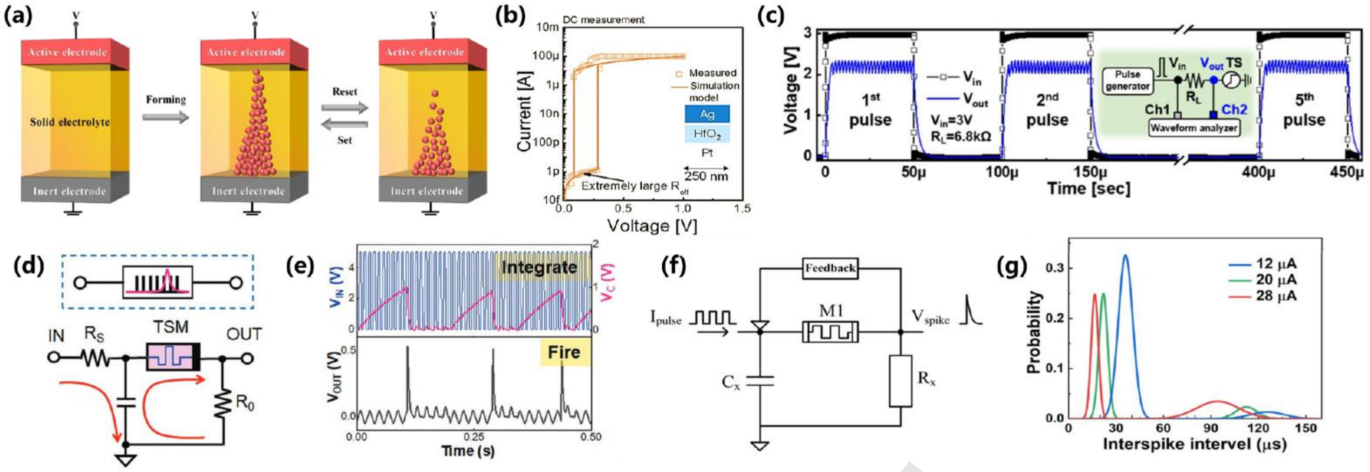

Figure 8 (a) Schematic of the set and reset of ion diffusion memristor, as the resistance change mechanism. (b) A representative threshold switching electrical characteristic loop based on ion diffusion memristor. Reproduced with permission from Ref. [88]. © WILEY-VCH Verlag GmbH & Co. KGaA, Weinheim 2019. (c) Reproducible V_{out} oscillations under the consecutive 5 V_{in} pulses. Reproduced with permission from Ref. [89]. © IEEE 2024. (d) Schematic diagram of the LIF spiking encoder circuit based on Ion-diffusion memristor. (e) Curves of the voltage across the capacitance and the output under a train of input voltage pulses (blue curve).Reproduced with permission from Ref. [90]. © Wiley-VCH GmbH 2022. (f) LIF neuron circuit with feedback module. (g) Fitted curves of probability density distribution upon different current pulse amplitudes. Reproduced with permission from Ref. [91]. © IEEE 2023.

(3) IF & LIF Neuron

Unlike traditional sensing systems, biological systems operate parallelly and use the "spike" instead of the amplitude as its language, which have absolute preponderance in terms of energy efficiency [92].

Employing the TS property of ion diffusion memristors, several IF &LIF Neurons have been implemented. Yoon et al. fabricated a Ag/PZT($PbZr_{0.52}Ti_{0.48}O_3$)/LSMO($La_{0.8}Sr_{0.2}MnO_3$) TS device on the single-crystalline $SrTiO_3$ substrate and used it to represent IF function with stochastic behavior, mimicking the stimulus-strength-dependent spiking probability of a biological neuron [93]. Chen's team built a LIF photoelectric spiking neuron (PSN) with a Ag/TaO_x/ITO ion diffusion memristor, which realizes biological plausibility with a very low spiking rate of no more than 200 Hz and low power consumption of only 0.25–0.5 μW per spike, as shown in **Fig. 8(d)** [90]. The resistor (R_0 = 200 kΩ) and capacitance (C = 10 nF) connected to the memristor mimic dendrites and axons which respectively serve to integrate input spikes from presynaptic neurons and generate spikes. **Fig. 8(e)** delineates the LIF behavior of the ion-diffusion TS memristor in response to a series of voltage spikes.

Simple LIF model neuron circuits with single firing spike fail to attain various firing patterns observed in biological neurons like nonlinear oscillatory neurons in the cerebral cortex. To solve this problem, a compact LIF neuron based on the Ag/Ti/$HfSe_{2-x}O_y$/Pt metallic TS memristor was designed to realize the bionic bursting functions [91]. An ultrathin Ti layer of 3 nm is inserted between the Ag electrode and $HfSe_{2-x}O_y$ resistance switching layer, forming a TiO_x layer due to the transmission of oxygen atoms from HfO_2 to Ti layer, to stabilize the TS property. Consequently, burst firing with different biologically plausible interspike intervals distributions can be realized by adjusting the input of the LIF neuron circuit with the feedback module as shown in **Fig. 8(f)**. The feedback module excites the neuron to restart pulsing after a random period of time after it enters a resting state, thus realizing bionic bursting. As the input current pulse amplitude increases, the number of clusters rises while the number of spikes within each cluster declines. This trend is characterized by a reduction in the main peak and an elevation of the secondary peak as displayed in **Fig. 8(g)**.

2.2.3 Ovonic-threshold-switching (OTS) memristor neuron

(1) Operating mechanism

Although plenty of various novel artificial neurons with great potential are emerging, ovonic-threshold-switching (OTS) memristors are getting more attention lately, which is attributed to low power consumption, superior switching characteristics, high scalability for the integration of perception and computing and intrinsic semiconductor features [94, 95]. The stringent requirements for relatively low off-state leakage(nA) and relatively high on-state current(10MA/cm2) for the selector also make OTS the preferred choice for suppressing leakage current in the one-selector-one-resistor (1S1R) array [96].

As early as 1964, Northover, and Pearson from Bell Telephone Laboratories in the United States first observed in As-Te-I that when the applied voltage reaches a specific threshold voltage (V_{th}), the conductivity rapidly increases to the conducting state [97]. Subsequently, Ovshinsky systematically described the OTS phenomenon based on amorphous $Te_{48}As_{30}Si_{12}Ge_{10}$ and patented his discovery, opening up a new research field [98]. The OTS phenomenon has been found in many disordered materials, especially amorphous chalcogenides with a band gap between 0.6 and 1.4 eV. The functional layer of an OTS is usually an amorphous chalcogenide, and its device structure is a sandwich-like inert metal electrode-amorphous chalcogenide material-inert metal electrode. To date, numerous theories have been developed to explain OTS behavior. However, researchers currently have not reached a consensus on its physical mechanism. The sub-threshold current is described by either Poole, Poole-Frenkel or thermally assisted tunneling and hopping through the mobility gap and the tail/gap states of the amorphous matrix [99]. Under the critical V_{th}, the states are filled and the current increases sharply. In addition, there is also an electric field-induced nucleation model which points out that the reduction of the energy barrier for nucleation and the critical nucleus size by the electric field leads to the spontaneous growth of crystal nuclei, as shown in the schematic diagram in **Fig. 9(a)**. Once the electric field is removed, the energy barrier is restored, and the grown crystal nuclei become unstable and dissolve rapidly. However, note that this conductive-filaments like nucleation model does not fully conform to the crystallization experimental data of OTS, The electrically induced electron defect localization/delocalization transition model is more competent to explain the formation and rupture of conductive pathways [100]. The applied electric field will induce the defects in the localized state to delocalize. The ability of carrier hopping between the defects is greatly enhanced, resulting in a steep drop in resistance, when there are enough delocalized defects. After the applied electric field is removed, the defects will spontaneously return to the localized state, leading to the breakdown of the conduction path.

From the perspective of material design, the incorporation of elements such as Ge, As, Si, C, N, and B can further improve the performance of OTS materials. Commonly used materials, as depicted in the material tree in **Fig. 9(b)**, have three material systems, including Te-, Se-, and S-based ones [96]. D. Lee et al. prepared a common B–Te based OTS memristor and measured its I-V characteristics as displayed in **Fig. 9(c)** [88]. The device initially presents an on-state current at the nA level. Then it undergoes a process of switching between high and low conductance under DC scanning. OTS phenomenon is more like an electronic behavior caused by a secondary thermal effect. The applied voltage can reduce the energy barrier for activating and trapping electrons, thereby increasing the conductivity. Since it does not involve atomic rearrangement like traditional crystalline-amorphous transitions, it does not require the displacement of a large number of atoms in the microscopic environment. Because of this, the high and low resistance switching speed of OTS devices is quite fast, usually on the order of nanoseconds (ns), and the I-V characteristic remains almost invariant. In a well-processed OTS device, its cycle endurance can achieve 10^{10} times with great repeatability. Therefore, it is very suitable for use in neuronal spike generation.

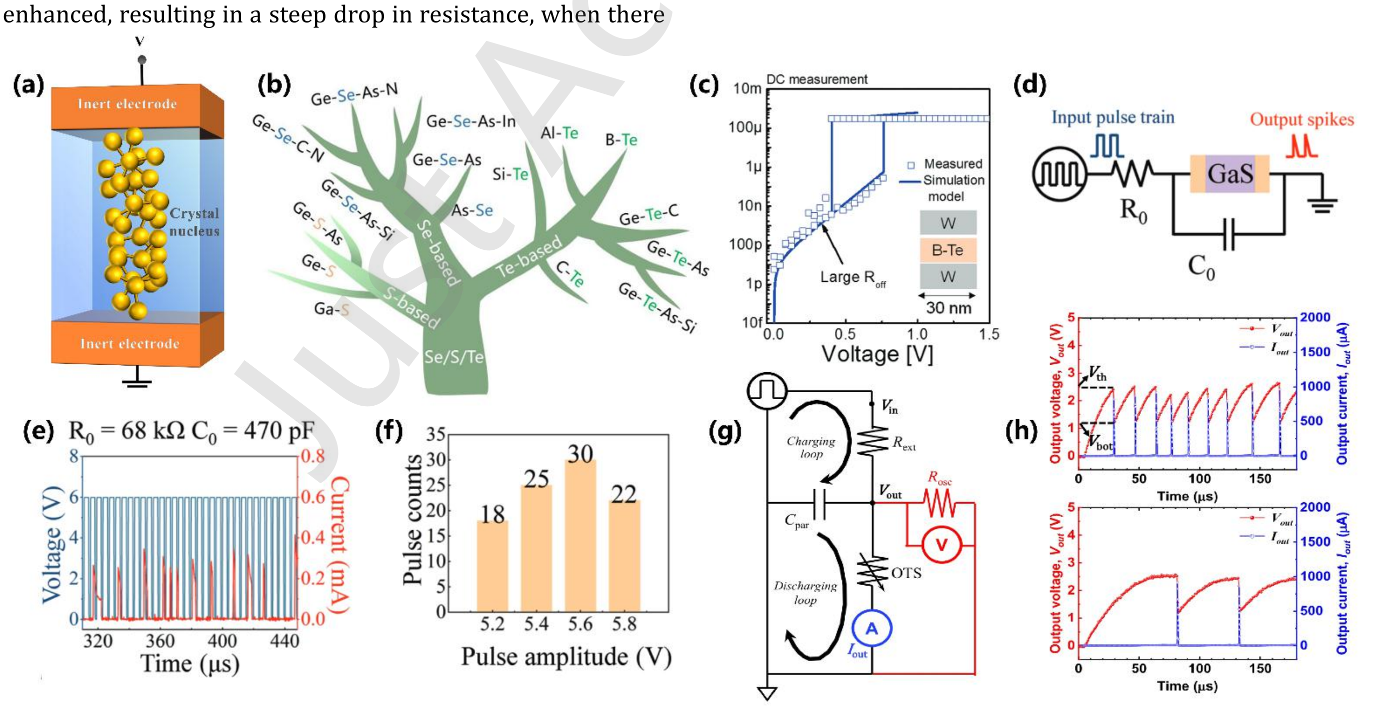

Figure 9 (a) Schematic of the growth of crystal nuclei resulting in the formation of a conductive path, based on the electric field-induced nucleation theory. (b) The OTS material tree. Reproduced with permission from Ref. [96] © Springer Nature 2024. (c) A representative OTS TS electrical characteristic loop. Reproduced with permission from Ref. [88]. © WILEY-VCH Verlag GmbH & Co. KGaA, Weinheim 2019. (d) The LIF spiking neuron circuit based on the GaS OTS device. (e) Characterization of the LIF neuron under a continuous pulse train with certain R_0 and C_0. (f) The firing pulse count varies under different pulse amplitudes. Reproduced with permission from Ref. [101]. © Wiley-VCH GmbH 2022. (g) Schematic to measure oscillation characteristics. C_{par}, R_{ext} and R_{osc} refer respectively to the parasitic capacitor, external resistor, and resistance of an oscilloscope. (h) Measured output voltage (V_{out}) and output current (I_{out}) when R_{ext} is 75 kΩ (top) and 150 kΩ (bottom) at the input voltage (Vin) of 4.2V. Reproduced

with permission from Ref. [102] © American Chemical Society 2024.

(2) IF & LIF neuron

Given that the leakage current is intimately associated with the bandgap of the OTS material and only amorphous OTS materials possess volatile switching properties, binary gallium sulfide (GaS) was selected to realize LIF neurons in Wu et al.'s work [101], which is the most attractive OTS material with a large bandgap of 2.53 eV and a high crystallization temperature about 823K. The binary GaS-based OTS device can provide a large ON current density and low OFF current with high switching speed of ~10 ns. It can even survive under the temperature of 400-450 °C in the back-end-of-line (BEOL) process, as the most conspicuous capacity. The OTS-based LIF neuron is constructed with a capacitor, a resistor and a GaS cell, in which a capacitor (C_0) is in parallel with GaS device to emulate the real cell membrane and loop as illustrated in **Fig. 9(d)**. The spiking behaviors of the neuron shown in **Fig. 9(e)** illustrate the stochastic firing as an essential biological dynamic feature. When the voltage gradually increases from 5.2 V to 5.8 V, the pulse frequency first goes up and then down as shown in **Fig. 9(f)**. This intriguing phenomenon exhibited by the GaS OTS-based neuron may render it a suitable candidate for an artificial afferent nerve.

Jeon et al. [102] presented vertically stackable $Ge_{0.6}Se_{0.4}$ OTS oscillators (VOTS-OSCs) for high-density neuromorphic hardware, which were fabricated by growing Ge0.6Se0.4 film on a contact hole structure with atomic layer deposition technique in a vertical crossbar array (V-CBA) architecture under the fabrication temperature of 400 °C. Measurement indicates that the device first fires at 5.5V then threshold switching happens at 2.5V when applying 10 μs triangular pulses. Following the circuit configuration shown in **Fig. 9(g)**, the oscillation behavior is clearly detected. Charges start accruing in C_{par} until the voltage across OTS reaches the threshold voltage (V_{th}) when Vin is applied, and discharged by threshold switching. Noticeable V_{out}-I_{out} oscillations are generated and the variation law of the spike frequency has been discovered in the repeating process, as described in **Fig. 9(h)**. It indicates that the frequency (f) of oscillations can be modulated by adjustment of Vin and R_{ext}. Higher Vin and lower R_{ext} can boost the charging speed. These oscillation features of VOTS-OSC are applicable for the LIF neuron in SNNs and the coupled oscillator in ONNs.

There is another via-hole structure N-doped SiTe OTS device has been fabricated for the first time by Li et al., which is capable of perceiving and handling ambient information by transforming thermal signals into frequency-coded spikes [103]. By further connecting this OTS device with a resistor and a capacitor, it can be used as a typical LIF neuron. Nitrogen doping greatly optimizes the SiTe OTS device to obtain an ultra-low leakage current of 5.5 nA and ideal power consumption of less than 0.3 nJ per spike. To complete the initial electroforming, a large voltage should be applied to the pristine OTS device. After forming, the leakage current at half of the V_{th} decreases by more than an order of magnitude from 86.8 nA to 5.5 nA due to nitrogen doping, which is critical to the realization of low-power artificial afferent neurons. Variations in the I–V characteristics at different temperatures are tested and the results manifest that the threshold voltage is halved to 0.5 V undergoing a temperature change from 25 °C to 100 °C, which confirmed the sensitive temperature response of the OTS device. Besides, the N-doped SiTe device can surprisingly survive square pulses for approximately 10^7 cycles which is ten times larger than that of a memory cell.

(3) ALIF neuron

An artificial ALIF neuron device composed of an OTS and a few passive electrical components is devised by Lee et al. based on the crosspoint Mo/$Ge_{60}Se_{40}$/Mo sandwich structure [104]. This $Ge_{60}Se_{40}$ OTS device can mimic ample complex behaviors of a biological neuron such as IF, rate coding, the spike-frequency-adaptation (SFA), as well as chaotic activity. Among them, SFA that is ubiquitous in biological neurons can be leveraged to make artificial neural network computations notably more efficient [81]. The device shows that the interspike interval (ISI) gradually increases with the spike counts. The spike frequency also decays exponentially over time, which is highly consistent with the SFA behavior of biological neurons, i.e. progressive elongation of the spiking interval of excitatory neurons in response to steady stimuli.

2.2.4 Phase change memristor neuron

(1) Operating mechanism

The research on the working principle and optimization of phase-change memory (PCM), similar to that of OTS, traces back to Ovshinsky's pioneering work in the late 1960s [98]. A key distinction lies in their material states: OTS devices operate exclusively in the amorphous phase, whereas PCMs rely on reversible transitions between amorphous and crystalline states [105]. A typical mushroom-type PCM structure comprises two inert metal electrodes sandwiching a layer of chalcogenide-based phase-change material (e.g., $Ge_2Sb_2Te_5$ (GST) or Sb_2Te_3 [106]. When a narrow, high voltage pulse is applied, Joule heating drives the phase-change material to an amorphous state at high temperatures, setting the PCM to a high-resistance state (HRS). Conversely, a wide-and-low voltage pulse induces recrystallization at moderate temperatures, switching the device to a low-resistance state (LRS).

PCMs have garnered significant attention in academia and industry as promising non-volatile memory candidates, owing to their fast-programming speed, low operating voltage, excellent data retention, and high endurance for erase/write cycles. Inspired by Ovshinsky's vision of chalcogenide-based brain-like computers in the early 2000s, recent research has focused on leveraging PCMs for neuromorphic applications. Notably, PCM devices can mimic biological synapse behaviors such as spike-time-dependent plasticity (STDP) [107, 108], making their superior switching properties and non-volatility well-suited for neuromorphic computing [109].

Beyond synaptic applications, Tuma et al. [110] first proposed in 2016 that volatile artificial neurons could be constructed using chalcogenide-based phase-change cells to emulate neuronal membranes. By applying continuous voltage pulses, the material in the programmable region gradually transitions from amorphous to crystalline, causing a progressive decrease in resistance, as shown in **Fig.10(a)**. Once the phase change hits the threshold, resistance switches to LRS. Unlike the continuous crystallization process, amorphization is abrupt, necessitating an additional reset circuit to revert the device to HRS when the resistance falls below a threshold, which is a notable limitation of PCM neuron models. The spiking behavior of PCM neurons exhibits stochasticity due to inherent cycle-to-cycle variations in resistive switching, which determine whether the resistance meets the reset firing threshold.

(2) IF & LIF neuron

A simple LIF neuron circuit based on PCM can be constructed by combining a PCM device with two resistors, a capacitor, and a comparator in a series-parallel configuration, providing a template for integration and spike generation. Firing occurs when the integrated circuit voltage V reaches the threshold V_{th}. Postsynaptic excitation requires an additional backpropagation module for membrane potential recovery.

Tuma et al. proposed an innovative hybrid circuit for high-density silicon integration of PCM neurons, combining analog (phase-change devices) and digital (latches and "NOR" gates) components as shown in **Fig. 10(b)** [110]. The operation involves three steps and the typical signal waveforms are provided in **Fig. 10(c)**:

1)When $\overline{\text{WRITE}}$ goes low, V_{INPUT} is triggered and READ is low, V_{DDA} causes a phase change and resistance reduction in the phase change device.

2)When $\overline{\text{WRITE}}$ returns high, V_{INPUT} ceases, and READ goes high, V_{PCD} drops slightly due to voltage division with the reduced-resistance PCM device, but no spiking signal is produced as the D latch still outputs high.

3) Repeated PCM setting cause V_{PCD} to drop below threshold θ_v, triggering the D latch to output "0". A subsequent low $\overline{\text{WRITE}}$ generates a high-level SPIKE signal. Following an optional refractory period, the membrane potential is restored by a reset pulse, after which the cycle repeats. The firing rate can be controlled by adjusting the power and width of the crystallizing pulse as shown in **Fig. 10(d)**. Fabrication-induced variations in PCM physical properties lead to random distributions in firing rates, which emulate neural noise and stochastic dynamics and is critical for constructing dense neural populations that robustly represent signals.

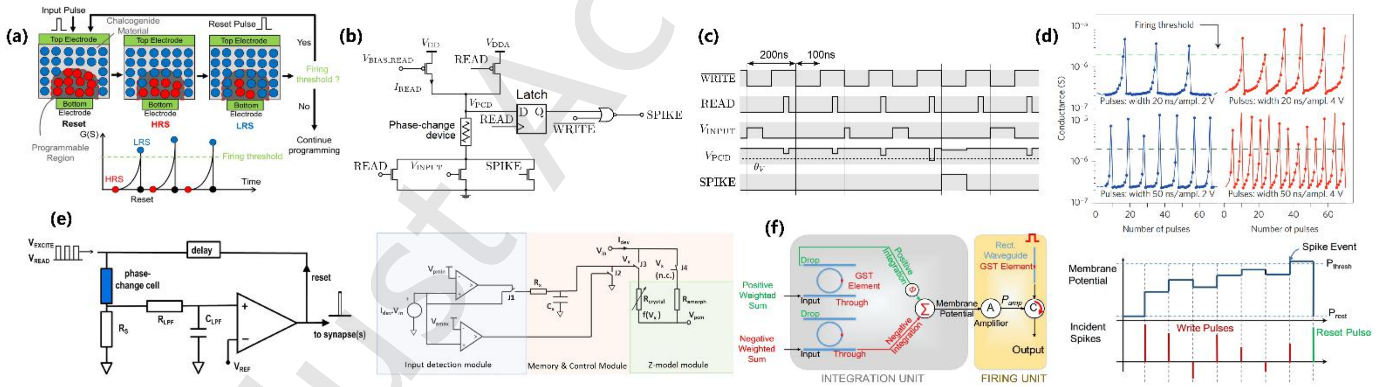

Figure 10 (a) Demonstration of spike generation mechanism in phase change neuron devices [110, 111]. Reproduced with permission from Ref. [110, 111]. © Wiley 2021. (b) Specific implementation of neuron circuit based on phase-change device. The main control signals in the figure are $\overline{\text{WRITE}}$ and READ. V_{INPUT} is the input signal and SPIKE is the output signal. V_{PCD} is the input signal of the D latch. (c) Schematic diagram of typical signal waveforms in the neuron circuit. (d) The integrate-and-fire process of a phase-change neuron controlled by different amplitude and duration of the crystallizing pulses. Reproduced with permission from Ref. [110]. © Springer Nature 2016. (e) Left panel: self-resetting IF PCM-based spiking neuron SPICE model; Right panel: details of the SPICE PCM cell model. Reproduced with permission from Ref. [112]. © IOP Publishing 2018. (f) Schematic diagram of the bipolar IF neuron and timing diagram revealing the relationship between the integration of membrane potential and the operation of the proposed neuron. Reproduced with permission from Ref. [113]. © Springer Nature 2018.

IF PCM-based spiking neuron has been constructed by employing a delay module [110]. Because the physical attributes of the PCM are more or less disparate attributed to fabrication differences, firing rates of the neuron appear to have a random distribution. This ability that emulates neural noise and stochastic neural dynamics at the device level is the key to the establishment of dense neural populations for robust representation of signals. Later, Cobley et al. presented a straightforward circuit model that could mimic an IF neuron with the self-resetting feature on the basis of PCM cell and SPICE model integration, as shown in **Fig. 10(e)** [112]. The core approach is to utilize the high-level output voltage generated by the comparator to re-amorphize the device. This is fed back to the phase-change unit through the delay block. the SPICE PCM model includes three core sub-modules. The input detection module detects the input programming voltage pulse and generates appropriate input voltages (V_{reset} or V_{set} or V_{preset}) for the memory & control module. The memory & control module is responsible for controlling the Z-model module to select the programming state of the PCM cell, such as fully crystalline, fully amorphous, or partially crystalline. This circuit simulated spiking frequencies from 0.5 to 4 MHz which far exceeds biological neural rates.

In order to evade the problem of energy limitations in the electrical domain due to high 'write' times for PCMs in the electrical domain, Indranil et al. presented an all-photonic phase-change spiking neuron employing the GST-embedded ring resonator which was made up with wo rectangular waveguides and a ring waveguide [113]. Wave entering through the INPUT gate gets partially coupled to the ring waveguide and constructively interferes inside the ring when the resonant condition is fulfilled. The GST element introduced above the ring waveguide of the ring resonator enabled us to control the propagation of light through the port by merely changing the state of the GST. Light instantaneously coupled to the GST element through the waveguide is differentially absorbed by the GST in its low-loss amorphous and highly doped crystalline states. Therefore, transmission of the 'THROUGH' and 'DROP' ports can be integrated in opposite direction to emulate the resultant integration. After further process of an interferometer, resultant integration is based on both the positive and negative inputs to the neuron body and can be treated as membrane potential of the IF neuron. The corresponding schematic is provided in the left part of **Fig. 10(f)**. The value of membrane potential integration is proportional to the amplitude of the incident spike to the neuron, as shown in the right part of **Fig. 10(f)**. Later Kumar et al. [114] presented a CMOS-PCM thermosensory spiking neuron circuit for bio-inspired sensing. The neuron shows linear output frequency variation with temperature and works in 0–80 °C, suitable for AI robots in industrial applications.

2.2.5 Self-Rectifying Memristor Neuron

Crossbar arrays are favored for high-density neuromorphic computing. However, sneak path currents in passive arrays degrade read margins and limit the scalable array size [115-117]. Self-rectifying memristors (SRMs) [118-120] leverage intrinsic nonlinearity to suppress these currents without additional components, enabling high-density 3D integration. Consequently, Rectification Ratio (RR) and Nonlinearity (NL) [121, 122] are critical metrics for evaluating leakage suppression and maximizing integration scale. Synaptic SRMs are widely investigated. Luo et al. [123] modeled a $Pt/TaO_x/Al_2O_3/TiN$ device to design a secure PUF circuit, achieving 50.1% uniqueness and 99% reliability. Zhang et al. [124] enhanced a $TiN/HfO_x/Pt$ structure via RTA, achieving the highest reported rectification ratio (10^8) and nonlinearity (10^5). This high-performance device enabled an autonomous driving system that retains high accuracy even under adversarial attacks.

Regarding the construction of Leaky Integrate-and-Fire (LIF) neurons, Park et al. [125] proposed an SRM neuron based on a gradual TiO_x structure in 2022. This work innovatively utilized an anodizing process to create a vertical oxygen concentration gradient within the TiO_x layer, physically shifting the resistive switching mechanism from localized stochastic filament formation to oxygen anion migration within the bulk phase. This fundamental shift in mechanism significantly suppressed stochasticity, with experimental measurements showing cycle-to-cycle (C2C) variation as low as 1.39% and device-to-device (D2D) variation of only 3.87%, achieving a near 100% yield in a 20×20 array. The constructed LIF neuron array system successfully realized the generation and processing of complex sequential data, such as antimicrobial peptide sequences, by leveraging dynamic response differences under varying pulse widths. In 2025, Cai et al. [126] developed a multifunctional SRM based on a $Pt/TiO_xN_y/HfO2/W$ structure. By exploiting the differences in thermal effects and ion migration responses under different pulse widths, this device achieved dynamic functional reconfiguration within a single device: it behaves as a typical LIF neuron under short pulses (10 μs), while transitioning into a nociceptor with threshold and sensitization characteristics under long pulses (>100 μs). Notably, the device exhibits an ultra-low energy consumption of only 0.8 fJ/spike in LIF mode and a leakage current as low as 100 pA. While maintaining a high rectification ratio (10^5) and a large on/off ratio (10^4), it achieves extremely high energy efficiency and functional density, demonstrating immense potential for application in ultra-low power sensing-memory-computing integrated systems.

2.3 Transistor-based artificial spiking neurons

2.3.1 Single Transistor Latch phenomenon

(1) Operating mechanism

A single transistor latch (STL) can cause an abrupt transition from a HRS to a LRS in the I_{DS}–V_{DS} characteristics of a transistor, primarily driven by impact ionization. This mechanism in bipolar transistors and MOSFETs has been leveraged to construct artificial spiking neurons.

Yun et al. [127] fabricated a bipolar transistor (**Fig. 11(a)**) and characterized its I-V behavior by grounding the emitter and sweeping the collector voltage. As shown in **Fig. 11(b)**, when the voltage exceeds V_{LU}, the current abruptly increases, switching the transistor to LRS; when the voltage drops below V_{LD}, the current drops sharply, reverting to HRS.

This threshold resistance change arises from the STL phenomenon. The underlying mechanism (**Fig. 11(c)**) involves voltage-induced lowering of the collector energy band, thinning the base-collector potential barrier. When the barrier becomes sufficiently thin, massive carrier transport occurs, causing the abrupt current jump in the I-V curve.

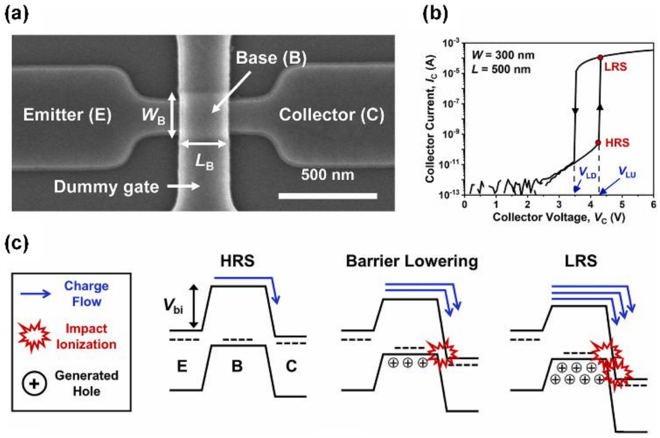

Figure 11 Electrical mechanism and operating characteristics of single transistor-based artificial spiking neuron. (a) SEM diagram of the single bipolar transistor-based artificial spiking neuron. (b) output characteristics of a single transistor. (c) energy band diagram corresponding to the transistor latch-up phenomenon. Reproduced with permission from Ref. [127]. © Elsevier Ltd 2023.

(2) Oscillating neuron

The circuit structure of a single transistor neuron is shown in **Fig. 12(a)** [128], where the transistor is connected in series with a resistor R_L, and an oscillating voltage spiking signal can be generated at the output by using its own parasitic capacitance. Applying a constant V_{DD} at one end of the resistor and measuring V_{out}, the transistor jumps back and forth between the high and low resistance states driven by the current signal generated by the voltage signal through the resistor, thus generating oscillating voltage spiking signals at both ends of the transistor. The output voltage spiking signal exhibits a steady amplitude oscillation over time, as shown in **Fig. 12(b)**. Meanwhile, when only increasing the series resistance RL, the oscillation frequency decreases, as shown in **Fig. 12(c)**; when only increasing the supply voltage V_{DD}, the oscillation frequency increases, as shown in **Fig. 12(d)**.

In order to explore the possibility of generating oscillating signals from a single MOSFET, J. Han et al.[129] fabricated on a block silicon wafer, and its I_{DS}-V_{DS} characteristic curve is shown in **Fig. 12(e)**. Unlike conventional voltage-input, current-output MOSFETs, this MOSFET is current-input, voltage-output. The current input between HRS and LRS affects the drain and source side energy barriers between n^+D, n^+S and the p-type body to change the output voltage by changing the motion of holes and charges, and the positive feedback loop thus generated can produce a wedge oscillation waveform with a certain frequency. Parallel connection of this MOSFET with a capacitor C_{par} (**Fig. 12(f)**) containing parasitic capacitance produces oscillating waveforms at different input currents I_{in} as shown in **Fig. 12(g)**. It can be seen that as the input current I_{in} increases, the oscillation frequency increases, which can be expressed by

$$f = \frac{I_{in}}{C_{par} \cdot V_{pp}} \tag{12}$$

where C_{par} is parasite capacitance and V_{pp} is the peak-to-peak value and is equal to (V_{LU}-V_{LD}).

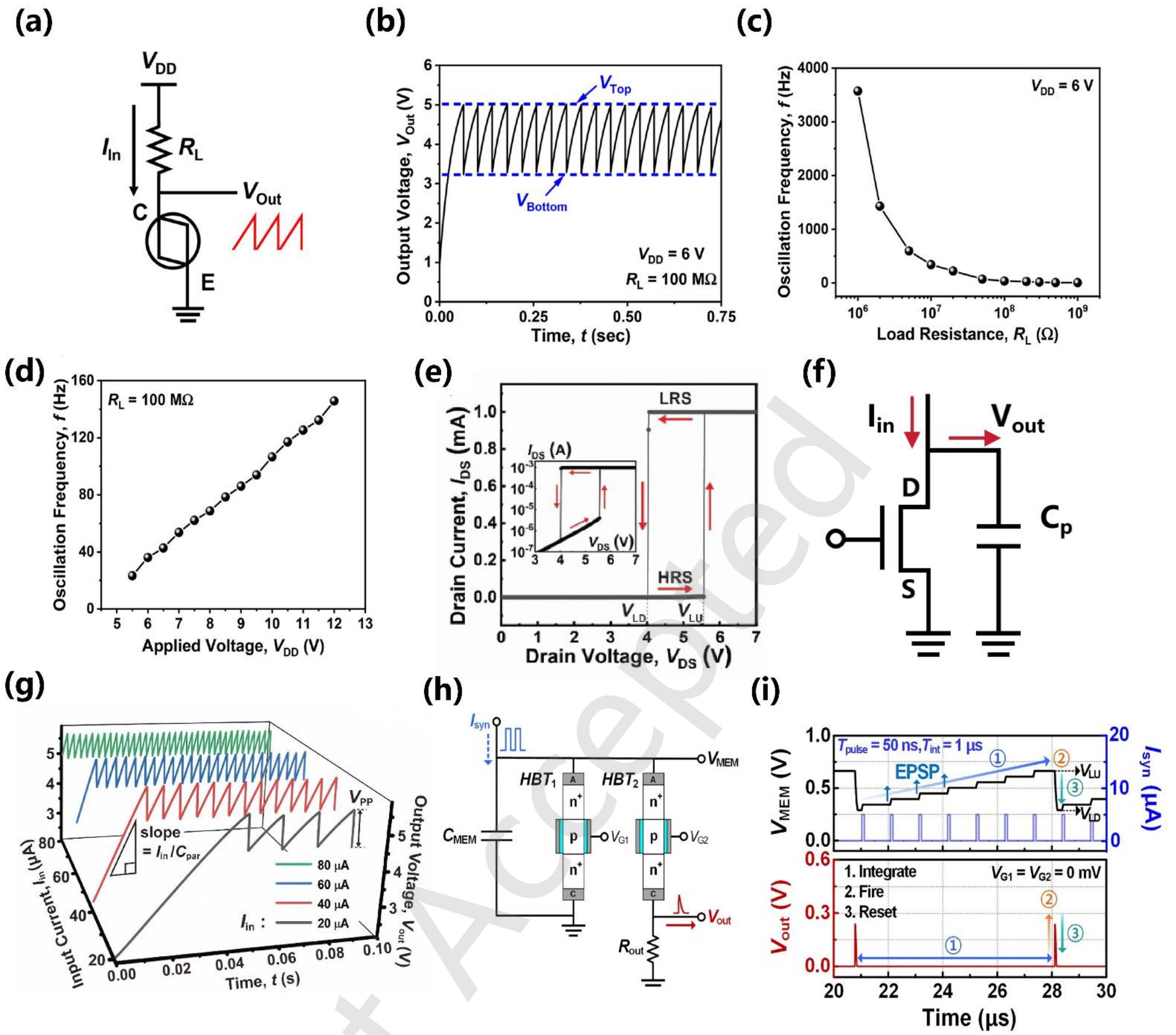

Figure 12 Electrical operating characteristics of a single gate transistor-based artificial spiking neuron. (a) Circuit structure of a single bipolar transistor-based neuron. (b) Output voltage spiking signals of a single bipolar transistor-based neuron. (c) Relationship between the oscillation frequency and the series resistance R_L. (d) Relationship between the oscillation frequency and the supply voltage V_{DD}. Reproduced with permission from Ref. [128]. © American Chemical Society 2024. (e) Output characteristics of a single MOSFET. (f) Circuit structure of a single MOSFET-based neuron. (g) Output voltage spiking signals of a single MOSFET-based neuron. Reproduced with permission from Ref. [129]. © IEEE 2024. (h) SiGe-HBT-based IF neuron circuit. (i) Output signals under input pulsed signals. Reproduced with permission from Ref. [130]. © Springer Nature 2024.

(3) IF neuron

In addition to this, some novel structured transistor-based artificial spiking neurons utilizing the STL phenomenon have been proposed. Mori et al. [131] designed a PN-body tied (PNBT) silicon-on-insulator field-effect transistor (SOI-FET), which implements the integrate-fire (IF) neuron function. The body resistance is high in the initial state, the body terminal is charged at the input of I_{in}, and the device enters into the latch-up mode after positive feedback occurs, the body resistance is lowered, but the device also possesses the function of amplifying the signal at the drain. Kim et al. [130] proposed a spiking neuron based on silicon-germanium heterojunction based bipolar transistors (HBTs) with nanowire structure and the circuit consists of two HBTs, a resistor and a capacitor, as shown in **Fig. 12(h)**. This neuron can achieve periodic IF behavior without an external resetting circuit. In this circuit the capacitor acts as the integrating unit and the two HBTs act as threshold triggers for the spiking discharge and self-reset process. The resistor generates the output voltage signal. During the integration process, the input I_{syn} charges the capacitor so that the VMEM increases to the latch-up voltage of the HBTs and then enters into the on state from the off state. The decrease in the resistance of the HBT2 leads to an increase in the voltage across the output resistor. The sharp increase in V_{out} indicates that the spike is discharged. At the same time I_{syn} stops charging the capacitor and the capacitor starts discharging and VMEM decreases. As V_{out} increases, the potential difference between HBT_2 decreases eventually switching off, V_{out} decreases to 0 and the spike eventually forms. Thus this neuron can achieve periodic Integrate-Fire (IF) behavior without an external resetting circuit as shown in **Fig. 12(i)**.

(4)LIF Neuron

Han et al. [132] presented the first LIF neuron realized with a single MOSFET. When the device gate voltage is set, different oscillating signals can be generated when different drain currents I_{in} are input. This kind of different pulse characteristics generated by controlling the gate can improve the classification accuracy of the device.

2.3.2 Multiple-gate transistor

Single-gate MOSFETs lack the capability to emulate neuronal inhibition, necessitating the integration of additional gate terminals to expand functional complexity. Han et al. [133] addressed this by developing a double-gate MOSFET for artificial spiking neurons. The device incorporates two independent gates: the primary gate controls excitatory/inhibitory states, while the secondary gate modulates spiking dynamics. When a 1 V voltage is applied to the primary gate, the neuron enters an inhibitory state, suppressing voltage pulse output. Conversely, a 0.5 V primary gate voltage activates the excitatory state, where the peak-to-peak amplitude of output voltage pulses decreases with reduced secondary gate voltage. Simultaneously, spiking frequency increases with input current and further escalates with higher secondary gate voltages.

Ding's team [134] advanced this concept with a vertical silicon nanowire-based cylindrical double-gate MOSFET. The device features independently controlled inner and outer gates: the outer gate selectively inhibits neuronal activity, mimicking lateral inhibition in retinal amacrine-to-ganglion cell signaling, while the inner gate adjusts the firing threshold voltage. Leveraging the STL phenomenon, input current injection drives charge/discharge cycles, generating wedge-shaped oscillatory waveforms characteristic of biological spiking dynamics.

2.3.3 FeFET

Hafnium oxide (HfO_2)-based ferroelectrics have emerged as the preferred choice for artificial neurons due to their superior scalability and CMOS compatibility compared to traditional perovskite ferroelectrics [135-141]. Fundamentally, FeFETs operate by modulating the channel conductance through the reversible polarization switching of the ferroelectric gate dielectric under an applied electric field, thereby enabling the emulation of neuronal spiking thresholds [142-147].

Li et al. [148] developed a relaxation oscillator using a metal-ferroelectric-metal-insulator-semiconductor (MFMIS) double-gate FeFET **(Fig. 13(a))**. Applying a pulsed voltage to the drain generates oscillatory waveforms **(Fig. 13(b))**, with frequencies increasing from 0.6 V to 0.8 V gate voltage. Rajasekharan et al. [149] designed an artificial neuron circuit using a FeFET to emulate FitzHugh-Nagumo (FHN) dynamics, which closely approximate Hodgkin-Huxley (HH) neuron behavior. This circuit **(Fig. 13(c))** captures biological phenomena like excitation block and anodal break excitation. To reduce hardware complexity,Lee et al. [150] proposed a single-transistor leaky integrate-and-fire (LIF) neuron using a Single-Device Leaky-FeFET (SD L-FeFET,). By leveraging directional ferroelectric polarization switching, this approach simulates both excitatory and inhibitory inputs within a single device, achieving biologically plausible dynamics while eliminating the need for additional circuitry.

2.3.4 AFeFET

Anti-ferroelectric field-effect transistors (AFeFETs) employ antiferroelectric materials like $Hf_{0.2}Zr_{0.8}O_2$ as gate dielectrics, distinguishing themselves from conventional ferroelectrics by their inherent volatility—polarization relaxes to a neutral state upon voltage removal. This property enables fast, autonomous resetting without additional circuitry, in contrast to non-volatile FeFETs, which require feedback loops or specialized ferroelectric layers for reset, increasing hardware complexity, energy consumption, and cost.

Cao et al. [151] demonstrated a leaky integrate-and-fire (LIF) neuron using AFeFETs, achieving leaky neuron functionality without external capacitance or reset circuitry **(Fig. 13(d))**. Sun et al. [29] further developed an amorphous-indium-gallium-zinc-oxide (a-IGZO) AFeFET-based LIF neuron **(Fig. 13(e))**, where inherent volatility yields near-zero residual polarization (Pr) upon voltage removal, enabling simultaneous emulation of excitatory and inhibitory inputs**(Fig. 13(f))**.

Endurance is a critical bottleneck for neuromorphic hardware due to the high-frequency spiking requirements. Conventional FeFETs are typically limited to 10^5 cycles [152], constrained by charge trapping and wake-up effects from forced reset operations. In contrast, AFeFETs leverage the intrinsic volatility of the antiferroelectric phase for spontaneous depolarization, eliminating the need for aggressive resets. This self-resetting mechanism mitigates dielectric stress, extending endurance to 10^{12} cycles [151]. **Fig. 13(g)** visualizes this polarization fatigue contrast, highlighting the orders-of-magnitude advantage of AFeFETs for long-term applications.

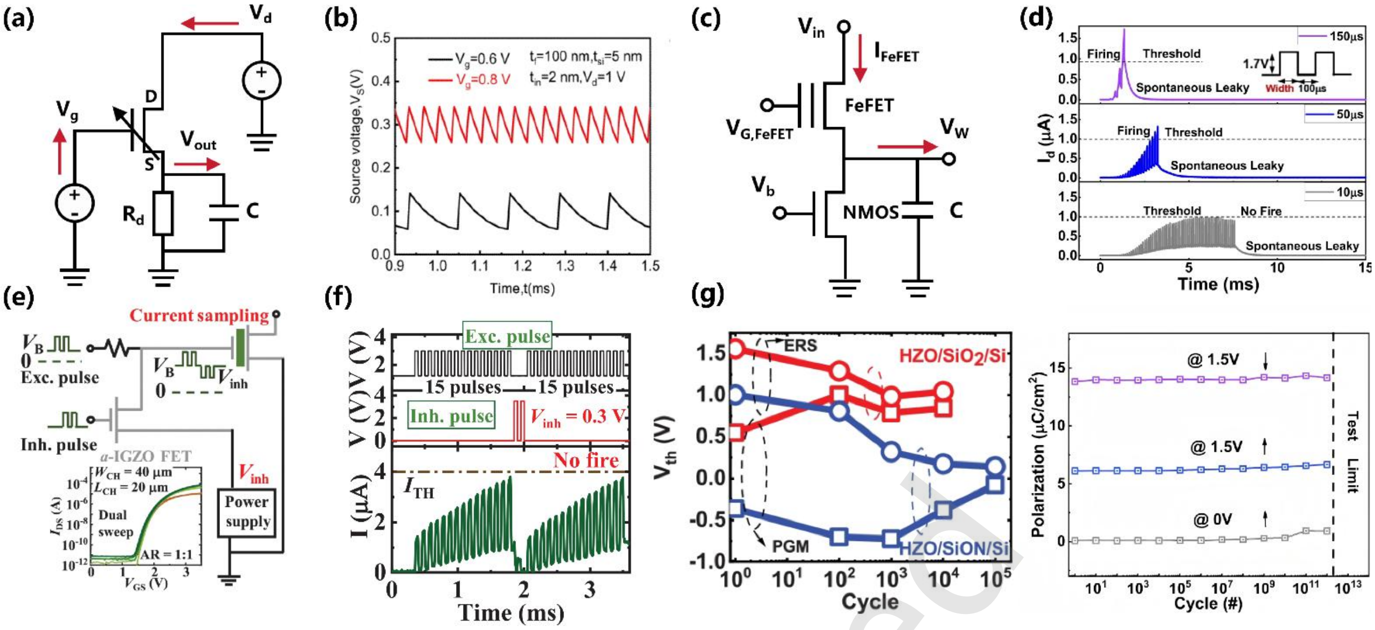

Figure 13 FeFET-based artificial spiking neuron and its electrical characteristics. (a) Schematic of the 1F1R1C relaxation oscillator circuit. (b) Output voltage spiking signals from 1F1R1C relaxation oscillator with different input gate voltages. Reproduced with permission from Ref. [148]. © IEEE 2023. (c) FeFET-based FHN neuron oscillator circuit. (d) Output signals under the input of excitation pulse signals. Reproduced with permission from Ref. [151]. © Springer Nature 2022. (e) Circuit of a-IGZO AFeFET-based LIF neuron. (f) Output signals when excitation signals are input at the same time as inhibition signals Reproduced with permission from Ref. [29]. © IEEE 2022. (g) Polarization fatigue graphs of FeFET (left) and AFeFET (right). Reproduced with permission from Ref. [152]. © IEEE 2021.

2.4 2D material-based artificial spiking neurons

In addition to the above two categories, 2D materials are emerging as an important enabling platform for artificial spiking neurons, although most 2D neuromorphic studies have so far emphasized synaptic devices and plasticity [40, 153-156]. Owing to their atomically thin body and strong electrostatic gate control, together with the high tunability of defects, interfaces, and ionic environments, 2D materials can be employed as the active channel or the sensory transduction layer to implement leaky integration, threshold triggering, firing rate modulation, and stimulus to spike encoding with reduced circuit overhead [41, 157, 158]. Furthermore, their optoelectronic response and carrier trapping dynamics facilitate direct coupling to sensory front ends, enabling event driven spiking outputs that are well suited for downstream spiking neural network processing. In practice, the required nonlinearity and spatiotemporal dynamics are commonly introduced through van der Waals heterostructures or hybrid integration with ferroelectric layers, ionic conductors, and threshold switching elements [43, 159].

2.4.1 IF & LIF neuron

2D semiconductors enable compact device–circuit co-design of IF or LIF neuron units. Using a wafer-scale monolayer MoS_2 film, Wang et al. [160] integrated a DRAM capacitor with a MoS_2 inverter to implement a biologically inspired IF neuron, as shown in **Fig. 14(a)**. The capacitor stores charge as the membrane potential, and inverter switching produces a spike once the voltage reaches the threshold. Write voltage (V_W) programs the initial membrane state, thereby emulating intrinsic plasticity by tuning neuronal excitability. In parallel, selected voltage (V_S) regulates leakage-mediated integration dynamics, broadening the time-to-first-spike (TTFS) tunability as shown in **Fig. 14(b)**, which supports light and dark adaptive encoding. Owing to MoS_2 photosensitivity, optical intensity can be directly mapped to TTFS. The device reports a spike energy of 2.82 nJ within a 100 ms TTFS window, highlighting its energy-efficient potential for sparse temporal coding.

Li et al. [161] constructed a TS-FET by serially integrating a volatile threshold switch with a gated 2D MoS_2 channel, further compressing LIF dynamics into a single spiking transistor as displayed in **Fig. 14(c)**. The excitatory voltage pulse amplitude can tune the firing frequency as illustrated in **Fig. 14(d)**. MoS_2 serves simultaneously as a scalable transistor channel and an optoelectronic gating element, enabling light-programmable excitability: spiking is inhibited in darkness, whereas illumination reduces the channel resistance and facilitates firing. The device achieves nanowatt-level power consumption (3.75 nW in the inhibited state), highlighting its suitability for energy-efficient neuromorphic vision front ends.

Similarly, in the photoresponse-driven pathway, Aung et al. [44] exploited carrier photogeneration in monolayer MoS_2 phototransistors and the subsequent exponential relaxation after illumination removal to emulate membrane charging and leakage, respectively. Gate control was further employed to enable rapid reset, thereby completing the reset operation required for LIF dynamics. By contrast, the WSe_2

platform highlights neuron–synapse co-integration enabled by polarity control and ferroelectric coupling. Huo et al. [162] leveraged the short retention and volatile polarization states of WSe_2 p-FeFETs to realize fast-release transient programming, in which spike generation emerges from pulse accumulation and the device autonomously returns to its initial state upon stimulus withdrawal, consistent with the leakage and self-reset characteristics of LIF neurons. In addition, reconfigurable van der Waals heterostructures provide a programmable hardware substrate for multifunctional neuromorphic primitives. Specifically, the 2D MoS_2/graphene/hBN platform proposed by Hu et al. can be reconfigured into synaptic, dendritic, and neuronal modes via terminal configuration [163]. In the two terminal memristive mode, Ag-ion migration in hBN induces conductance switching with volatile evolution, giving rise to IF spiking and enabling reprogrammable implementation of multiple neural information processing building blocks within a single device unit.

2.4.2 E-I LIF neuron

Neurons do not operate independently, but are linked to combinations of neurons or circuit motifs that process specific sorts of messages [164]. Inspired by this population behavior of neurons, Li et al. worked on core processing neurons with a variety of synaptic excitatory-inhibitory (E-I) connectivity patterns [165]. As one of the basic neuronal circuit motifs, the E-I connectivity pattern can further enable parallel, power-efficient computing like human brain. By combining the gated-controlled field-effect and volatile resistive switching, a compact neuron emulates these essential neuronal behaviors (e.g. LIF and inhibition) and synchronously processes complex spatiotemporal E–I information.

The proposed core processor is composed of a 2D semiconducting MoS_2 field effect channel with a drain-end-embedded volatile ECM threshold switch, in which the Al_2O_3 layer serves as both high-κ gate dielectric for the MoS_2 channel and reliable electrochemical switching layer in the TS device as displayed in **Fig. 14(e)**. In order to realize coherent perception, the brain needs to integrate multisensory signals from the same event and segregate signals from different events, with temporal synchrony being critical. As a basic neuronal circuit motif, feedforward inhibition enhances the temporal precision of neurons by narrowing the time window for the suprathreshold summation of excitatory signals. In its mechanism, inhibitory and excitatory signals converge on postsynaptic neurons as shown in **Fig. 14(f)**, and excitatory inputs must occur within a specific time window to trigger a spike. This time window controls the temporal resolution of neuronal integration and shapes temporal precision as illustrated in **Fig. 14(g)**.

2.4.3 Analog neuron

Unlike typical LIF spiking neurons, which generate pulse outputs through discrete events including integration, threshold triggering, discharge reset, and a refractory period, analog neurons generally do not emphasize explicit spike generation. Instead, they use continuous device state variables, such as current, voltage, or conductance, as a physical representation of the membrane potential. Because the output varies continuously with the input in a graded manner, these neurons can perform dynamic-range compression, temporal integration, and feature extraction directly at the sensing front end, thereby reducing reliance on downstream spike generation and digital preprocessing.

A representative example is the optoelectronic graded-neuron array reported by Chen et al. [159]. In this work, the MoS_2 phototransistor exhibited in **Fig. 14(h)** emulates the characteristics of the graded neuron as shown in **Fig. 14(i)**, where the graded response arises from charge dynamics dominated by shallow trap centers, resulting in sublinear and compressive photoelectronic outputs. More importantly, the characteristic time constant can be widely tuned by the gate bias, enabling temporal resolutions spanning approximately 10^1–10^6 ms and accommodating motion perception across a broad range of speeds. At the array level, such continuous outputs allow multi-frame temporal information to be encoded and integrated locally at the pixel, thereby capturing motion trajectories with reduced data redundancy and alleviating the computational burden of downstream processing. Beyond optoelectronic transistors, accumulative electrochemical devices can also implement analog neuronal functions. Liang et al. [166] reported a MoO_x–Nafion three-terminal ECRAM (electrochemical random-access memory), where gate pulses drive reversible ion and proton migration between the electrolyte and the channel to modulate conductance. Under pulsed stimulation, the conductance acts as an integrable state variable that accumulates with successive pulses and can be read out as a continuous current output.

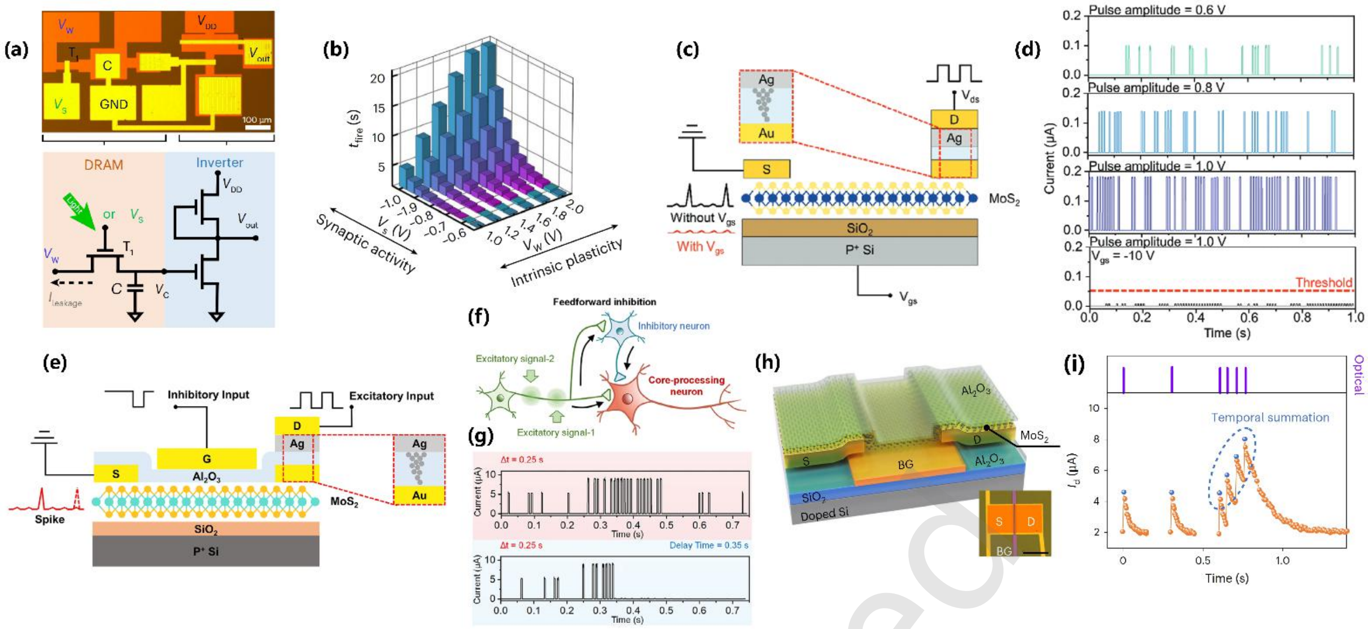

Figure 14 (a) Optical micrograph and the circuit schematic of a versatile neuron module combining a DRAM cell with a MoS_2 transistor-based inverter. T1 serves as the DRAM access transistor. (b) Tuning of t_{fire} on the same device through adjustment of synaptic activity and intrinsic plasticity, denoted by V_S and V_W, respectively. (c) The operating principle of the threshold-switch embedded MoS_2 channel phototransistor under excitatory stimulation applied at the drain and inhibitory modulation applied at the gate. (d) The firing characteristics of the device under stimulus pulses with different amplitudes and V_{gs} (pulse interval: 5 ms, pulse width: 5 ms). Reproduced with permission from Ref. [160]. © Springer Nature 2025. (e) Schematic diagram of the single-transistor neuron with excitatory and inhibitory input signals. (f) The feedforward inhibition model involves an inhibitory neuron receiving input from a presynaptic excitatory neuron and sending inhibitory outputs to a postsynaptic neuron. (g) Raster plot of firing patterns over time without(red) and with(blue) inhibitory signal applied, Δt = 0.25 represents that only half of the excitatory signals are synchronized and enhanced. Reproduced with permission from Ref. [165]. © John Wiley & Sons 2024. (h) Schematic of the MoS_2 phototransistor, with an inset optical micrograph of the device. (i) Time-resolved photocurrent response to a single light pulse (660 nm, 5 mW cm^{-2}, 10 ms), measured at V_{ds}=0.1V and V_g=0V. "Optical" denotes the light stimulus. Reproduced with permission from Ref. [159]. © Springer Nature 2023.

3 Neuromorphic perception and computing system based on artificial spiking neurons

Among many artificial neural networks, SNN is a neural network that efficiently simulates the working mode of human brain [3, 167]. And spiking neuromorphic perception systems (SNPS) is the best match for the SNN. As shown in **Fig. 15**, in order to convert the analog signals in the environment into spiking signals that can be recognized by SNNs, traditional sensing architectures require a large number of sensors and ADCs; however, faced with the task of processing massive amounts of sensing data, ADCs need to have high conversion efficiency and accuracy, which leads to most of the circuit area being occupied by ADCs, resulting in inefficient utilization of the chip area, high power consumption, and long latency. Moreover, voltage to frequency converters (VFCs) are needed to converter the output of ADCs to SNN. These problems seriously limit the development of SNNs. Therefore, the development of SNNs will be accelerated by employing novel electronic devices to construct simple spike-encoded neuromorphic perception systems. This section will first describe how to construct a neuromorphic sensing system based on artificial spiking neurons to realize artificial tactile, visual, olfactory, gustatory, auditory, and thermal receptors as shown in **Fig. 16**. Then the neuromorphic computing system will be reviewed.

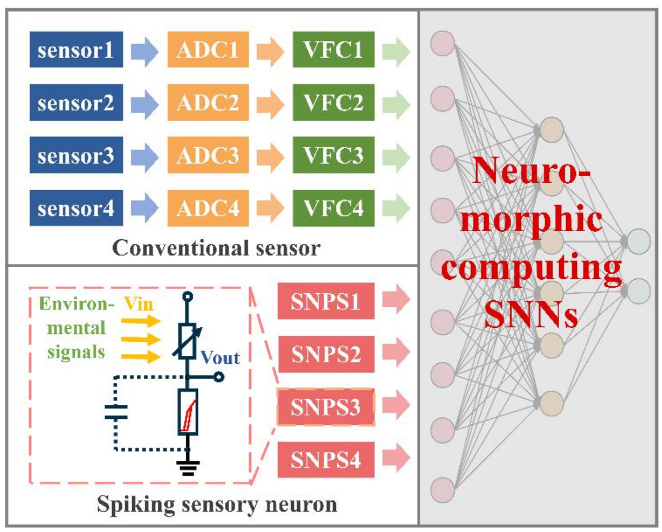

Figure 15 Conventional sensor SNNs and Spiking sensory neuron SNNs

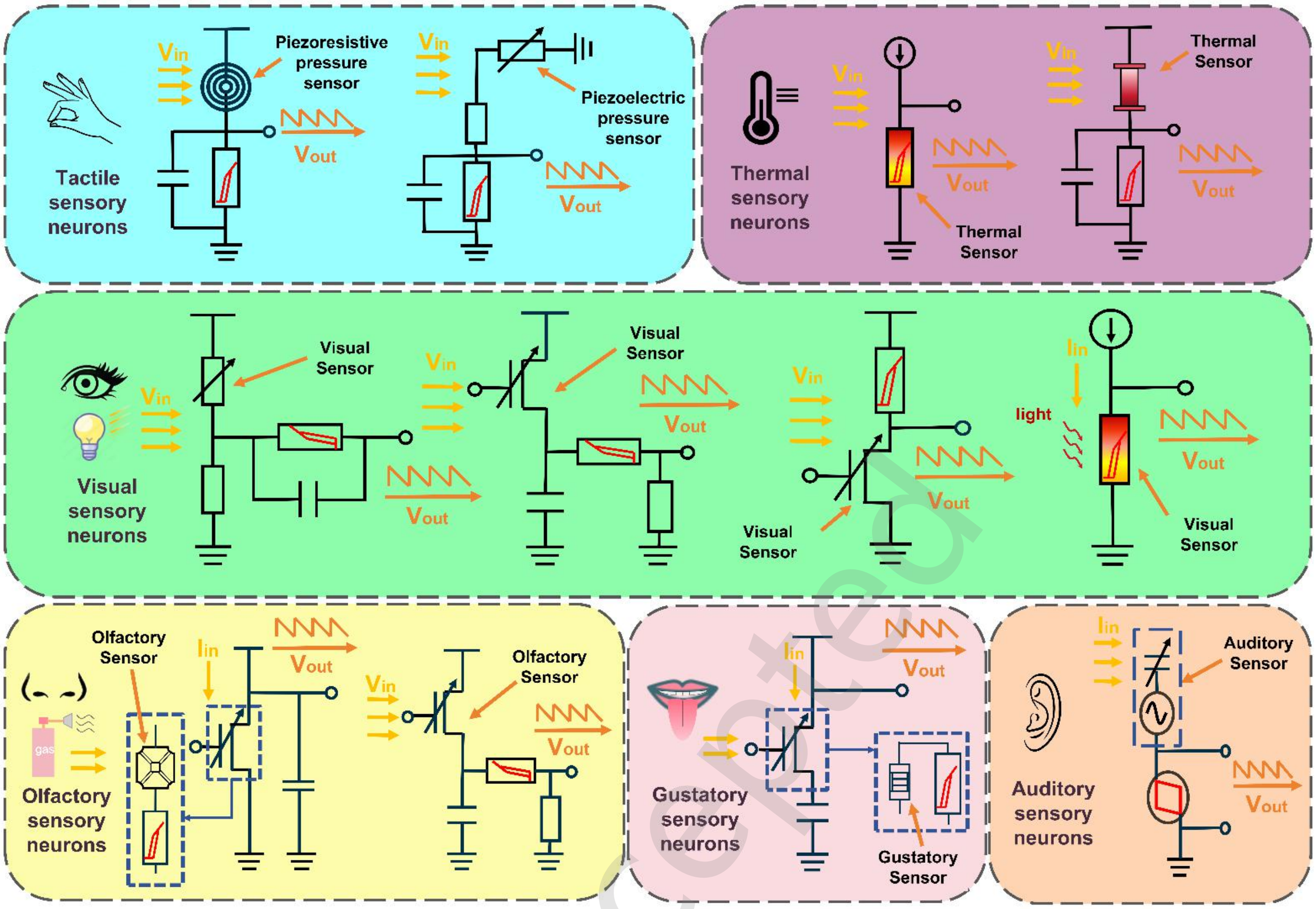

Figure 16 The structures of neuromorphic perception system, (a) tactile sensory neuron, (b) thermal sensory neurons, (c) visual sensory neuron, (d) olfactory sensory neuron, (e) gustatory sensory neuron, (f) auditory sensory neuron.

3.1 Neuromorphic perception system

The realization of tactile neurons can be achieved by connecting a Mott memristor in series with a piezoresistive sensor or a piezoelectric sensor. The advantage of the piezoresistive sensor lies in its flexibility, while the piezoelectric sensor offers the benefit of self-power supply. For temperature neurons, the temperature characteristics of Mott memristors can be utilized, and a single Mott memristor can be employed for implementation. Alternatively, it can be realized by connecting a Mott memristor in series with a thermistor. The implementation methods for visual neurons are as follows: Connecting a Mott memristor in series with a photoresistor; Using a transistor as a light sensor to drive the Mott memristor to oscillate, typically in the two forms shown in the figure; Utilizing the photosensitive properties of VO_2 Mott memristors to encode light information into electrical pulse signals. Olfactory neurons can be realized by connecting a Mott memristor in series with an olfactory resistive sensor, or by connecting an olfactory transistor sensor in series. Auditory neurons can be achieved by connecting a triboelectric sound sensor in series with an STL transistor.

3.1.1 Tactile sensory neurons

The hand is the most important tactile sensory organ in humans, with approximately 17,000 mechanoreceptors in its hairless skin. The basic task of the mechanoreceptors is to extract information about the spatial details of skin deformations, encode them into biological impulses, and fuse multiple biological impulses, ultimately transmitting the spiking sequence to the spinal cord and medulla. Thus, perception, spike encoding and information fusion are the three basic functions of a mechanoreceptor, allowing the hand to be very agile in processing a wide variety of complex tactile information [34]. In order to realize artificial mechanoreceptors in hardware, researchers have combined pressure sensors and artificial pulsed neurons to study the correspondence between the frequency of emitted pulses and pressure. Fang et al built an artificial mechanoreceptor circuit as shown in **Fig. 17(a)** using a VO_2 motor memristor and three pressure sensors [168]. The circuit not only encodes the pressure information sensed by the pressure sensors into a spiking signal (**Fig. 17(b)**), but also fuses the information from the three pressure sensors into a signal all the way through, thus realizing the functions of perception, spike encoding, and information fusion of artificial mechanoreceptors.

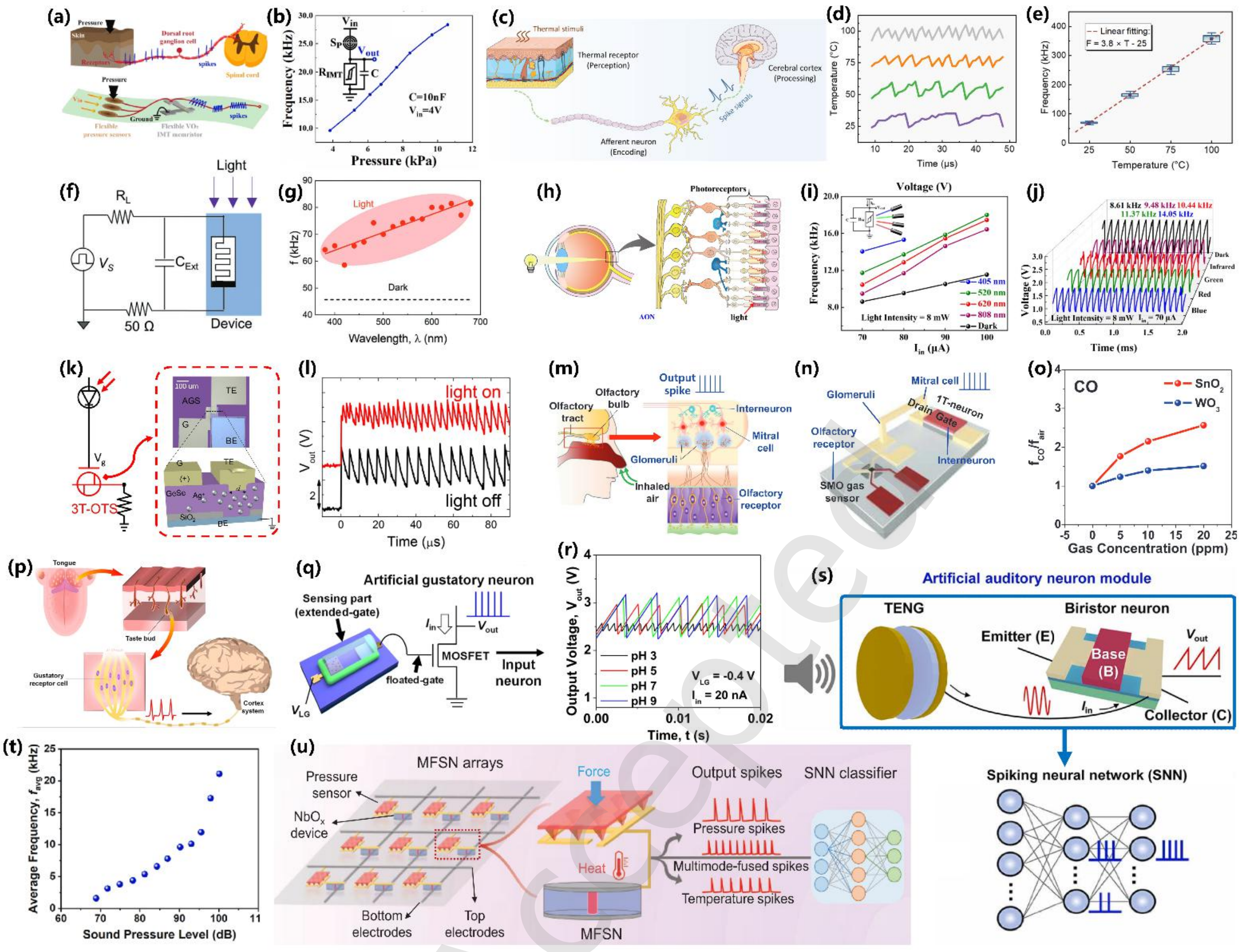

Figure 17 (a) Biological mechanoreceptor and artificial mechanoreceptor. (b) Relationship between the oscillation frequency and pressure. Reproduced with permission from Ref. [168]. © Elsevier B.V. 2022. (c) Schematic diagram of the human sensory nervous system. The whole process is carried out by a combination of thermal receptors, afferent neurons, and the cerebral cortex. (d) The disparate spiking performances (frequency) of afferent neurons at different temperatures. (e) The relationship between the spiking frequency and temperature and corresponding distributions. Reproduced with permission from Ref. [103]. © Royal Society of Chemistry 2024. (f) The circuit configuration of the Pearson–Anson oscillator to analyze the oscillation dynamics. (g) The oscillation frequency in relation to the wavelength. Reproduced with permission from Ref. [169]. © Wiley-VCH GmbH 2024. (h) Schematic illustration of the eye and retina. (i) The correlation between the ASP's output spiking frequency and I_{in} at different wavelengths with a light intensity of 8 mW. (j) The spike trains generated by the ASP when irradiated with light of different wavelengths under an input current of 70 μA and a light intensity of 8 mW. Reproduced with permission from Ref. [170]. © American Chemical Society 2024. (k) Schematic diagram of the artificial RGC via 3T-OTS and Optical microscope image (top) with a schematic illustration of the cross-section (bottom) of the 3T-OTS device. (l) Spike patterns of the RGC neuron with (red) and without (black) light. Reproduced with permission from Ref. [171]. © American Chemical Society 2022. (m) A biological olfactory system comprises various olfactory neurons, including olfactory receptors, glomeruli cells, mitral cells, and interneurons. (n) Schematic diagram of the artificial olfactory neuron module. The SMO gas sensor operates as an olfactory receptor that captures odorants. (o) The electrical characteristics of the artificial olfactory neuron modules for CO gas. Reproduced with permission from Ref. [172]. © Wiley-VCH GmbH 2022. (p) Workflow of the biological gustatory system. (q) The proposed neuromorphic E-tongue system with artificial gustatory neuron. (r) Variation of the waveform of V_{out} with pH concentration for the pH-sensitive artificial gustatory neuron. Reproduced with permission from Ref. [173]. © American Chemical Society 2022. (s) Schematic diagram of the biological auditory system; (t) Relationship between mean spiking frequency of the artificial auditory system and Sound Pressure Level. Reproduced with permission from Ref. [127]. © Elsevier Ltd 2023. (u) Schematic of an artificial neuromorphic sensing system combining sensors and artificial neurons. Reproduced with permission from Ref. [174]. © Wiley-VCH GmbH 2022.

3.1.2 Thermal sensory neurons

The perception and recognition of external thermal stimuli is a fundamental ability of the human sensory nervous system, which is able to perceive and process the information almost simultaneously by employing a unique strategy, with ultra-low power consumption in the femtojoule range [175].

Li et al. [103] developed an energy-efficient artificial sensory nervous system using a compact thermal afferent neuron built on N-doped SiTe OTS. The thermal sensory neuron is capable of sensing temperatures ranging from 25°C to 100°C without any additional sensors, subsequently converting the data into spike signals with varying frequencies. In this system, thermal stimuli are converted into electrical spikes that are sent to the cerebral cortex for processing as shown in **Fig. 17(c)**. The thermal afferent neuron operates with a capacitor and a resistor to create stable electrical oscillation. The oscillation frequency of the afferent neurons varies with temperature due to changes in threshold voltage, establishing a quasi-linear relationship between temperature and oscillation frequency as exhibited in **Fig. 17((d)(e))**. Additionally, the frequency-encoded artificial afferent neuron exhibits a biofrequency adaptation of hundreds of kilohertz, which offers promising potential for bioelectronic interface applications.

To simplify the neuron structure, Han et al presented a flexible artificial spiking warm receptor realized by a single VO_2 Mott memristor driven by a current source mimicking the behavior of biological warm receptors [176]. As the stimulus temperature rises from 20 to 40 °C, the spiking frequency increases, then rapidly drops to zero at 45 °C. This flexible artificial spiking warm receptor shows promise for use in bio-inspired electronic skin for spike-based intelligent machines with neuromorphic computing.

3.1.3 Visual sensory neurons

Autonomous vehicles and drones require advanced electronic systems for visual target detection, but traditional CMOS-based image sensing is nearing its limits. In response, artificial neuromorphic vision systems inspired by the human visual system have gained interest due to their ability to simulate visual processing through spike coding, offering high throughput with low energy consumption [30, 31].

Research has focused on integrating photoreceptors with artificial spiking neurons to convert optical signals into frequency-encoded spikes. For example, Wu et al. [177] developed a neuromorphic artificial photoreceptor using a Ta/IGZO/Pt structure combined with a NbO_x memristor, which responds to ultraviolet light and influences spiking frequency. Pei et al. [178] created a multifunctional artificial vision system using an optoelectronic memristor that converts signals to voltages, activating an actuator to mimic eye muscle contractions in response to bright light.

Photoreceptors and optical nerves together make up the retina. Each optical nerve is connected to a specific range of photoreceptors, forming the photoreceptor's receptive field as shown in **Fig. 17(h)**. Exploring the photoconductive and bolometric properties of VO_x, artificial spiking photoreceptor (ASP) can be realized by using a single VO_x Mott memristor. For example, Nath et al. [169] demonstrated the direct optical control of an oscillatory neuron utilizing volatile threshold switching in V_3O_5. The devices operate without the need for electroforming, and their switching parameters can be adjusted through optical illumination. A Pearson-Anson oscillator based on this device was further constructed as shown in **Fig. 17(f)**, confirming that light irradiation can govern its oscillatory dynamics. The oscillation frequency can be dictated by the light wavelength and incident light intensity, as illustrated in **Fig. 17(g)**. Han et al. [170] presented a bioinspired flexible artificial spiking photoreceptor (ASP), which is realized by using a single VO_2 Mott memristor with ITO transparent top electrode that can simultaneously sense and encode the stimulus light into spikes. The ASP has high spike-encoded photosensitivity and ultrawide photosensing range (405–808 nm) with good endurance (>7 × 10^7) and high flexibility (bending radius ~5 mm). Under the same light intensity, the output spike frequencies at different wavelengths all increase with the growth of the input current (I_{in}) and diverge from each other presents a comparison of the output spike trains of light at different wavelengths, as shown in **Fig. 17((i)(j))**.

Moreover, the photoelectric spiking neuron (PSN) with an Ag/TaO_x/ITO memristor by Chen et al. exhibits precise light-spike transformation and depth perception capabilities, enhancing pattern recognition accuracy from 68% to 90% in an artificial binocular visual system [90]. Lee et al. [171] later developed a three-terminal OTS spiking neuron using Ag-doped GeSe2, combined with a photodiode to form an artificial retinal ganglion cell (RGC), successfully encoding visual signals into inter-spike interval information. The schematic illustration of the artificial visual neuron circuit based on the 3T-OTS device is shown in **Fig. 17(k)**. The output waveforms in **Fig. 17(l)** under the conditions of the light source being on and off clearly revealed that the spike frequency is higher than that in the dark when the artificial RGC is illuminated.

3.1.4 Olfactory sensory neurons

Olfaction is the process by which organisms sense odors through their noses, converting odor information into bioelectrical impulse signals that are sent to the cerebral cortex for processing [179]. J.K. Han et al. [172] developed a hardware implementation of an olfactory receptor by connecting a gas sensor to a single transistor artificial spiking neuron on the same substrate. The system includes a semiconductor metal oxide (SMO) gas sensor and a MOSFET-based 1T-neuron, with metal interconnections acting as a glomerulus to transmit signals from olfactory receptors as demonstrated in **Fig. 17((m)(n))**. The spiking frequency of the artificial olfactory neuron modules correlates with gas concentrations, increasing for NH_3, CO, and acetone, while decreasing for NO_2. **Fig. 17(o)** especially shows the correlation between the spiking frequency of the olfactory sensors and the concentrations of CO in the ambient environment when SnO_2 or WO_2 was respectively applied as the gas-sensitive film connected to the 1T-neuron. This scalable neuromorphic electronic nose (E-nose) offers a new approach for energy-efficient mobile gas sensing.

3.1.5 Gustatory sensory neurons

Taste perception in humans involves responses from gustatory receptor neurons located in taste buds as exhibited in **Fig.17(p)** [180]. To replicate this in hardware, J.K. Han et al. [173] developed a highly scalable and energy-efficient electronic tongue (E-tongue) by connecting pH or Na+ sensors to a single transistor MOSFET in an extended-gate structure, as shown in **Fig.17(q)**. This setup allows the sensors to communicate taste information to the MOSFET's gate, influencing the spiking frequency of artificial spiking neurons and converting taste data into spike coding signals for classification by a SNN. The E-tongue's performance is illustrated by how changes in pH affect the spiking characteristics of pH-sensitive artificial gustatory neurons, with lower pH leading to increased spiking frequency as demonstrated in **Fig. 17(r)**. Similarly, higher Na+ concentrations also result in a rise in spiking frequency. Furthermore, by changing the sensing layer, the E-tongue can detect other tastes, such as sweetness and bitterness.

3.1.6 Auditory sensory neurons

Hearing is achieved through the collaboration of the ear, auditory nerve, and auditory center. The ear consists of the outer, middle, and inner ear, where the outer and middle ear transmit sound, and the inner ear senses it. Sound waves vibrate the tympanic membrane, which is transmitted to the basilar membrane, causing hair cells to generate nerve impulses that are converted into bioelectrical spiking signals for processing in the cerebral cortex.

Yun et al. [127] developed an auditory receptor by connecting a friction electric nanogenerator with a single transistor artificial spiking neuron(**Fig. 17(s)**). This nanogenerator serves as both a sound sensor and a power source, enabling low power consumption. The relationship between the auditory receptor's output voltage spiking frequency and sound intensity is demonstrated, showing that the spiking frequency increases with sound intensity (**Fig. 17(t)**), mimicking biological auditory system characteristics.

3.1.7 Multisensory neurons

The human body is a highly sensitive multi-sensory fusion system that converts external environmental signals into spikes through the binding of receptors to neurons, thus enabling accurate judgment of variable and complex situations in the environment. For example, we are able to accurately recognize whether there is water in the cup in our hands and whether the water is hot or cold. The combination of artificial neurons constructed using Mott's amnesia blocker and multiple sensors can be easily implemented in hardware to simulate multiple human senses.

Yuan et al [181] presented a leaky integrate-and-fire (LIF) artificial spiking sensory neuron (ASSN) using a NbO_x memristor and an a-IGZO thin-film transistor (TFT) for edge processing of perception information. The a-IGZO TFT exhibits dual sensitivity to NO_2 gas and ultraviolet (UV) light, so the ASSN can encode NO_2 gas concentration and UV intensity into spikes. Consequently, the ASSN demonstrates an inhibitory response to NO_2 stimulation while exhibiting an excitatory response to UV light stimulation. Therefore, self-adaption and lateral regulation circuits between different ASSNs are proposed at the edge in mimicking biological neurons' rich interconnection and feedback mechanisms.

Zhu et al [174] reported a multimode-fused spiking neuron (MFSN) designed for human-like multisensory perception, integrating a pressure sensor and a NbO_x-based memristor for temperature sensing (**Fig. 17(u)**). The MFSN fuses multisensory analog information into a single spike train, demonstrating effective data compression and conversion. It distinguishes pressure and temperature information by decoupling output frequencies and amplitudes, thereby supporting multimodal tactile perception.

Advancements in artificial spiking sensory neurons, such as the ASSN and MFSN, demonstrate significant potential for simulating human-like multisensory perception. By integrating various sensors and utilizing innovative materials like NbO_x memristors and a-IGZO TFTs, these systems can effectively process and encode environmental signals. The development of self-adaptive circuits further enhances their functionality, paving the way for more sophisticated, intelligent sensory systems in robotics and other applications.

3.2 Neuromorphic computing system

The traditional computing model relies on the Von Neumann architecture, which separates storage and computation. This separation requires frequent data transfers between the computing and storage units, resulting in significant inefficiencies and high energy consumption. To address these issues, neuromorphic computing architecture [3, 182] has been developed to emulate the brain's efficiency. Neuromorphic systems process information using artificial neurons and synapses, integrating memory and computation. This approach allows for the creation of low-power, high-efficiency computing systems. This section will explore the construction of a neuromorphic computing system utilizing artificial spiking neurons to execute tasks based on Various neural networks and in-sensor computing

3.2.1 SNN

As a third-generation artificial neuron model, spiking neural networks (SNNs) efficiently simulate the functioning of the human brain. SNNs incorporate neurons with synaptic states, transmitting information through discrete spikes represented by their timing and rate of arrival. The most commonly used models for SNN neurons are the LIF model and the IF model [138]. SNNs offer higher computational efficiency and lower energy consumption compared to first- and second-generation artificial neuron models, leading to an increased demand for SNN-related hardware in recent years. Unlike CMOS-based neuromorphic circuits, this hardware is believed to achieve similar functionality with lower power consumption and a smaller device footprint.

Zhang et al. [183] experimentally demonstrated a one-layer SNN (320 × 10) based on the 1T1R Mott neuron, which incorporates RRAM synaptic weight elements and Mott-type output neurons. Thanks to the rectified linear voltage-rate relationship of the 1T1R neuron and its inherent stochasticity, the system achieved a 95.7% conversion accuracy and an 85.7% recognition accuracy on the MNIST dataset.

To develop SNN hardware circuits using artificial spiking neurons, Lee et al. [150] first modeled the operation of an artificial neuron based on a Single-Device Leaky-FeFET (SD L-FeFET), with fitted and experimental data. They then designed a three-neuron layer SNN comprising 32 × 32 input neurons, 40 intermediate neurons, and 3 output neurons. Neurons in each layer integrate postsynaptic currents and operate according to the LIF model. The data is clustered using unsupervised learning and classified through supervised learning. This SNN achieved a 92.5% recognition rate for the MNIST dataset and a 91.7% recognition accuracy for face recognition samples from the Yale face database.

3.2.2 RSNN/LSNN

Recurrent spiking neural networks (RSNNs) are studied for their potential to model brain networks, particularly for temporal computations like speech processing, using spikes as events in time and space. However, typical RSNN models lack many dynamic processes present in biological neurons [184]. Long short-term memory spiking neural networks (LSNNs) can be regarded as a structured subclass of RSNNs that augment recurrent spiking circuits with additional slow state variables (e.g., adaptive thresholds or spike-frequency adaptation), thereby introducing multiple intrinsic time constants and substantially improving long-range temporal memory while preserving event-driven computation. Rui Y. et al. [74] developed an efficient physiological signal processing system using a VO_2 memristor-based asynchronous spike encoder and a decision-making LSNN as illustrated in **Fig. 18(a)**. This system converts analog physiological signals, such as ECG, into spike trains and processes them through a three-layer architecture, consisting of an input layer, a hidden recurrent layer with LIF and ALIF neurons, and an output classification layer referred to **Fig. 18(b)**. The LSNN's adaptive ALIF neurons enhance its temporal processing capabilities. The system's effectiveness was validated by classifying heartbeats from the MIT-BIH arrhythmia database, achieving a 95.83% accuracy after 150 training epochs as shown in **Fig. 18(c)**. The confusion matrix indicated successful classification of heartbeats across four distinct classes.

3.2.3 ONN

Oscillatory neural network (ONN) is an emerging neural network architecture that simulates the information represented by the phase relationship between oscillating signals generated by neurons in the human brain, as shown in **Fig. 18(d)**. Since ONN focuses on utilizing the phase rather than the amplitude of the signals, it has great potential to reduce the energy consumption of the hardware. The hardware implementation of ONN requires artificial oscillators that generate oscillatory signals continuously, coupled by two or more artificial oscillators, where the oscillatory signals generated independently by each oscillator can interact with each other, and thus encode the information using the phase difference.

Yun et al. [128] developed a birillator using a bistable resistor, then constructed an ONN network with four capacitively coupled birillators to solve the vertex coloring problem. The output waveforms and phase differences are illustrated, indicating that when the phase difference exceeds 60°, the vertices display different colors.

Coupling multiple oscillating neurons that generate continuous voltage oscillations in a completely parallel manner can establish an ONN system based on spontaneous synchronization of multiple oscillations [185]. For example, a 3×5 ONN system created from 15 $Nb/SiO_x/Nb$ TS oscillating neurons successfully identifies noise input patterns based on the synchrony of their output oscillations [128] .

3.2.4 PCNN

Pulse coupled neural networks organize neuronal population activity through iterative firing governed by local neighborhood coupling and dynamic threshold updating. Johnson systematized this model in 1994 as an image processing framework in which neurons are often mapped one to one to pixels [186]. Compared with spiking neural networks, which typically rely on trainable synaptic weights for general inference tasks, PCNNs place greater emphasis on neighborhood coupled synchronization and dynamic threshold driven spiking dynamics, and are therefore commonly used for structured vision operations such as image segmentation and image fusion.

Wu et al. [177] reported a simplified single layer PCNN driven by spike encoded inputs from artificial optic sensory neurons. The sensory neuron was formed by connecting a $Ta\backslash IGZO_4\backslash Pt$ ultraviolet sensor in series with a $Pt\backslash NbO_x\backslash Ta$ oscillatory neuron, and the resulting spike encoded signals were used as the PCNN input. The PCNN employs two-dimensional local connectivity, with neurons mapped one to one to image pixels and coupled to neighboring neurons, enabling ultraviolet image segmentation in complex backgrounds without training, as shown in **Fig. 18(e)**.

Meanwhile, conventional multispectral image fusion typically relies on post-imaging digital preprocessing, which incurs substantial data-movement overhead. To mitigate this overhead and to establish a representation and processing paradigm closer to biological vision, Zhang et al. [187] developed a PCNN for near-infrared and ultraviolet image fusion, using spike-encoded images generated by artificial visual neurons as direct inputs. The PCNN maintained stable and robust fusion performance across 30 image pairs and under noise and optical distortion perturbations. Besides, featuring broad spiking frequency range (0.3–2.65 MHz) and low spiking energy (0.57 nJ), this system achieves enhanced processing speed and efficiency at lower power consumption.

3.2.5 Multi-NN

Computational methods using artificial neural networks (ANNs), such as convolutional neural networks (CNNs) and reservoir neural networks (RNNs), encode image information in an analog form, which benefits image processing and recognition. In contrast, SNNs mimic biological structures like the retina and cortex, encoding image data as spikes and offering rich spatio-temporal dynamics that integrate perception, storage, and processing.

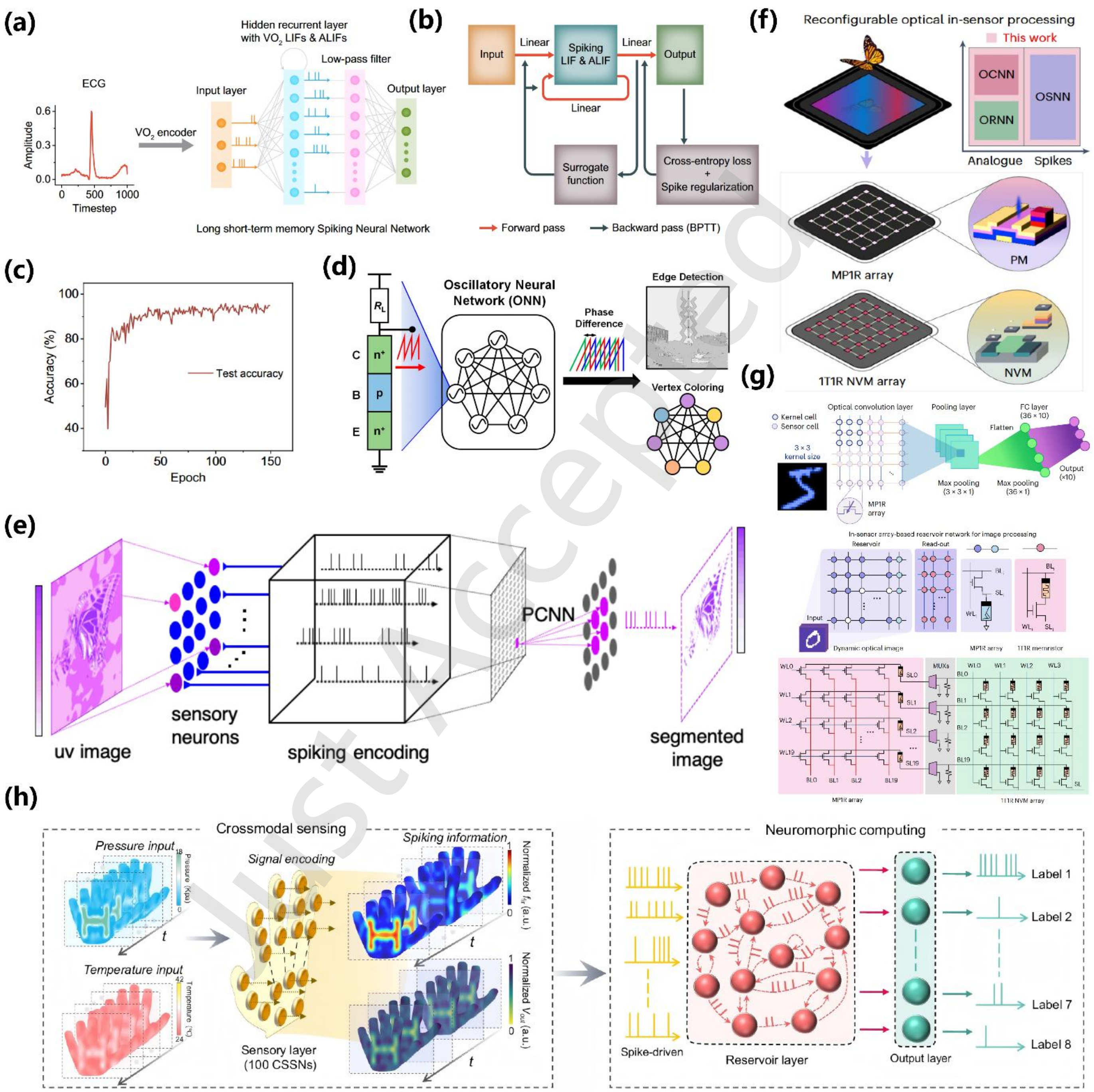

Figure 18 Computing system. (a) Detailed schematic of the VO_2 memristor-based physiological processing system. (b) Complete workflow of the LSNN operation. (c) Schematic diagram of the SNN structure. Reproduced with permission from Ref. [74]. © Springer Nature 2023. (d) ONN structure schematic. Reproduced with permission from Ref. [128]. © American Chemical Society 2024. (e) PCNN structure schematic. Reproduced with permission from Ref. [177]. © American Chemical Society 2020. (f) This artificial intelligence vision system adopts memristors and the MP1R array. PM stands for photonic memristor. (g) Detailed schematics of the MP1R array-based OCNN, ORNN and OSNN. Reproduced with permission from Ref. [188]. © Springer Nature 2024. (h) CSSN structure schematic. Reproduced with permission from Ref. [189]. © Springer Nature 2024.

To create a universal vision computing system, an in-sensor computing architecture that supports both analog and spiking methods is essential. Dang et al. [188] developed a 20×20 array of indium gallium zinc oxide (IGZO) phototransistors and a single Mott memristor (MP1R) using a reconfigurable heterostructure. The MP1R exhibits self-rectifying volatile and threshold switching behaviors, making it compatible with both architectures and capable of integrating optical sensing and signal processing. This MP1R array works alongside a 1T1R non-volatile memory (NVM) array, which functions as a classifier using analog resistive switching. Together, they are integrated onto a single printed circuit board to form an in-sensor vision computing system. The system supports various multimodal optical neural network architectures, including optical convolutional neural networks (OCNNs), optical recurrent neural networks (ORNNs), and optical spiking neural networks (OSNNs) as shown in **Fig. 18(f). Figure 18(g)** delineates the fundamental structures and comprehensive schematic illustrations of the three optical neural networks as the OCNN, ORNN and OSNN.

3.2.6 In-sensor computing

The IoT and AI-driven explosion of unstructured data exacerbates the 'memory wall' and power bottlenecks in von Neumann architectures, necessitating the emergence of in-sensor computing [190, 191]. By embedding computation directly within sensors, this architecture transforms passive collectors into active processing nodes. This minimizes redundant data movement, drastically reducing latency and energy consumption while enhancing integration density for applications like edge intelligence and autonomous driving. Regarding visual perception, Li et al. [192] (2024) proposed a single-transistor optoelectronic spiking neuron (TS-FET) featuring an ultra-compact design by integrating a gate-modulated 2D MoS2 channel with a volatile threshold switch. Utilizing a resistance-matching mechanism, this device bio-faithfully emulated the excitatory and inhibitory characteristics of retinal neurons under illuminated and dark conditions, realizing optogenetics-inspired spike modulation. In the same year, the same research team constructed a reconfigurable neuromorphic unit [193] based on an all-2D material heterostructure (MoS_2/hBN/Gr). This device not only emulates synaptic and integrate-and-fire neuronal functions but also realizes dendritic computing capabilities—specifically nonlinear filtering and Boolean logic operations—through optoelectronic modulation, thereby significantly enriching the diversity of neural information processing. In the domain of olfactory sensing, Lee et al. [194]developed a "two-in-one" artificial olfactory neuron utilizing a silicon nanowire field-effect transistor (Si-NW FET) decorated with catalytic metal nanoparticles (Pd/Pt) in 2023. This device directly encodes gas concentration information of H_2 and NH_3 into spike frequency signals without requiring external analog-to-digital converters, validating gas classification capabilities based on spiking neural networks (SNNs).

While single devices have exhibited excellent sensing and encoding characteristics, constructing system-level arrays capable of multimodal fusion and real-time feedback remains a critical step toward practical application. Li et al. [189] (2024) utilized high-performance flexible VO_2 memristors fabricated via a low-temperature process to construct a crossmodal spiking sensory neuron (CSSN) and its array system. By introducing a Cr_2O_3 buffer layer, the team significantly optimized the crystalline quality of the VO2 thin film, achieving volatile threshold switching devices with ultra-high endurance (>10^{12} cycles), low variability (device-to-device variability of only 3.73%), and excellent flexibility (bending radius of 1 mm). The CSSN unit based on this device leverages a piezoresistive sensor and the intrinsic thermistor properties of VO_2 to synchronously perceive pressure and temperature signals, encoding them into spike trains with distinct frequencies and amplitudes. Furthermore, the study established a hardware system based on Spiking Reservoir Computing, successfully achieving crossmodal recognition of dynamic objects with an accuracy of up to 98.1%, as well as real-time haptic feedback for human-machine interaction, as shown in **Fig. 18(h)**. This work demonstrates the immense potential of memristor arrays in constructing energy-efficient, low-latency wearable human-machine interfaces, providing a robust reference for the integrated development of future in-sensor computing systems.

4 Future Perceptive

Recent literature has demonstrated that current neuromorphic devices and systems offer significant advantages across various application scenarios, providing valuable insights for new development prospects and methodologies that warrant further exploration. Based on this context, we present the following perspectives.

(1) Material level: **Introduction of new materials in Transistor-Based Artificial Spiking Neurons.** Most transistor-based artificial spiking neurons rely on inorganic materials, whereas organic transistors are emerging as a complementary platform because they are low-cost, mechanically compliant, and compatible with solution processing and low-temperature fabrication. These features enable monolithic integration with soft sensors, wearables, and large-area arrays. Organic electrochemical transistor (OECT)-based neurons have already been demonstrated. For embodied intelligence, co-integration of organic neuromorphic devices with artificial skins, tactile sensors, and soft actuators could support low-latency, low-power sensing–learning–control loops under deformation and humidity. However, stability and endurance under oxygen, moisture, temperature variation, and biofluids remain key bottlenecks, motivating advances in robust materials, interface engineering, and encapsulation. In addition, beyond organics, 2D materials also have substantial potential for neuromorphic computing. They are readily compatible with van der Waals stacking and heterogeneous integration, enabling the incorporation of diverse physical mechanisms, for example charge trapping/detrapping, ionic migration, polarization modulation, and phase-transition-assisted switching. These coupled effects hold substantial

promise for the joint modulation of the time constant, firing threshold and response gain of artificial neurons.

(2) Device level: **Enhancing Performance.** A high spiking rate directly increases the number of events that can be encoded per unit time, thereby supporting lower end-to-end latency, higher event throughput and faster system convergence, which is particularly valuable for time-critical workloads such as event-driven sensing and edge neuromorphic inference. For transistor-based neurons, the attainable rate is often bounded by RC parasitic, carrier-lifetime or trap-mediated dynamics, ferroelectric switching kinetics, and the energy overhead associated with reset and readout. For memristor-based neurons based on volatile TS devices such as OTS or Mott memristors, can intrinsically sustain rapid spiking, yet high-rate cycling exacerbates threshold drift, cycle-to-cycle jitter and endurance limitations. By contrast, Ion diffusion devices provide versatile time constants, but faster operation often comes at the expense of higher variability and switching energy, motivating shorter ionic pathways, better filament confinement and improved control of the volatile window. Overall, device optimization should prioritize energy per spike, temporal fidelity, endurance and uniformity, rather than frequency alone.

(3) Circuit and neuron level: **Innovative Circuit Designs.** Currently, most memristor-based artificial spiking neuron circuits are constructed by combining resistor and capacitor devices. There is limited research on simulating neurons by integrating transistor and inductor devices. Therefore, developing artificial spiking neurons with multiple neural states through various device combinations, including inductors, represents a promising avenue for further study. Moreover, prevalent neuron models for neural component simulation include the integral-fire (IF) model and the leaky integral-fire (LIF) model. However, fewer devices have been designed based on more complex neuron dynamics, such as the four-dimensional Hodgkin-Huxley (HH) equations, the three-dimensional Hindmarsh-Rose (HR) equations, and the two-dimensional FitzHugh-Nagumo (FHN) equations. Recently, research teams have begun constructing circuit and dynamic models of artificial neurons based on FHN and HR neurons. Thus, the design and development of devices and circuit models that accurately simulate complex neural morphologies could be a significant direction for future research, particularly for mimicking human brain neurons.

(4) System and application level:

Toward scalable neuromorphic systems. Scaling artificial synapses and neurons from single devices to arrays is primarily limited by interconnect scalability and device uniformity. In integrated crossbars, sneak-path currents, line parasitics and IR-drop shrink the read and write margin and cap the practical array size. Peripheral circuits such as selectors, comparators, data conversion and event routing can further erode density and energy-efficiency benefits. Moreover, variability, threshold drift and temperature sensitivity lead to frequency dispersion and phase noise, requiring online calibration and tolerance. High-rate operation also raises concerns in endurance, thermal management, and compatibility with CMOS processes and packaging.

Addressing Data Processing Needs. To effectively manage the rapid development of the Internet of Things (IoT) across various industries, neuromorphic computing technologies—such as spiking neural networks (SNNs) and oscillatory neural networks (ONNs)—are gaining increasing attention. ONNs, particularly those with coupled oscillators, are notable for processing computations based on oscillator phases rather than signal amplitudes, which can significantly enhance energy efficiency. OTS devices, as promising artificial afferent neurons, have shown great potential in boosting the computational speed of SNNs and ONNs through high-frequency oscillations and fast switching speeds.

Toward deployable edge neuromorphic intelligence. Deploying neuromorphic systems in edge and Internet of Things nodes, wearables, and biointerfaces requires low power, low latency, and long-term reliability. Humidity, oxygen, temperature swings, bending, and biofluids can accelerate drift and ageing, degrading thresholds, time constants, and inference stability, which calls for adaptive compensation and adequate margins. Meanwhile, task-to-hardware mapping methods and unified benchmarks that jointly assess accuracy, energy, latency, and robustness remain limited. Manufacturing yield, reconfigurability, data privacy, and verifiable security further hinder large-scale deployment.

5 Conclusion

To address the limitations of conventional von Neumann computing, artificial spiking neurons built on emerging electronic devices provide a promising route toward configurable and energy-efficient neuromorphic hardware that tightly couples sensing and computation. In this review, we adopt a material–device–circuit–system perspective and systematically summarize artificial spiking neurons spanning memristor-based and transistor-based implementations, together with their spiking mechanisms, circuit construction templates, and representative applications in neuromorphic perception and brain-inspired computing architectures. To enable fair cross-technology comparison, we further introduce a unified benchmarking framework centered on key performance indicators, which covers electrical metrics, reliability and integration constraints, and functional attributes (including test-condition dependence), and we compile representative data in **Table 1** for ion diffusion-, OTS-, PCM-, Mott memristor-, and transistor-based neurons.

From the device perspective, each technology exhibits a distinct performance envelope. Mott-memristor neurons already demonstrate low to moderate threshold voltages (e.g. 0.4–1.3 V) with endurance extending beyond 10^7 cycles and, in selected stacks, reaching above 10^{12} cycles, together with firing frequencies from tens of kHz up to hundreds of kHz and energy per spike down to the sub-pJ regime, and even fJ-level values in simulation, which positions Mott devices as strong candidates for compact, high-rate spiking primitives when process integration is feasible. OTS neurons emphasize fast threshold switching and BEOL-friendly integration routes in representative cases, including kHz-to-MHz class operation with energy per spike around sub-nJ to nJ, and vertically stackable $Ge_{0.6}Se_{0.4}$ implementations with thermal budget below 400 °C, supporting dense 3D integration and high-speed oscillatory dynamics relevant to coupled-oscillator computing. Ion diffusion neurons offer low threshold operation (e.g., 0.52 V) and substantial endurance (>10^8 cycles in a representative device), while their demonstrated firing rates and energy figures span from tens of kHz to higher-rate pulse-driven demonstrations with pJ to nJ-level energy per spike, indicating a useful regime for rich time-constant engineering under carefully controlled operating windows. PCM-based neurons highlight non-volatile state physics and very high endurance (e.g., 1×10^{12} cycles) with pJ-level spiking energy, but they typically rely on explicit RESET and crystallization pulse trains, which shifts part of the design burden to peripheral timing and reset management. Transistor neurons retain the advantage of mature CMOS integration and circuit design flexibility. Transistor-based artificial neurons are attractive primarily because they are directly compatible with mature CMOS process flows and circuit design methodologies, which simplifies monolithic integration with peripheral circuitry and system-level co-design. In addition, their multi-terminal gate control enables flexible programmability of neuronal dynamics (e.g., tuning thresholding, excitatory/inhibitory inputs, and firing-rate characteristics) without relying on delicate volatile operating windows. Consistent with Table 1, transistor neurons span a broad operating envelope, with representative thresholds of ~0.6–6.3 V and firing rates of ~0.35–245 kHz, while achieving competitive energy efficiency that can range from tens of femtojoules per spike (e.g., 37 fJ in an AFeFET neuron) up to the pJ regime depending on the device and circuit topology. Reliability can also be strong in optimized ferroelectric variants, where endurance exceeding 10^{12} cycles is reported, although stability issues such as threshold drift (e.g., in latch-type devices) and phase-distribution effects (e.g., in Hf-based FeFETs) still need to be addressed for scalable, robust deployment. For single-transistor latch (STL) devices, it is the significantly induced threshold voltage drift after repeated operations leading to poor stability. For Hf-based FeFETs, the coexistence of dielectric and ferroelectric phases means the ratio and distribution of the ferroelectric phase can influence device characteristics by inducing an inhomogeneous electric field in scaled devices.

Meanwhile, in practical spiking neurons, spike intervals are not perfectly uniform even under identical stimuli, because device stochasticity and circuit noise introduce cycle-to-cycle timing fluctuations. This temporal jitter degrades timing margins, synchronization robustness, and latency predictability at the circuit and system levels. To enable cross-technology comparison, we quantify jitter using the inter-spike interval (ISI) and its coefficient of variation, $\mathrm{CoV_{ISI}} = \sigma_T/\mu_T$, where μ_T and σ_T are the mean and standard deviation of the ISI distribution. Different mechanisms show a clear hierarchy in $\mathrm{CoV_{ISI}}$, which captures the relative dispersion of spike-timing jitter. Ion-diffusion neurons typically exhibit the largest values (~10%–60%), because stochastic ion transport and redox-driven filament dynamics, together with environmental sensitivity and circuit parasitic, amplify cycle-to-cycle variability. Mott (~5%–15%), phase-change devices (~8%–20%), and OTS-based neurons (<25%) fall in an intermediate regime, reflecting nucleation- and threshold-switching fluctuations, although strong nonlinearity can stabilize firing within an appropriate bias window. In contrast, ferroelectric (~1%–4%) and anti-ferroelectric neurons (<4%) generally show lower jitter, consistent with more deterministic polarization switching; residual variations are mainly linked to domain statistics, defects, non-uniformity, and peripheral noise.

In summary, this work provides a comprehensive overview of the latest advancements, benchmarks, and future prospects of artificial spiking neurons based on emerging electronic devices, aimed at addressing the inefficiencies of traditional von Neumann computing architectures and advancing neuromorphic perception and computation. By systematically categorizing and analyzing these artificial spiking neurons as memristor-based and transistor-based devices, this study clarifies their working mechanisms, performance characteristics, and application potential—offering a valuable reference for interdisciplinary research at the intersection of materials science, microelectronics, and neuroscience.

Data availability

Not applicable.

Acknowledgement

This work was supported by the National Natural Science Foundation of China (No. 62574161, 62174130).

Declaration of competing interest

All the contributing authors report no conflict of interests in this work.

Author contribution statement

Zheng Fang and Kaiyao Wang contributed equally to Data curation, project administration, validation, writing manuscript. Shujing Zhao, Shiquan Fan, Weihua Liu, Xin Li, Li

Geng: Data curation. Chuanyu Han: Project administration, funding acquisition, writing manuscript. All the authors have approved the final manuscript.

Use of AI statement

During the preparation of this work, ChatGPT is used in order to refine "A schematic illustration. After using this tool/service, the authors reviewed and edited the content as needed and take full responsibility for the content of the publication.

Table 1 Performance indicators of Artificial Spiking Neurons

Device Type	Device Structure	V_{th} /V	Endurance /cycles	Frequency /kHz	Energy per Spike	Volatility¹	Test Conditions	Thermal Budget/°C	CBEC²	Neuron Type	Ref.
Mott Memristor	$Pt/Ti/VO_2/Pt/Ti$	0.4-1.3	$>2.6\times10^7$	~50	5.6fJ(sim)	Yes	DC current source; R & C	-	Yes	HH	[53]
Mott Memristor	$Ti/Pt/NbO_y/NbO_x/Ti/Pt$	~1.5	>1×109	1×10^3(3V)	-	Yes	DC/Pulse driven; Rs=10kΩ; Cp=470pF	-	Yes	LIF	[85]
	$V/VO_x/HfWO_x/Pt$	~1	$>1\times10^{12}$	250(2V)	-	Both	V_{in} pulses; R_s=20kΩ, C_p~200pF	25	Yes	LIF	[48]
	$Au/Ti/VO_2/Al_2O_3$	3.4	6.5×10^6	450(1.3V)	0.34pJ	Yes	DC/Pulse driven; R_L=18kΩ, R_0=50Ω	530	FEOL	LIF/ALIF	[74]
Ion diffusion	$Pt/Ag/HfO_2/Pt$	~0.52	$>1\times10^8$	54 (0.8V)	1.8μW	Yes	DC/Pulse driven; R_L=81kΩ	500	FEOL	LIF	[132]
	W/Mg/MgO/W	~0.65	1×10^5	0.045(1.2V)	4nJ	Yes	Pulse driven; 4 V, 100 Hz	≤50	Yes	LIF	[130]
	$Ag/TaO_x/ITO$	~0.3	>1×103	0.2 (5V)	0.23-0.5μW	Yes	DC/Pulse driven; Rs=1MΩ; Cp=2nF	-	Yes	LIF	[129]
	$Nb/SiO_x/Nb$	~1.2	$>5\times10^4$	562 (3V)	2.4nJ	Yes	V_{in} Pulse driven	-	Yes	LIF	[133]
(with 2D material)	MoS_2 channel and $Ag/Al_2O_3/Au$	~0.3	>500	0.3 (1.4V)	20nJ	Yes	V_{in} Pulse driven	≥105	FEOL	LIF	[150]
OTS memristor	$Mo/Ge_{60}Se_{40}/Mo$	~6.2	-	1×10^3 (6.2V)	~1nJ	Yes	V_{in}=7V; R_1=10kΩ, C=10pF, R_2=100Ω	-	Yes	IF	[151]
	Vertically stackable $Ge_{0.6}Se_{0.4}$	2.5	$>3\times10^4$	90 (50kΩ,4.2V)	358 pJ@60 kHz	Yes	V_{in}=4.2V; R_1=75kΩ, R_2=150kΩ	< 400	Yes	LIF/Coupled oscillator	[52]
	W/N-doped $SiTe/SiO_2/W$	1.12	1×10^7	350 (75°C)	< 0.3nJ	Yes	V_{in} Pulse driven; R_s=50kΩ	-	Yes	LIF	[90]
PCM	Typical PCM modal	Conductance threshold=2μS	1×10^{12}	20 (150ns pulse width)	5pJ	No	Pulse-driven (RESET + crystallizing pulse train)	-	Yes	LIF	[95]
STL Transistor	1 PD-SOI MOSFET	~3.5	-	0.8(10nA)	<45pJ	Yes	DC I_{in}=10nA; V_{GS}=−1V; L_G=880nm	~1000	FEOL	LIF	[89]
	2 SiGe-HBT	~0.6	-	245	≤1.37pJ	Yes	Pulse I_{syn}=10μA; R_s=20kΩ, C_p=4.7pF	>900	FEOL	IF	[165]
	1 OB-MOSFET	5.56	-	0.35(80μA)	<35.5μW	Yes	DC I_{in}=20~80μA; C_p=220nF	>1000	FEOL	Oscillating	[104]
Multiple-gate	1 SOI FINFET	~6.3	-	0.5(60nA)	950pJ	Yes	DC I_{in}=20~60nA; Dual Gate Bias	>1000	FEOL	LIF	[102]
FeFET	1 SD L-FeFET	~3	1×10^4	-	-	Yes	V_{in} Pulse driven	>600	FEOL	LIF	[103]
AFeFET	1 AFeFET	~1.3	$>1\times10^{12}$	-	37fJ	Yes	V_{in} Pulse driven	500	FEOL	LIF	[110]

1. In the Volatility column, 'both' means it has both volatile and non-volatile characteristics, while 'No' means non-volatile.
2. CBEC is an abbreviation for CMOS-back-end compatibility, and FEOL in the table represents CMOS-front-end compatibility.

References

[1] Wang, S.;Song, L.;Chen, W.;Wang, G.;Hao, E.;Li, C.;Hu, Y.;Pan, Y.;Nathan, A.;Hu, G.; Gao, S. Memristor‐Based Intelligent Human‐Like Neural Computing. *Advanced Electronic Materials* **2023**, *9*, 2200877.

[2] Zhou, G.;Wang, Z.;Sun, B.;Zhou, F.;Sun, L.;Zhao, H.;Hu, X.;Peng, X.;Yan, J.;Wang, H.;Wang, W.;Li, J.;Yan, B.;Kuang, D.;Wang, Y.;Wang, L.; Duan, S. Volatile and Nonvolatile Memristive Devices for Neuromorphic Computing. *Advanced Electronic Materials* **2022**, *8*, 2101127.

[3] Kumar, S.;Wang, X.;Strachan, J. P.;Yang, Y.; Lu, W. D. Dynamical memristors for higher-complexity neuromorphic computing. *Nature Reviews Materials* **2022**, *7*, 575-591.

[4] Lecun, Y.;Bengio, Y.; Hinton, G. Deep learning. *Nature* **2015**, *521*, 436-444.

[5] Zuo, W.;Zhu, Q.;Fu, Y.;Zhang, Y.;Wan, T.;Li, Y.;Xu, M.; Miao, X. Volatile threshold switching memristor: An emerging enabler in the AIoT era. *Journal of Semiconductors* **2023**, *44*, 053102.

[6] Han, J.-K.;Yun, S.-Y.;Lee, S.-W.;Yu, J.-M.; Choi, Y.-K. A Review of Artificial Spiking Neuron Devices for Neural Processing and Sensing. *Adv. Funct. Mater.* **2022**.

[7] Han, J. K.;Yun, S. Y.;Lee, S. W.;Yu, J. M.; Choi, Y. K. A Review of Artificial Spiking Neuron Devices for Neural Processing and Sensing. *Advanced Functional Materials* **2022**, *32*, 2204102.

[8] Yoo, H.-J. 1.2 Intelligence on Silicon: From Deep-Neural-Network Accelerators to Brain Mimicking AI-SoCs. IEEE.

[9] Zidan, M. A.;Strachan, J. P.; Lu, W. D. The future of electronics based on memristive systems. *Nature Electronics* **2018**, *1*, 22-29.

[10] Roy, K.;Jaiswal, A.; Panda, P. Towards spike-based machine intelligence with neuromorphic computing. *Nature* **2019**, *575*, 607-617.

[11] Han, S.;Liu, X.;Mao, H.;Pu, J.;Pedram, A.;Horowitz, M. A.; Dally, W. J. EIE：Efficient Inference Engine on Compressed Deep Neural Network. *ACM SIGARCH Computer Architecture News* **2016**, *44*, 243-254.

[12] Zhang, T.;Yang, K.;Xu, X.;Cai, Y.;Yang, Y.; Huang, R. Memristive Devices and Networks for Brain‐Inspired Computing. *physica status solidi (RRL) – Rapid Research Letters* **2019**, *13*, 1900029.

[13] Ling, H.;Koutsouras, D. A.;Kazemzadeh, S.;Van De Burgt, Y.;Yan, F.; Gkoupidenis, P. Electrolyte-gated transistors for synaptic electronics, neuromorphic computing, and adaptable biointerfacing. *Applied Physics Reviews* **2020**, *7*, 011307.

[14] Zhu, J.;Zhang, T.;Yang, Y.; Huang, R. A comprehensive review on emerging artificial neuromorphic devices. *Applied Physics Reviews* **2020**, *7*, 011312.

[15] In *Principles of Neural Science, Fifth Edition*. McGraw-Hill Education; New York, NY, 2014.

[16] Sebastian, A.;Le Gallo, M.;Khaddam-Aljameh, R.; Eleftheriou, E. Memory devices and applications for in-memory computing. *Nature Nanotechnology* **2020**, *15*, 529-544.

[17] Monzio Compagnoni, C.;Yu, S.;Zhao, W.; Ielmini, D. Editorial: Novel materials, devices and solutions for brain-inspired sensing and computing. *Frontiers in Neuroscience* **2022**, *16*, 1099962.

[18] Xi, F.;Grenmyr, A.;Zhang, J.;Han, Y.;Bae, J. H.;Grützmacher, D.; Zhao, Q. T. Heterosynaptic Plasticity and Neuromorphic Boolean Logic Enabled by Ferroelectric Polarization Modulated Schottky Diodes. *Advanced Electronic Materials* **2023**, *9*, 2201155.

[19] Sung, S. H.;Jeong, Y.;Oh, J. W.;Shin, H.-J.;Lee, J. H.; Lee, K. J. Bio-plausible memristive neural components towards hardware implementation of brain-like intelligence. *Materials Today* **2023**, *62*, 251-270.

[20] Xie, Z.;Zhu, X.;Wang, W.;Guo, Z.;Zhang, Y.;Liu, H.;Sun, C.;Tang, M.;Gao, S.; Li, R. W. Temporal Pattern Coding in Ionic Memristor‐Based Spiking Neurons for Adaptive Tactile Perception. *Advanced Electronic Materials* **2022**, *8*, 2200334.

[21] Wang, T.;Wang, X.-X.;Wen, J.;Shao, Z.-Y.;Huang, H.-M.; Guo, X. A Bio‐Inspired Neuromorphic Sensory System. *Advanced Intelligent Systems* **2022**, *4*, 2200047.

[22] Wu, G.;Zhang, X.;Feng, G.;Wang, J.;Zhou, K.;Zeng, J.;Dong, D.;Zhu, F.;Yang, C.;Zhao, X.;Gong, D.;Zhang, M.;Tian, B.;Duan, C.;Liu, Q.;Wang, J.;Chu, J.; Liu, M. Ferroelectric-defined reconfigurable homojunctions for in-memory sensing and computing. *Nature Materials* **2023**, *22*, 1499-1506.

[23] Song, W.;Rao, M.;Li, Y.;Li, C.;Zhuo, Y.;Cai, F.;Wu, M.;Yin, W.;Li, Z.;Wei, Q.;Lee, S.;Zhu, H.;Gong, L.;Barnell, M.;Wu, Q.;Beerel, P. A.;Chen, M. S.-W.;Ge, N.;Hu, M.;Xia, Q.; Yang, J. J. Programming memristor arrays with arbitrarily high precision for analog computing. *Science* **2024**, *383*, 903-910.

[24] Wu, X.;Li, E.;Liu, Y.;Lin, W.;Yu, R.;Chen, G.;Hu, Y.;Chen, H.; Guo, T. Artificial multisensory integration nervous system with haptic and iconic perception behaviors. *Nano Energy* **2021**, *85*, 106000.

[25] Wang, J.;Wang, C.;Cai, P.;Luo, Y.;Cui, Z.;Loh, X. J.; Chen, X. Artificial Sense Technology: Emulating and Extending Biological Senses. *ACS Nano* **2021**, *15*, 18671-18678.

[26] Wang, P.;Li, J.;Xue, W.;Ci, W.;Jiang, F.;Shi, L.;Zhou, F.;Zhou, P.; Xu, X. Integrated In‐Memory Sensor and Computing of Artificial Vision Based on Full‐vdW Optoelectronic Ferroelectric Field‐Effect Transistor. *Advanced Science* **2024**, *11*.

[27] Hwang, S.;Lee, J.-J.;Kwon, M.-W.;Baek, M.-H.;Jang, T.;Chang, J.;Lee, J.-H.; Park, B.-G. Analog Complementary Metal–Oxide–Semiconductor Integrate-and-Fire Neuron Circuit for Overflow Retaining in Hardware Spiking Neural Networks. *Journal of Nanoscience and Nanotechnology* **2020**, *20*, 3117-3122.

[28] Zhang, Y.;Wang, Z.;Zhu, J.;Yang, Y.;Rao, M.;Song, W.;Zhuo, Y.;Zhang, X.;Cui, M.;Shen, L.;Huang, R.; Joshua Yang, J. Brain-inspired computing with memristors: Challenges in devices, circuits, and systems. *Applied Physics Reviews* **2020**, *7*, 011308.

[29] Sun, C.;Wang, X.;Xu, H.;Zhang, J.;Zheng, Z.;Kong, Q.;Kang, Y.;Han, K.;Jiao, L.;Zhou, Z.;Chen, Y.;Zhang, D.;Liu, G.;Liu, L.; Gong, X. Novel a-IGZO Anti-Ferroelectric FET LIF Neuron with Co-Integrated Ferroelectric FET Synapse for Spiking Neural Networks. In *Proceedings 2022 International Electron Devices Meeting (IEDM)*, pp 2.1.1-2.1.4.

[30] Kwon, J. Y.;Kim, J. E.;Kim, J. S.;Chun, S. Y.;Soh, K.; Yoon, J. H. Artificial sensory system based on memristive devices. *Exploration* **2024**, *4*.

[31] Zhong, S.;Zhang, Y.;Zheng, H.;Yu, F.; Zhao, R. Spike‐Based Spatiotemporal Processing Enabled by Oscillation Neuron for Energy‐Efficient Artificial Sensory Systems. *Advanced Intelligent Systems* **2022**, *4*, 2200076.

[32] Yang, Y.;Zhu, F.;Zhang, X.;Chen, P.;Wang, Y.;Zhu, J.;Ding, Y.;Cheng, L.;Li, C.;Jiang, H.;Wang, Z.;Lin, P.;Shi, T.;Wang, M.;Liu, Q.;Xu, N.; Liu, M. Firing feature-driven neural circuits with scalable memristive neurons for robotic obstacle avoidance. *Nature Communications* **2024**, *15*.

[33] Yuan, R.;Duan, Q.;Tiw, P. J.;Li, G.;Xiao, Z.;Jing, Z.;Yang, K.;Liu, C.;Ge, C.;Huang, R.; Yang, Y. A calibratable sensory neuron based on epitaxial VO2 for spike-based neuromorphic multisensory system. *Nature Communications* **2022**, *13*.

[34] Kandel, E. R.;Koester, J. D.;Mack, S. H.; Siegelbaum, S. A. Editors. In *Principles of Neural Science, 6e*. McGraw Hill; New York, NY, 2021.

[35] Hua, Q.;Wu, H.;Gao, B.;Zhang, Q.;Wu, W.;Li, Y.;Wang, X.;Hu, W.; Qian, H. Low-Voltage Oscillatory Neurons for Memristor-Based Neuromorphic Systems. *Glob Chall* **2019**, *3*, 1900015.

[36] Wang, X.;Huang, P.;Dong, Z.;Zhou, Z.;Jiang, Y.;Han, R.;Liu, L.;Liu, X.; Kang, J. A novel RRAM-based adaptive-threshold LIF neuron circuit for high recognition accuracy. In *2018 International Symposium on VLSI Technology, Systems and Application (VLSI-TSA)*; IEEE, 2018; pp 1-2.

[37] Gao, L.;Chen, P.-Y.; Yu, S. NbOx based oscillation neuron for neuromorphic computing. *Applied Physics Letters* **2017**, *111*.

[38] Lee, J.-J.;Park, J.;Kwon, M.-W.;Hwang, S.;Kim, H.; Park, B.-G. Integrated neuron circuit for implementing neuromorphic system with synaptic device. *Solid-State Electronics* **2018**, *140*, 34-40.

[39] Indiveri, G.;Linares-Barranco, B.;Hamilton, T. J.;van Schaik, A.;Etienne-Cummings, R.;Delbruck, T.;Liu, S. C.;Dudek, P.;Hafliger, P.;Renaud, S.;Schemmel, J.;Cauwenberghs, G.;Arthur, J.;Hynna, K.;Folowosele, F.;Saighi, S.;Serrano-Gotarredona, T.;Wijekoon, J.;Wang, Y.; Boahen, K. Neuromorphic silicon neuron circuits. *Front Neurosci* **2011**, *5*, 73.

[40] Zhang, G.;Zhang, G.;Luo, Q.;Luo, Q.;Yao, J.;Yao, J.;Zhong, S.;Zhong, S.;Wang, H.;Wang, H.;Xue, F.;Xue, F.;Yu, B.;Yu, B.;Loh, K. P.;Loh, K. P.;Zhang, Y.; Zhang, Y. All-in-one neuromorphic hardware with 2D material technology: current status and future perspective. *Chemical Society Reviews* **2025/09/15**, *54*.

[41] Wang, C.-Y.;Liang, S.-J.;Wang, S.;Wang, P.;Li, Z. a.;Wang,

Z.;Gao, A.;Pan, C.;Liu, C.;Liu, J.;Yang, H.;Liu, X.;Song, W.;Wang, C.;Cheng, B.;Wang, X.;Chen, K.;Wang, Z.;Watanabe, K.;Taniguchi, T.;Yang, J. J.; Miao, F. Gate-tunable van der Waals heterostructure for reconfigurable neural network vision sensor. *Science Advances* **2020-06**, *6*.

[42] Sangwan, V. K.;Liu, S. E.;Trivedi, A. R.; Hersam, M. C. Two-dimensional materials for bio-realistic neuronal computing networks. *Matter* **2022/12/07**, *5*.

[43] Pei, Y.;Yan, L.;Wu, Z.;Lu, J.;Zhao, J.;Chen, J.;Liu, Q.; Yan, X. Artificial Visual Perception Nervous System Based on Low-Dimensional Material Photoelectric Memristors. *ACS Nano* **2021**, *15*, 17319-17326.

[44] Aung, T.;Giridhar, S. P.;Abidi, I. H.;Ahmed, T.;AI-Hourani, A.; Walia, S. Photoactive Monolayer MoS2 for Spiking Neural Networks Enabled Machine Vision Applications. *Advanced Materials Technologies* **2025/08/01**, *10*.

[45] Sarkar, T.;Lieberth, K.;Pavlou, A.;Frank, T.;Mailaender, V.;McCulloch, I.;Blom, P. W. M.;Torricelli, F.;Gkoupidenis, P.;Sarkar, T.;Lieberth, K.;Pavlou, A.;Frank, T.;Mailaender, V.;McCulloch, I.;Blom, P. W. M.;Torricelli, F.; Gkoupidenis, P. An organic artificial spiking neuron for in situ neuromorphic sensing and biointerfacing. *Nature Electronics 2022 5:11* **2022-11-07**, *5*.

[46] Lee, D. H.;Kim, W.;Lee, E. K.; Yoo, H. Advances in Organic In‐Sensor Neuromorphic Computing: from Material Mechanisms to Applications. *Advanced Intelligent Discovery* **2025/12/01**, *1*.

[47] Tan, S. T. M.;Gumyusenge, A.;Quill, T. J.;LeCroy, G. S.;Bonacchini, G. E.;Denti, I.; Salleo, A. Mixed Ionic–Electronic Conduction, a Multifunctional Property in Organic Conductors. *Advanced Materials* **2022/05/01**, *34*.

[48] Fu, Y.;Zhou, Y.;Huang, X.;Dong, B.;Zhuge, F.;Li, Y.;He, Y.;Chai, Y.; Miao, X. Reconfigurable Synaptic and Neuronal Functions in a V/VOx/HfWOx/Pt Memristor for Nonpolar Spiking Convolutional Neural Network. *Advanced Functional Materials* **2022**, *32*.

[49] Wang, Z.;Zhang, G.;Fan, X.;Li, P.;Zhang, Z.;Xing, S.;Zhu, B.;Wan, Q.; Zhang, Y. Topology-Aware Recognition Framework Based on Ultra-High On/Off Ratio Memristors for Handwritten Digit Recognition. *IEEE Electron Device Letters* **2025**, *46*, 2349-2352.

[50] Fan, X.;Chen, A.;Li, Z.;Gong, Z.;Wang, Z.;Zhang, G.;Li, P.;Xu, Y.;Wang, H.;Wang, C.;Zhu, X.;Zhao, R.;Yu, B.; Zhang, Y. Metaplasticity-Enabled Graphene Quantum Dot Devices for Mitigating Catastrophic Forgetting in Artificial Neural Networks. *Adv Mater* **2025**, *37*, e2411237.

[51] Ielmini, D.;Wang, Z.; Liu, Y. Brain-inspired computing via memory device physics. *APL Materials* **2021**, *9*, 050702.

[52] Hua, Q.;Wu, H.;Gao, B.;Zhang, Q.;Wu, W.;Li, Y.;Wang, X.;Hu, W.; Qian, H. Low‐Voltage Oscillatory Neurons for Memristor‐Based Neuromorphic Systems. *Global Challenges* **2019**, *3*, 1900015.

[53] Chen, P.;Zhang, X.;Wu, Z.;Wang, Y.;Zhu, J.;Hao, Y.;Feng, G.;Sun, Y.;Shi, T.;Wang, M.; Liu, Q. High-Yield and Uniform NbOx -Based Threshold Switching Devices for Neuron Applications. *IEEE Transactions on Electron Devices* **2022**, *69*, 2391-2397.

[54] Wei, Y.;Duan, Q.;Yuan, R.;Yan, X.; Yang, Y. Dropout neuronal unit with tunable probability based on NbOx stochastic memristor for efficient suppression of overfitting. *Microelectronic Engineering* **2022**, *259*.

[55] Yang, G.;Chen, A.;Liu, N.;Ma, G.;Lin, Z.;Fu, Y.;Zhao, X.;Rao, Y.;Tao, L.;Wan, H.;Duan, J.;Shen, L.;Sun, P.;Yang, D.; Wang, H. Realization of Outstanding Stable 1S1R Behavior Based on Al-Doped NbOx. *IEEE Transactions on Electron Devices* **2023**, *70*, 65-69.

[56] Zhu, J.;Zhang, X.;Wang, M.;Wang, R.;Chen, P.;Cheng, L.; Liu, Q. An Artificial Spiking Nociceptor Integrating Pressure Sensors and Memristors. *IEEE Electron Device Letters* **2022**, *43*, 962-965.

[57] Maramreddy, S. R.;Arige, S.; Dixit, T. Elucidating the role of Device architecture for Mott-insulator based Memory technology. In *Proceedings 2024 IEEE 9th International Conference for Convergence in Technology (I2CT)*, pp 1-5.

[58] Ding, Y.;Li, Y.;Jia, S.;Chen, P.;Zhang, X.;Wang, W.;Li, Y.;Hao, Y.;Bi, J.;Gong, T.;Jiang, H.;Wang, M.;Liu, Q.;Xu, N.; Liu, M. Fatigue of NbOx-Based Locally Active Memristors—Part I: Experimental Characteristics. *IEEE Transactions on Electron Devices* **2023**, *70*, 6600-6605.

[59] Li, Y.;Ding, Y.;Zhang, X.;Jia, S.;Wang, W.;Li, Y.;Wang, M.;Jiang, H.;Liu, Q.;Xu, N.; Liu, M. Fatigue of NbOx-Based Locally Active Memristors—Part II: Mechanisms and Modeling. *IEEE Transactions on Electron Devices* **2023**, *70*, 6606-6612.

[60] Chen, J.;Zheng, X.;Tang, J.;Li, X.;Xu, F.;Gao, B.;Sun, W.;Qian, H.; Wu, H. Microscopic Modeling and Optimization of NbOx Mott Memristor for Artificial Neuron Applications. *IEEE Transactions on Electron Devices* **2022**, *69*, 6686-6692.

[61] Liu, G.;Li, F.;Chen, Y.;Ren, H.;Li, D.;Wang, Y.;Tang, Y.;Zhang, Z.;Wang, R.;Wang, H.; Zhu, B. Experimental Demonstration of Coplanar NbOx Mott Memristors for Spiking Neurons. *IEEE Electron Device Letters* **2024**, *45*, 708-711.

[62] Hoffmann, A.;Ramanathan, S.;Grollier, J.;Kent, A. D.;Rozenberg, M. J.;Schuller, I. K.;Shpyrko, O. G.;Dynes, R. C.;Fainman, Y.;Frano, A.;Fullerton, E. E.;Galli, G.;Lomakin, V.;Ong, S. P.;Petford-Long, A. K.;Schuller, J. A.;Stiles, M. D.;Takamura, Y.; Zhu, Y. Quantum materials for energy-efficient neuromorphic computing: Opportunities and challenges. *APL Materials* **2022**, *10*.

[63] Wang, Y.;Su, C.;Zheng, Y.;Zhou, K.;Wen, Z.;Fu, Y.;Wang, Q.; He, D. High consistency VO2 memristor for artificial auditory neuron. *Microelectronic Engineering* **2023**, *282*.

[64] Varanasi, A.;Devabharathi, N.;Divya, M.;Mondal, S. K.; Dasgupta, S. Printed and Room Temperature Processed Nanoparticulate VO2 Thin Films Toward Memristive Device Applications. *IEEE Journal on Flexible Electronics* **2023**, *2*, 414-420.

[65] Shi, R.;Kong, D.;Shen, N.;Gan, Y.;Zhao, Y.;Wang, Z.;Wang, W.;Wang, J.;Amini, A.;Wang, N.; Cheng, C. Low-temperature wafer-scale fabrication of vertical VO2 nanowire arrays. *Applied Physics Letters* **2020**, *117*.

[66] Kim, H. W.;Kang, S.-Y.;Moon, J.;Kim, N.;Hong, E.;Jeon, S.;Jeon, S.; Woo, J. Experimental Robust Spontaneous Synchronizations in Coupled NbOx Oscillation Neurons for Unconventional Computing. *IEEE Transactions on Electron Devices* **2023**, *70*, 6699-6702.

[67] Wright, J. P.;Sarles, S. A.; Pei, J.-S. DC operating points of Mott neuristor circuits. *Microelectronic Engineering* **2024**, *284-285*.

[68] Fan, S.;Lu, Z.;Ma, W.;Fang, S.;Chen, K.;Ma, B.;Han, C.;Zhang, G.; Geng, L. A Low-Power Sensing System Architecture With Mott Memristor and Time-to-Digital Converter for Large-Scale Sensor-Array Application. *IEEE Transactions on Circuits and Systems II: Express Briefs* **2023**, *70*, 3842-3846.

[69] Delacour, C.; Todri-Sanial, A. Mapping Hebbian Learning Rules to Coupling Resistances for Oscillatory Neural Networks. *Frontiers in Neuroscience* **2021**, *15*.

[70] FANG Shengli;REN Wenjun;ZHAO Shujing;WANG Ruilin ;LIU Weihua;LI Xin;ZHANG Guohe;WANG Xiaoli;GENG Li; HAN Chuanyu Research Progress on Artificial Spiking Neurons for Neuromorphic Perception. *MICROELECTRONICS*, *54*, 1-16.

[71] Zhu, J.-X.;Zhang, X.-M.;Wang, R.; Liu, Q. Flexible memristive spiking neuron for neuromorphic sensing and computing. *Acta Physica Sinica* **2022**, *71*.

[72] Han, C. Y.;Han, Z. R.;Fang, S. L.;Fan, S. Q.;Yin, J. Q.;Liu, W. H.;Li, X.;Yang, S. Q.;Zhang, G. H.;Wang, X. L.; Geng, L. Characterization and Modelling of Flexible VO2 Mott Memristor for the Artificial Spiking Warm Receptor. *Advanced Materials Interfaces* **2022**, *9*.

[73] Zhao, S.;Han, C. Y.;Tian, F.;Yuan, Y.;Chai, J.;Xu, H.;Fan, S.;Li, X.;Liu, W.;Li, C.;Tang, W. M.;Lai, P. T.;Huang, X.;Zhang, G.;Geng, L.; Wang, X. A 1T1M programmable artificial spiking neuron via the integration of FeFET and NbOx Mott memristor. *IEEE Electron Device Letters* **2024**, 10.1109/led.2024.3395024, 1-1.

[74] Yuan, R.;Tiw, P. J.;Cai, L.;Yang, Z. Y.;Liu, C.;Zhang, T.;Ge, C.;Huang, R.; Yang, Y. C. A neuromorphic physiological signal processing system based on VO2 memristor for next-generation human-machine interface. *Nature Communications* **2023**, *14*.

[75] Kumar, S.;Williams, R. S.; Wang, Z. Third-order nanocircuit elements for neuromorphic engineering. *Nature* **2020**, *585*, 518-523.

[76] Pickett, M. D.; Stanley Williams, R. Sub-100 fJ and sub-nanosecond thermally driven threshold switching in niobium oxide crosspoint nanodevices. *Nanotechnology* **2012**, *23*.

[77] Burkitt, A. N. A review of the integrate-and-fire neuron model: I. Homogeneous synaptic input. *Biol Cybern* **2006**, *95*, 1-19.

[78] Lee, D.;Kwak, M.;Moon, K.;Choi, W.;Park, J.;Yoo, J.;Song, J.;Lim, S.;Sung, C.;Banerjee, W.; Hwang, H. Various Threshold

Switching Devices for Integrate and Fire Neuron Applications. *Advanced Electronic Materials* **2019**, *5*.

[79] Izhikevich, E. M. Which Model to Use for Cortical Spiking Neurons? *IEEE Transactions on Neural Networks* **2004**, *15*, 1063-1070.

[80] Del Valle, J.;Salev, P.;Kalcheim, Y.; Schuller, I. K. A caloritronics-based Mott neuristor. *Sci Rep* **2020**, *10*, 4292.

[81] Ganguly, C.;Bezugam, S. S.;Abs, E.;Payvand, M.;Dey, S.; Suri, M. Spike frequency adaptation: bridging neural models and neuromorphic applications. *Communications Engineering* **2024**, *3*, 22.

[82] Shaban, A.;Bezugam, S. S.; Suri, M. An adaptive threshold neuron for recurrent spiking neural networks with nanodevice hardware implementation. *Nature Communications* **2021**, *12*.

[83] Yin, B. J.;Corradi, F.; Bohté, S. M. Accurate and efficient time-domain classification with adaptive spiking recurrent neural networks. *Nature Machine Intelligence* **2021**, *3*, 905-+.

[84] Li, X.;Sun, J.;Sun, Y.;Wang, C.;Hong, Q.;Du, S.; Zhang, J. Design of Artificial Neurons of Memristive Neuromorphic Networks Based on Biological Neural Dynamics and Structures. *IEEE Transactions on Circuits and Systems I: Regular Papers* **2024**, *71*, 2320-2333.

[85] Yi, W.;Tsang, K. K.;Lam, S. K.;Bai, X.;Crowell, J. A.; Flores, E. A. Biological plausibility and stochasticity in scalable VO(2) active memristor neurons. *Nat Commun* **2018**, *9*, 4661.

[86] Sun, W.;Gao, B.;Chi, M.;Xia, Q.;Yang, J. J.;Qian, H.; Wu, H. Understanding memristive switching via in situ characterization and device modeling. *Nature Communications* **2019**, *10*.

[87] Wang, Y.;Zhou, G.;Sun, B.;Wang, W.;Li, J.;Duan, S.; Song, Q. Ag/HfO_x/Pt Unipolar Memristor for High-Efficiency Logic Operation. *The Journal of Physical Chemistry Letters* **2022**, *13*, 8019-8025.

[88] Lee, D.;Kwak, M.;Moon, K.;Choi, W.;Park, J.;Yoo, J.;Song, J.;Lim, S.;Sung, C.;Banerjee, W.; Hwang, H. Various Threshold Switching Devices for Integrate and Fire Neuron Applications. *Advanced Electronic Materials* **2019**, *5*, 1800866.

[89] Hong, E.;Kim, H. W.;Choi, H.;Jeon, S.;Kim, N.; Woo, J. Demonstration of Threshold Switching in Undoped SiOx Layer for Oscillation Neurons. *IEEE Transactions on Electron Devices* **2024**, *71*, 2228-2232.

[90] Chen, C.;He, Y.;Mao, H.;Zhu, L.;Wang, X.;Zhu, Y.;Zhu, Y.;Shi, Y.;Wan, C.; Wan, Q. A Photoelectric Spiking Neuron for Visual Depth Perception. *Advanced Materials* **2022**, *34*, 2201895.

[91] Zhang, Z.;Gao, S.;Li, Z.;Xu, Y.;Yang, R.; Miao, X. Artificial LIF Neuron With Bursting Behavior Based on Threshold Switching Device. *IEEE Transactions on Electron Devices* **2023**, *70*, 1374-1379.

[92] Abbott, L. F.; Regehr, W. G. Synaptic computation. *Nature* **2004**, *431*, 796-803.

[93] Yoon, C.;Oh, G.;Kim, S.;Jeon, J.;Lee, J. H.;Kim, Y. H.; Park, B. H. Implementation of threshold- and memory-switching memristors based on electrochemical metallization in an identical ferroelectric electrolyte. *NPG Asia Materials* **2023**, *15*, 33.

[94] Kau, D.;Tang, S.;Karpov, I. V.;Dodge, R.;Klehn, B.;Kalb, J. A.;Strand, J.;Diaz, A.;Leung, N.;Wu, J.;Lee, S.;Langtry, T.;Chang, K.-w.;Papagianni, C.;Lee, J.;Hirst, J.;Erra, S.;Flores, E.;Righos, N.;Castro, H.; Spadini, G. A stackable cross point Phase Change Memory. In *2009 IEEE International Electron Devices Meeting (IEDM)*; IEEE, 2009; pp 1-4.

[95] Cao, Y.;Wang, S.;Wang, R.;Sun, J.;Yang, M.;Ma, X.;Wang, H.; Hao, Y. Physically Transient Artificial Neuron Based on Mg/Magnesium Oxide Threshold Switching Memristor. *IEEE Transactions on Electron Devices* **2023**, *70*, 2047-2051.

[96] Zhao, Z.;Clima, S.;Garbin, D.;Degraeve, R.;Pourtois, G.;Song, Z.;Zhu, M.;Zhao, Z.;Clima, S.;Garbin, D.;Degraeve, R.;Pourtois, G.;Song, Z.; Zhu, M. Chalcogenide Ovonic Threshold Switching Selector. *Nano-Micro Letters 2024 16:1* **2024-01-11**, *16*.

[97] Author Multiple resistance semiconductor elements. 1966.

[98] Ovshinsky, S. R. Reversible Electrical Switching Phenomena in Disordered Structures. *Physical Review Letters* **1968-11-11**, *21*.

[99] Clima, S.;Govoreanu, B.;Opsomer, K.;Velea, A.;Avasarala, N. S.;Devulder, W.;Shlyakhov, I.;Donadio, G. L.;Witters, T.;Kundu, S.;Goux, L.;Afanasiev, V.;Kar, G. S.; Pourtois, G. Atomistic investigation of the electronic structure, thermal properties and conduction defects in Ge-rich GexSe1−x materials for selector applications | IEEE Conference Publication | IEEE Xplore. *2017 IEEE International Electron Devices Meeting (IEDM)* **2017**, 10.1109/IEDM.2017.8268323.

[100] Hatem, F.;Chai, Z.;Zhang, W.;Fantini, A.;Degraeve, R.;Clima, S.;Garbin, D.;Robertson, J.;Guo, Y.;Zhang, J. F.;Marsland, J.;Freitas, P.;Goux, L.; Kar, G. S. Endurance improvement of more than five orders in GexSe1-x OTS selectors by using a novel refreshing program scheme | IEEE Conference Publication | IEEE Xplore. *2019 IEEE International Electron Devices Meeting (IEDM)* **2019**, 10.1109/IEDM19573.2019.8993448.

[101] Wu, R.;Jia, S.;Gotoh, T.;Luo, Q.;Song, Z.; Zhu, M. Screening Switching Materials with Low Leakage Current and High Thermal Stability for Neuromorphic Computing. *Advanced Electronic Materials* **2022**, *8*, 2200150.

[102] Jeon, J. W.;Park, B.;Jang, Y. H.;Lee, S. H.;Jeon, S.;Han, J.;Ryoo, S. K.;Kim, K. D.;Shim, S. K.;Cheong, S.;Choi, W.;Jeon, G.;Kim, S.;Yoo, C.;Han, J.-K.; Hwang, C. S. Vertically Stackable Ovonic Threshold Switch Oscillator Using Atomic Layer Deposited $Ge_{0.6}Se_{0.4}$ Film for High-Density Artificial Neural Networks. *ACS Applied Materials & Interfaces* **2024**, *16*, 15032-15042.

[103] Li, K.;Yao, J.;Zhao, P.;Luo, Y.;Ge, X.;Yang, R.;Cheng, X.; Miao, X. Ovonic threshold switching-based artificial afferent neurons for thermal in-sensor computing. *Materials Horizons* **2024**, 10.1039/D4MH00053F, 10.1039.D1034MH00053F.

[104] Lee, M.;Cho, S. W.;Kim, S. J.;Kwak, J. Y.;Ju, H.;Yi, Y.;Cheong, B.-k.; Lee, S. Simple Artificial Neuron Using an Ovonic Threshold Switch Featuring Spike-Frequency Adaptation and Chaotic Activity. *Physical Review Applied* **2020**, *13*, 064056.

[105] Lai, S.; Lowrey, T. OUM - A 180 nm nonvolatile memory cell element technology for stand alone and embedded applications. *International Electron Devices Meeting. Technical Digest (Cat. No.01CH37224)* **2010**, 10.1109/IEDM.2001.979636.

[106] Fantini, P. Phase change memory applications: the history, the present and the future. *Journal of Physics D: Applied Physics* **2020**, *53*, 283002.

[107] Suri, M.;Bichler, O.;Querlioz, D.;Traoré, B.;Cueto, O.;Perniola, L.;Sousa, V.;Vuillaume, D.;Gamrat, C.; DeSalvo, B. Physical aspects of low power synapses based on phase change memory devices. *Journal of Applied Physics* **2012**, *112*, 054904.

[108] Wang, W.;Pedretti, G.;Milo, V.;Carboni, R.;Calderoni, A.;Ramaswamy, N.;Spinelli, A. S.; Ielmini, D. Learning of spatiotemporal patterns in a spiking neural network with resistive switching synapses. *Science Advances* **2018**, *4*, eaat4752.

[109] Mazzarello, R. Phase-Change Materials for Neuromorphic Computing. In *2023 IEEE Nanotechnology Materials and Devices Conference (NMDC)*; IEEE, 2023; pp 728-728.

[110] Tuma, T.;Pantazi, A.;Le Gallo, M.;Sebastian, A.; Eleftheriou, E. Stochastic phase-change neurons. *Nature Nanotechnology* **2016**, *11*, 693-699.

[111] Liang, F.-X.;Wang, I.-T.; Hou, T.-H. Progress and Benchmark of Spiking Neuron Devices and Circuits. *Advanced Intelligent Systems* **2021**, *3*, 2100007.

[112] Cobley, R. A.;Hayat, H.; Wright, C. D. A self-resetting spiking phase-change neuron. *Nanotechnology* **2018**, *29*, 195202.

[113] Chakraborty, I.;Saha, G.;Sengupta, A.; Roy, K. Toward Fast Neural Computing using All-Photonic Phase Change Spiking Neurons. *Scientific Reports* **2018**, *8*, 12980.

[114] Kumar, M.;Bezugam, S. S.; Suri, M. CMOS-PCM Based Artificial Thermosensory Neuron for Bio-Inspired Sensing. In *2023 IEEE 23rd International Conference on Nanotechnology (NANO)*; IEEE, 2023; pp 121-126.

[115] Zhang, Y.;Ren, S.-G.;Zuo, W.-B.;Xue, Y.-B.;Sun, J.-Y.;Xue, K.-H.;Li, Y.; Miao, X.-S. Realizing Performance Balance by Band Offset and Defect Concentration Engineering in HfOx/ZrOy Self-Rectifying Memristor. *IEEE Electron Device Letters* **2025**, *46*, 1317-1320.

[116] Wang, J.;Liu, L.;Zhao, X.;Zhang, Y.; Yan, Y. Reconfigurable Counterion Gradient around Charged Metal Nanoparticles Enables Self-Rectifying and Volatile Artificial Synapse. *Nano Lett* **2025**, *25*, 13243-13250.

[117] Tan, T.;Sivan, M.;Zhou, K.;Guo, H.;Wu, Y.;Sun, L.;Li, Y.; Feng, X. Self-Rectifying MoS(2) Memtransistor via Asymmetry Contact Metal Engineering for Neuromorphic Computing. *Small* **2025**, 10.1002/smll.202503716, e2503716.

[118] Wang, Z.;Zhang, J.;Jia, G.;Sun, W.;Yin, S.;Niu, J.;Bai, J.;Liu, C.;Zhao, Z.; Yan, X. Self-rectifying memristors based on epitaxial AlScN for neuromorphic computing. *Applied Physics Letters* **2025**, *127*.

[119] Pham, P. Q.;Tran, T. A.;Vo Van Anh, T.;Nguyen, T. D.;Brugger, J.;Kawazoe, Y.;Phan, T. B.;Nguyen, T. T.;Vu, N. H.; Pham, N. K. Selector‐Free 16 × 16 CrOX/TiO2‐Based Memristor Array for Synaptic Dynamics and LTP/ LTD Emulation: Experimental–Computational Correlation. *Advanced Functional Materials* **2025**,

10.1002/adfm.202516695.

[120] Cho, J. M.;Kim, S. S.;Park, T. W.;Shin, D. H.;Kim, Y. R.;Park, H. J.;Kim, D. Y.;Lee, S. H.;Park, T.; Hwang, C. S. Concealable physical unclonable function generation and an in-memory encryption machine using vertical self-rectifying memristors. *Nanoscale Horiz* **2024**, *10*, 113-123.

[121] Fan, X.;Wang, Z.;Yu, H.;Zhang, G.;Li, P.;Zhang, Z.;Zhu, X.; Zhang, Y. Superior rectification self-rectifying memristors with self-recovery capabilities enabled by GaOx/InOx heterostructures. *Applied Physics Letters* **2025**, *127*.

[122] Zhang, G.;Wang, Z.;Fan, X.;Luo, Q.;Li, P.;Zhang, Z.;Huang, K.;Ma, Y.;Zhang, Y.;Gao, D.;Yu, B.;Wan, Q.;Miao, X.; Zhang, Y. Stochastic self-rectifying memristor crossbar array as physical unclonable function for authentication and tamper-evident image security. *Device* **2025**, 10.1016/j.device.2025.100988.

[123] Luo, Y.;Li, Z.;Lin, X.;Hu, K.;Song, D.;Chen, X.;Du, H.;Wang, F.;Wang, Y.;Xu, C.;Song, Z.; Zhang, K. Application of Circuit Model Based on Self-Rectifying Al2O3/TaOX Memristor and Generation of Physically Unclonable Functions. *IEEE Transactions on Electron Devices* **2025**, *72*, 4090-4095.

[124] Zhang, G.;Fan, X.;Wang, J.;Wang, Z.;Zhang, Z.;Li, P.;Ma, Y.;Huang, K.;Yu, B.;Wan, Q.;Miao, X.; Zhang, Y. Self-rectifying memristors with high rectification ratio for attack-resilient autonomous driving systems. *Nat Commun* **2025**, *16*, 5759.

[125] Park, S. O.;Jeong, H.;Park, J.;Bae, J.; Choi, S. Experimental demonstration of highly reliable dynamic memristor for artificial neuron and neuromorphic computing. *Nat Commun* **2022**, *13*, 2888.

[126] Cai, B.;Wang, C.;Chen, K.;Sun, Q.;Zhang, D. W.; Chen, L. A Multifunctional Self-Rectifying Memristor Enabling LIF Neuron and Nociceptor Behaviors. *IEEE Electron Device Letters* **2025**, 10.1109/led.2025.3614142, 1-1.

[127] Yun, S.-Y.;Han, J.-K.;Lee, S.-W.;Yu, J.-M.;Jeon, S.-B.; Choi, Y.-K. Self-aware artificial auditory neuron with a triboelectric sensor for spike-based neuromorphic hardware. *Nano Energy* **2023**, *109*.

[128] Yun, S.-Y.;Han, J.-K.; Choi, Y.-K. A Nanoscale Bistable Resistor for an Oscillatory Neural Network. *Nano Letters* **2024**, *24*, 2751-2757.

[129] Kim, H.-Y.;Kim, S.-I.;Han, J.-K.;Jung, J.-W.; Choi, Y.-K. A Single MOSFET-Based Oscillator on a Bulk-Silicon Wafer. *IEEE Electron Device Letters* **2024**, *45*, 8-11.

[130] Kim, Y.;Kim, H.;Oh, K.;Park, J. H.; Baek, C. K. Highly biomimetic spiking neuron using SiGe heterojunction bipolar transistors for energy-efficient neuromorphic systems. *Sci Rep* **2024**, *14*, 8356.

[131] Mori, T.; Ida, J. Neuronal Function and Signal Amplification Device with Steep Switching “PN-Body Tied SOI-FET”. In *Proceedings 2023 International VLSI Symposium on Technology, Systems and Applications (VLSI-TSA/VLSI-DAT)*, pp 1-2.

[132] Han, J.-K.;Seo, M.;Kim, W.-K.;Kim, M.-S.;Kim, S.-Y.;Kim, M.-S.;Yun, G.-J.;Lee, G.-B.;Yu, J.-M.; Choi, Y.-K. Mimicry of Excitatory and Inhibitory Artificial Neuron With Leaky Integrate-and-Fire Function by a Single MOSFET. *IEEE Electron Device Letters* **2020**, *41*, 208-211.

[133] Han, J.-K.;Seo, M.;Yu, J.-M.;Suh, Y.-J.; Choi, Y.-K. A Single Transistor Neuron With Independently Accessed Double-Gate for Excitatory-Inhibitory Function and Tunable Firing Threshold Voltage. *IEEE Electron Device Letters* **2020**, *41*, 1157-1160.

[134] Ding, Q.-a.;Gu, C.;Li, J.;Li, X.;Hou, B.;Peng, Y.;Chen, B.; Yao, Y. Mimicking the retinal neuron functions by a photoresponsive single transistor with double-gate. *Biophysical Journal* **2024**, 10.1016/j.bpj.2024.05.023.

[135] A century of ferroelectricity. *Nature Materials* **2020**, *19*, 129-129.

[136] Kim, I. J.; Lee, J. S. Ferroelectric Transistors for Memory and Neuromorphic Device Applications. *Advanced Materials* **2023**, *35*.

[137] Dutta, S.;Schafer, C.;Gomez, J.;Ni, K.;Joshi, S.; Datta, S. Supervised Learning in All FeFET-Based Spiking Neural Network: Opportunities and Challenges. *Frontiers in Neuroscience* **2020**, *14*.

[138] Liang, F.-X.;Wang, I. T.; Hou, T.-H. Progress and Benchmark of Spiking Neuron Devices and Circuits. *Advanced Intelligent Systems* **2021**, *3*.

[139] Zhang, Z.;Tian, G.;Huo, J.;Zhang, F.;Zhang, Q.;Xu, G.;Wu, Z.;Cheng, Y.;Liu, Y.; Yin, H. Recent progress of hafnium oxide-based ferroelectric devices for advanced circuit applications. *Science China Information Sciences* **2023**, *66*.

[140] Covi, E.;Mulaosmanovic, H.;Max, B.;Slesazeck, S.; Mikolajick, T. Ferroelectric-based synapses and neurons for neuromorphic computing. *Neuromorphic Computing and Engineering* **2022**, *2*.

[141] Zhao, J.;Chen, B.;Liu, N.;Zhou, J.;Cheng, R.;Liu, Y.; Han, G. Voltage Bias Scheme Optimization in FeFET Based Neural Network System. *IEEE Electron Device Letters* **2023**, *44*, 1464-1467.

[142] Zhou, Y.;Shao, H.;Zhu, R.;Luo, W.;Huang, W.;Shan, L.;Huang, R.; Tang, K. Hybrid-FE-Layer FeFET With High Linearity and Endurance Toward On-Chip CIM by Array Demonstration. *IEEE Electron Device Letters* **2024**, *45*, 276-279.

[143] Covi, E.;Lancaster, S.;Slesazeck, S.;Deshpande, V.;Mikolajick, T.; Dubourdieu, C. Challenges and Perspectives for Energy-efficient Brain-inspired Edge Computing Applications (Invited Paper). In *Proceedings 2022 IEEE International Conference on Flexible and Printable Sensors and Systems (FLEPS)*, pp 1-4.

[144] Thomann, S.;Nguyen, H. L. G.;Genssler, P. R.; Amrouch, H. All-in-Memory Brain-Inspired Computing Using FeFET Synapses. *Frontiers in Electronics* **2022**, *3*.

[145] Chen, H. J. Y.;Beauchamp, M.;Toprasertpong, K.;Huang, F.;Le Coeur, L.;Nemec, T.;Wong, H. S. P.; Boahen, K. Multi-gate FeFET Discriminates Spatiotemporal Pulse Sequences for Dendrocentric Learning. In *Proceedings 2023 International Electron Devices Meeting (IEDM)*, pp 1-4.

[146] Matsui, C.;Toprasertpong, K.;Takagi, S.; Takeuchi, K. FeFET Local Multiply and Global Accumulate Voltage-Sensing Computation-In-Memory Circuit Design for Neuromorphic Computing. *IEEE Transactions on Very Large Scale Integration (VLSI) Systems* **2024**, *32*, 468-479.

[147] Niu, X.;Tian, B.;Zhu, Q.;Dkhil, B.; Duan, C. Ferroelectric polymers for neuromorphic computing. *Applied Physics Reviews* **2022**, *9*.

[148] Li, C.;Jiang, C.; Chen, H. Investigation of electrical characteristics of a novel FeFET-based relaxation oscillator. In *Proceedings 2023 IEEE 15th International Conference on ASIC (ASICON)*, pp 1-3.

[149] Rajasekharan, D.;Gaidhane, A.;Trivedi, A. R.; Chauhan, Y. S. Ferroelectric FET-Based Implementation of FitzHugh-Nagumo Neuron Model. *IEEE Transactions on Computer-Aided Design of Integrated Circuits and Systems* **2022**, *41*, 2107-2114.

[150] Lee, G.;Oh, J.;Shin, E. J.;Kim, S.;Park, Y.;Kim, M. J.;Choi, S.-Y.; Cho, B. J. A Novel Structured Single Device Neuron for Low Standby Power and Compact System Application. *IEEE Electron Device Letters* **2023**, *44*, 528-531.

[151] Cao, R.;Zhang, X.;Liu, S.;Lu, J.;Wang, Y.;Jiang, H.;Yang, Y.;Sun, Y.;Wei, W.;Wang, J.;Xu, H.;Li, Q.; Liu, Q. Compact artificial neuron based on anti-ferroelectric transistor. *Nature Communications* **2022**, *13*.

[152] Tian, F.;Zhao, S.;Xu, H.;Xiang, J.;Li, T.;Xiong, W.;Duan, J.;Chai, J.;Han, K.;Wang, X.;Wang, W.; Ye, T. Impact of Interlayer and Ferroelectric Materials on Charge Trapping During Endurance Fatigue of FeFET With TiN/HfxZr1-xO2/Interlayer/Si (MFIS) Gate Structure. *IEEE Transactions on Electron Devices* **2021**, *68*, 5872-5878.

[153] Kim, S. J.;Lee, H.-J.;Lee, C.-H.;Jang, H. W.;Kim, S. J.;Lee, H.-J.;Lee, C.-H.; Jang, H. W. 2D materials-based 3D integration for neuromorphic hardware. *npj 2D Materials and Applications 2024 8:1* **2024-11-04**, *8*.

[154] Lemme, M. C.;Akinwande, D.;Huyghebaert, C.;Stampfer, C.;Lemme, M. C.;Akinwande, D.;Huyghebaert, C.; Stampfer, C. 2D materials for future heterogeneous electronics. *Nature Communications 2022 13:1* **2022-03-16**, *13*.

[155] Sangwan, V. K.;Hersam, M. C.;Sangwan, V. K.; Hersam, M. C. Neuromorphic nanoelectronic materials. *Nature Nanotechnology 2020 15:7* **2020-03-02**, *15*.

[156] Pendurthi, R.;Sakib, N. U.;Sadaf, M. U. K.;Zhang, Z.;Sun, Y.;Chen, C.;Jayachandran, D.;Oberoi, A.;Ghosh, S.;Kumari, S.;Stepanoff, S. P.;Somvanshi, D.;Yang, Y.;Redwing, J. M.;Wolfe, D. E.;Das, S.;Pendurthi, R.;Sakib, N. U.;Sadaf, M. U. K.;Zhang, Z.;Sun, Y.;Chen, C.;Jayachandran, D.;Oberoi, A.;Ghosh, S.;Kumari, S.;Stepanoff, S. P.;Somvanshi, D.;Yang, Y.;Redwing, J. M.;Wolfe, D. E.; Das, S. Monolithic three-dimensional integration of complementary two-dimensional field-effect transistors. *Nature Nanotechnology 2024 19:7* **2024-07-23**, *19*.

[157] Seo, S.;Jo, S.-H.;Kim, S.;Shim, J.;Oh, S.;Kim, J.-H.;Heo, K.;Choi, J.-W.;Choi, C.;Oh, S.;Kuzum, D.;Wong, H.-S. P.;Park, J.-H.;Seo, S.;Jo, S.-H.;Kim, S.;Shim, J.;Oh, S.;Kim, J.-H.;Heo, K.;Choi, J.-W.;Choi, C.;Oh, S.;Kuzum, D.;Wong, H.-S. P.; Park,

J.-H. Artificial optic-neural synapse for colored and color-mixed pattern recognition. *Nature Communications 2018 9:1* **2018-11-30**, *9*.

[158] Kaniselvan, M.;Jeon, Y.-R.;Mladenović, M.;Luisier, M.;Akinwande, D.;Kaniselvan, M.;Jeon, Y.-R.;Mladenović, M.;Luisier, M.; Akinwande, D. Mechanisms of resistive switching in two-dimensional monolayer and multilayer materials. *Nature Materials 2025 24:9* **2025-03-24**, *24*.

[159] Chen, J.;Zhou, Z.;Kim, B. J.;Zhou, Y.;Wang, Z.;Wan, T.;Yan, J.;Kang, J.;Ahn, J.-H.;Chai, Y.;Chen, J.;Zhou, Z.;Kim, B. J.;Zhou, Y.;Wang, Z.;Wan, T.;Yan, J.;Kang, J.;Ahn, J.-H.; Chai, Y. Optoelectronic graded neurons for bioinspired in-sensor motion perception. *Nature Nanotechnology 2023 18:8* **2023-04-20**, *18*.

[160] Wang, Y.;Gou, S.;Dong, X.;Chen, X.;Wang, X.;Sun, Q.;Xia, Y.;Zhu, Y.;Zhang, Z.;Wang, D.;Zhang, J.;Guo, X.;Tong, L.;Ma, J.;Xu, Z.;Xie, Y.;Ma, S.;Zhou, P.;Chai, Y.;Bao, W.;Wang, Y.;Gou, S.;Dong, X.;Chen, X.;Wang, X.;Sun, Q.;Xia, Y.;Zhu, Y.;Zhang, Z.;Wang, D.;Zhang, J.;Guo, X.;Tong, L.;Ma, J.;Xu, Z.;Xie, Y.;Ma, S.;Zhou, P.;Chai, Y.; Bao, W. A biologically inspired artificial neuron with intrinsic plasticity based on monolayer molybdenum disulfide. *Nature Electronics 2025 8:8* **2025-08-11**, *8*.

[161] Li, H.;Hu, J.;Zhang, Y.;Chen, A.;Zhou, J.;Zhao, Y.;Xu, Y.; Yu, B. Single‐Transistor Optoelectronic Spiking Neuron with Optogenetics‐Inspired Spatiotemporal Dynamics. *Advanced Functional Materials* **2024/05/01**, *34*.

[162] Huo, J.;Li, L.;Zheng, H.;Gao, J.;Tun, T. T. T.;Xiang, H.; Ang, K.-W. Compact Physical Implementation of Spiking Neural Network Using Ambipolar WSe2 n-Type/p-Type Ferroelectric Field-Effect Transistor. *ACS Nano* **October 3, 2024**, *18*.

[163] Hu, J.;Li, H.;Zhang, Y.;Zhou, J.;Zhao, Y.;Xu, Y.; Yu, B. Reconfigurable Neuromorphic Computing with 2D Material Heterostructures for Versatile Neural Information Processing. *Nano Letters* **July 22, 2024**, 10.1021/acs.nanolett.4c02658.

[164] Pouille, F.; Scanziani, M. Enforcement of Temporal Fidelity in Pyramidal Cells by Somatic Feed-Forward Inhibition. *Science* **2001**, *293*, 1159-1163.

[165] Li, H.;Hu, J.;Chen, A.;Zhang, Y.;Wang, C.;Wang, B.;Tong, Y.;Zhou, J.;Loh, K. P.;Xu, Y.;Hasan, T.; Yu, B. Core processing neuron‐enabled circuit motifs for neuromorphic computing. *InfoMat* **2023**, *5*.

[166] Liang, X.;Su, D.;Tang, Y.;Xi, B.;Yang, C.;Xiu, H.;Wang, J.;Liu, C.;Wang, M.;Chai, Y.;Liang, X.;Su, D.;Tang, Y.;Xi, B.;Yang, C.;Xiu, H.;Wang, J.;Liu, C.;Wang, M.; Chai, Y. Lab-on-device investigation of phase transition in MoOx semiconductors. *Nature Communications 2025 16:1* **2025-05-23**, *16*.

[167] Wang, M.;Luo, Y.;Wang, T.;Wan, C.;Pan, L.;Pan, S.;He, K.;Neo, A.; Chen, X. Artificial Skin Perception. *Adv Mater* **2021**, *33*, e2003014.

[168] Fang, S. L.;Han, C. Y.;Liu, W.;Han, Z. R.;Ma, B.;Cui, Y. L.;Fan, S. Q.;Li, X.;Wang, X. L.;Zhang, G. H.;Yin, J. Q.;Huang, X. D.; Geng, L. A bioinspired flexible artificial mechanoreceptor based on VO2 insulator-metal transition memristor. *Journal of Alloys and Compounds* **2022**, *911*.

[169] Nath, S. K.;Das, S. K.;Nandi, S. K.;Xi, C.;Marquez, C. V.;Rúa, A.;Uenuma, M.;Wang, Z.;Zhang, S.;Zhu, R.-J.;Eshraghian, J.;Sun, X.;Lu, T.;Bian, Y.;Syed, N.;Pan, W.;Wang, H.;Lei, W.;Fu, L.;Faraone, L.;Liu, Y.; Elliman, R. G. Optically Tunable Electrical Oscillations in Oxide‐Based Memristors for Neuromorphic Computing. *Advanced Materials* **2024/06/01**, *36*.

[170] Han, C. Y.;Zhao, S.;Fang, S. L.;Liu, W.;Tang, W. M.;Lai, P. T.;Li, C.;Ma, Y. X.;Song, J. Q.;Li, X.;Wang, X. L.;Ren, W. J.;Wang, R. L.;Huang, X. D.;Zhang, G. H.; Geng, L. A Flexible Artificial Spiking Photoreceptor Enabled by a Single VO2 Mott Memristor for the Spike-Based Electronic Retina. *ACS Applied Materials & Interfaces* **October 9, 2024**, *16*.

[171] Lee, H.;Cho, S. W.;Kim, S. J.;Lee, J.;Kim, K. S.;Kim, I.;Park, J.-K.;Kwak, J. Y.;Kim, J.;Park, J.;Jeong, Y.;Hwang, G. W.;Lee, K.-S.;Ielmini, D.; Lee, S. Three-Terminal Ovonic Threshold Switch (3T-OTS) with Tunable Threshold Voltage for Versatile Artificial Sensory Neurons. *Nano Letters* **2022**, *22*, 733-739.

[172] Han, J. K.;Kang, M.;Jeong, J.;Cho, I.;Yu, J. M.;Yoon, K. J.;Park, I.; Choi, Y. K. Artificial Olfactory Neuron for an In‐Sensor Neuromorphic Nose. *Advanced Science* **2022**, *9*, 2106017.

[173] Han, J.-K.;Park, S.-C.;Yu, J.-M.;Ahn, J.-H.; Choi, Y.-K. A Bioinspired Artificial Gustatory Neuron for a Neuromorphic Based Electronic Tongue. *Nano Letters* **2022**, *22*, 5244-5251.

[174] Zhu, J.;Zhang, X.;Wang, R.;Wang, M.;Chen, P.;Cheng, L.;Wu, Z.;Wang, Y.;Liu, Q.; Liu, M. A Heterogeneously Integrated Spiking Neuron Array for Multimode-Fused Perception and Object Classification. *Adv Mater* **2022**, *34*, e2200481.

[175] Boahen, K. A neuromorph's prospectus. *Computing in Science & Engineering* **2017**, *19*, 14-28.

[176] Han, C. Y.;Han, Z. R.;Fang, S. L.;Fan, S. Q.;Yin, J. Q.;Liu, W. H.;Li, X.;Yang, S. Q.;Zhang, G. H.;Wang, X. L.; Geng, L. Characterization and Modelling of Flexible VO2 Mott Memristor for the Artificial Spiking Warm Receptor. *Advanced Materials Interfaces* **2022/07/01**, *9*.

[177] Wu, Q.;Dang, B.;Lu, C.;Xu, G.;Yang, G.;Wang, J.;Chuai, X.;Lu, N.;Geng, D.;Wang, H.; Li, L. Spike Encoding with Optic Sensory Neurons Enable a Pulse Coupled Neural Network for Ultraviolet Image Segmentation. *Nano Letters* **2020**, *20*, 8015-8023.

[178] Pei, Y.;Li, Z.;Li, B.;Zhao, Y.;He, H.;Yan, L.;Li, X.;Wang, J.;Zhao, Z.;Sun, Y.;Zhou, Z.;Zhao, J.;Guo, R.;Chen, J.; Yan, X. A Multifunctional and Efficient Artificial Visual Perception Nervous System with Sb2Se3/CdS‐Core/Shell (SC) Nanorod Arrays Optoelectronic Memristor. *Advanced Functional Materials* **2022**, *32*, 2203454.

[179] Song, Z.;Tong, Y.;Zhao, X.;Ren, H.;Tang, Q.; Liu, Y. A flexible conformable artificial organ-damage memory system towards hazardous gas leakage based on a single organic transistor. *Materials Horizons* **2019**, *6*, 717-726.

[180] Trivedi, B. P. Gustatory system: The finer points of taste. *Nature* **2012**, *486*, S2-S3.

[181] Yuan, Y.;Gao, R.;Wu, Q.;Fang, S.;Bu, X.;Cui, Y.;Han, C.;Hu, L.;Li, X.;Wang, X.;Geng, L.; Liu, W. Artificial Leaky Integrate-and-Fire Sensory Neuron for In-Sensor Computing Neuromorphic Perception at the Edge. *ACS Sens* **2023**, *8*, 2646-2655.

[182] Peng, H.;Gan, L.; Guo, X. Memristor-based spiking neural networks: cooperative development of neural network architecture/algorithms and memristors. *Chip* **2024**, *3*.

[183] Zhang, X.;Yang, J. J.;Liu, Q.;Liu, M.;Wang, Z.;Song, W.;Midya, R.;Zhuo, Y.;Wang, R.;Rao, M.;Upadhyay, N. K.; Xia, Q. Experimental Demonstration of Conversion-Based SNNs with 1T1R Mott Neurons for Neuromorphic Inference. *2019 IEEE International Electron Devices Meeting (IEDM)* **2019**, 6.7.1-6.7.4.

[184] Guillaume Bellec, D. S., Anand Subramoney, Robert Legenstein, Wolfgang MaassAuthors Info & Claims Long short-term memory and learning-to-learn in networks of spiking neurons. *Advances in Neural Information Processing Systems 31* **2018**, 10.5555/3326943.3327017.

[185] Todri-Sanial, A.;Carapezzi, S.;Delacour, C.;Abernot, M.;Gil, T.;Corti, E.;Karg, S. F.;Nüñez, J.;Jiménèz, M.;Avedillo, M. J.; Linares-Barranco, B. How Frequency Injection Locking Can Train Oscillatory Neural Networks to Compute in Phase | IEEE Journals & Magazine | IEEE Xplore. *IEEE Transactions on Neural Networks and Learning Systems* **2022**, *33*.

[186] Johnson, J. L.; Johnson, J. L. Pulse-coupled neural nets: translation, rotation, scale, distortion, and intensity signal invariance for images. *Applied Optics, Vol. 33, Issue 26, pp. 6239-6253* **1994-09-10**, *33*.

[187] Zhang, W.;Mao, J.;Li, D.;Jing, X.;Zhang, S.;Wang, R.;Wang, S.;Zeng, T.;Ma, X.;Huang, Q.;Zhu, B.;Wang, H.; Hao, Y. Fusion of Near‐Infrared and UV Light Image via Artificial Visual Neurons Based on Mott Memristor. *Small* **2025/10/01**, *21*.

[188] Dang, B.;Zhang, T.;Wu, X.;Liu, K.;Huang, R.;Yang, Y.;Dang, B.;Zhang, T.;Wu, X.;Liu, K.;Huang, R.; Yang, Y. Reconfigurable in-sensor processing based on a multi-phototransistor–one-memristor array. *Nature Electronics 2024 7:11* **2024-11-12**, *7*.

[189] Li, Z.;Li, Z.;Tang, W.;Yao, J.;Dou, Z.;Gong, J.;Li, Y.;Zhang, B.;Dong, Y.;Xia, J.;Sun, L.;Jiang, P.;Cao, X.;Yang, R.;Miao, X.; Yang, R. Crossmodal sensory neurons based on high-performance flexible memristors for human-machine in-sensor computing system. *Nat Commun* **2024**, *15*, 7275.

[190] Zhang, G.;Luo, Q.;Yao, J.;Zhong, S.;Wang, H.;Xue, F.;Yu, B.;Loh, K. P.; Zhang, Y. All-in-one neuromorphic hardware with 2D material technology: current status and future perspective. *Chem Soc Rev* **2025**, *54*, 8196-8242.

[191] Baek, Y.;Bae, B.;Shin, H.;Sonnadara, C.;Cho, H.;Lin, C.-Y.;Mu, Y.;Shen, C.;Shah, S.;Wang, G.; Lee, K. Edge intelligence through in-sensor and near-sensor computing for the artificial intelligence of things. *npj Unconventional Computing* **2025**, *2*.

[192] Li, H.;Hu, J.;Zhang, Y.;Chen, A.;Zhou, J.;Zhao, Y.;Xu, Y.; Yu, B. Single‐Transistor Optoelectronic Spiking Neuron with Optogenetics‐Inspired Spatiotemporal Dynamics. *Advanced Functional Materials* **2024**, *34*.
[193] Hu, J.;Li, H.;Zhang, Y.;Zhou, J.;Zhao, Y.;Xu, Y.; Yu, B. Reconfigurable Neuromorphic Computing with 2D Material Heterostructures for Versatile Neural Information Processing. *Nano Lett* **2024**, *24*, 9391-9398.
[194] Lee, S.-W.;Kang, M.;Han, J.-K.;Yun, S.-Y.;Park, I.; Choi, Y.-K. An artificial olfactory sensory neuron for selective gas detection with in-sensor computing. *Device* **2023**, *1*.